This document has been superseded by a later version. For the latest version go to the web site: http://fire.nist.gov/fds

NIST Special Publication 1018

Fire Dynamics Simulator (Version 4) Technical Reference Guide

Kevin McGrattan, Editor

NIST National Institute of Standards and Technology • Technology Administration • U.S. Department of Commerce

NIST Special Publication 1018

Fire Dynamics Simulator (Version 4) Technical Reference Guide

Kevin McGrattan, Editor
Fire Research Division
Building and Fire Research Laboratory
in cooperation with
VTT Building and Transport, Finland

July 2004

U.S. Department of Commerce
Donald L. Evans, Secretary

Technology Administration
Phillip J. Bond, Under Secretary for Technology

National Institute of Standards and Technology
Arden L. Bement, Jr., Director

Certain commercial entities, equipment, or materials may be identified in this document in order to describe an experimental procedure or concept adequately. Such identification is not intended to imply recommendation or endorsement by the National Institute of Standards and Technology, nor is it intended to imply that the entities, materials, or equipment are necessarily the best available for the purpose.

National Institute of Standards and Technology Special Publication 1018
Natl. Inst. Stand. Technol. Spec. Publ. 1018, 85 pages (July 2004)
CODEN: NSPUE2

U.S. GOVERNMENT PRINTING OFFICE
WASHINGTON: 2004

For sale by the Superintendent of Documents, U.S. Government Printing Office
Internet: bookstore.gpo.gov – Phone: (202) 512-1800 – Fax: (202) 512-2250
Mail: Stop SSOP, Washington, DC 20402-0001

Preface

The use of fire models currently extends beyond the fire research laboratories and into the engineering, fire service and legal communities. Surveys [1] [2] of available fire models have been compiled and show a significant increase in the number of available models over the last decade. Sufficient evaluation of fire models is necessary to ensure that those using the models can judge the adequacy of their technical basis, appropriateness of their desired use, and confidence level of their predictions. This document provides the theoretical basis for the Fire Dynamics Simulator (FDS) and a summary of the work performed to verify and validate the model. Such evaluations of fire models prevent their unintentional misuse.

This guide is based in part on the "Standard Guide for Evaluating the Predictive Capability of Deterministic Fire Models," ASTM E 1355 [3]. ASTM E 1355 defines *model evaluation* as "the process of quantifying the accuracy of chosen results from a model when applied for a specific use." The model evaluation process consists of two main components: verification and validation. *Verification* is a process to check the correctness of the solution of the governing equations. Verification does not imply that the governing equations are appropriate; only that the equations are being solved correctly. *Validation* is a process to determine the appropriateness of the governing equations as a mathematical model of the physical phenomena of interest. Typically, validation involves comparing model results with experimental measurement. Differences that cannot be explained in terms of numerical errors in the model or uncertainty in the measurements are attributed to the assumptions and simplifications of the physical model.

Evaluation is critical to establishing both the acceptable uses and limitations of a model. Throughout its development, FDS has undergone various forms of evaluation, both at NIST and beyond. This guide provides a survey of work conducted to date to evaluate FDS. Roughly half of the referenced studies were aimed primarily at model evaluation, the other half describe limited work to validate FDS for a specific use. The latter group were performed mostly by practicing engineers who did not have the time or resources to comprehensively evaluate the model. Collectively, the body of work forms the basis of a model evaluation. As FDS development continues, the work performed to date will provide a framework for future research.

Disclaimer

The US Department of Commerce makes no warranty, expressed or implied, to users of the Fire Dynamics Simulator (FDS),and accepts no responsibility for its use. Users of FDS assume sole responsibility under Federal law for determining the appropriateness of its use in any particular application; for any conclusions drawn from the results of its use; and for any actions taken or not taken as a result of analysis performed using these tools.

Users are warned that FDS is intended for use only by those competent in the fields of fluid dynamics, thermodynamics, heat transfer, combustion, and fire science, and is intended only to supplement the informed judgment of the qualified user. The software package is a computer model that may or may not have predictive capability when applied to a specific set of factual circumstances. Lack of accurate predictions by the model could lead to erroneous conclusions with regard to fire safety. All results should be evaluated by an informed user.

Throughout this document, the mention of computer hardware or commercial software does not constitute endorsement by NIST, nor does it indicate that the products are necessarily those best suited for the intended purpose.

Acknowledgments

The Fire Dynamics Simulator has been under development for almost 25 years. Many people have contributed to this effort and should be acknowledged here.

At NIST, Howard Baum and Ronald Rehm laid the theoretical groundwork for the model and devised the basic numerical solvers that are still used in the code today. Kevin McGrattan added features needed to make the model accessible to practicing fire protection engineers, and he remains the custodian of the FDS source code. Glenn Forney developed the visualization tool Smokeview which not only made the public release possible, but it also serves as the principal diagnostic tool for the continuing development of FDS. Kuldeep Prasad added the multiple-block feature of the model, paving the way for parallel processing. William (Ruddy) Mell has developed unique applications of the model in areas of microgravity combustion and wildland fire spread. Charles Bouldin devised the basic framework of the parallel version of the code.

Several postdoctoral fellows at NIST have made significant contributions to the model development. Jason Floyd implemented the mixture fraction combustion model, Francine Battaglia studied the extension of the model to look at fire whirls, Javier Trelles extended the large eddy simulation technique to large, wind-blown fire plumes, Amy Musser considered indoor air quality applications along with her advisor Steve Emmerich of the Building Environment Division of BFRL, Dike Ezekoye worked on an early combustion model, Kevin Cassel used early versions of the model to study gravity currents/ceiling jets.

In the labs at NIST, Anthony Hamins has conducted a number of small and large scale experiments to validate FDS, including a substantial set of experiments in response to the World Trade Center fires and collapse. Alex Maranghides oversees the Large Fire Laboratory at NIST where these tests were conducted, and has helped to design the experiments. Dick Gann has overseen the fire part of the WTC effort. Other participants in the WTC effort are Rodney Bryant, Michelle Donnelly, Eric Johnsson, George Mulholland and Tom Ohlemiller. Technicians Laurean Delauter, Jay McElroy, Jack Lee, Mike Smith and Bill Twilley have conducted numerous validation experiments in both large and small test facilities at NIST.

Takashi Kashiwagi, Greg Linteris, and John Yang have worked on small-scale experiments that have been used to validate FDS. Tony Putorti, through graduate work with Prof. Arvind Atreya at the University of Michigan, has conducted experiments and analysis for sprinkler applications. William Grosshandler and Tom Cleary helped to develop the smoke detector activation algorithm that has been implemented in FDS. Grosshandler is also the developer of RadCal, a library of subroutines that have been incorporated in FDS to provide the radiative properties of gases and smoke.

Also at NIST, Dan Madrzykowski, Doug Walton, Bob Vettori, Dave Stroup, Steve Kerber, and Nelson Bryner have applied FDS to the reconstruction of several real fire incidents that led to the death of fire fighters. Dave Evans and Doug Walton oversaw the development of ALOFT, A Large Outdoor Fire plume Trajectory model, an early off-shoot of FDS.

At VTT Building and Transport, Finland, Simo Hostikka developed and implemented the radiation solver and the pyrolysis model for charring materials. Also at VTT, Jukka Hietaniemi, Jukka Vaari and Timo Korhonen have performed validation studies of various sub-models. The VTT Fire Research group continues to work on model development and validation of the model for various applications.

Within the fire protection engineering community, many individuals have made contributions to the

model, either through development of sub-models or through validation work. Wei Zhang, Vijay d'Souza, Jason Sutula, Steve Olenick, Doug Carpenter, and Richard Roby of Combustion Science and Engineering (CSE) implemented a smoke detector activation model within FDS and also validated various parts of the model. Doug Carpenter and Erin Mack Ashley of CSE conducted the literature review that is now part of the FDS Technical Reference Guide.

Jason Floyd and Javier Trelles, former NIST post-docs now working at Hughes Associates, continue to make vital contributions to the model because of their familiarity with the source code.

Chris Wood of ArupFire, Dave Sheppard of the US Bureau of Alcohol, Tobacco and Firearms (ATF), and Doug Carpenter of Combustion Science and Engineering developed a training course on the use of FDS and Smokeview on behalf of the Society of Fire Protection Engineers (SFPE). Morgan Hurley of the SFPE supported this effort. Prof. David McGill of Seneca College, Ontario, Canada has also conducted a remote-learning course on the use of FDS. Prof. Ian Thomas of Victoria University has presented short courses on the use of FDS in Australia. His students have also performed some validation work on compartment fires.

At the University of Maryland, Professors Fred Mowrer, Jim Quintiere, Jose Torero and Marino di Marzo have supervised students who have conducted validation work with FDS. In particular, Phil Friday and T. Ma have performed extensive validation work on the basic hydrodynamic solvers, and Paulo Ruffino has studied the activation of sprinklers that have been wetted by previously activated sprinklers. Profs. Arnaud Trouve and Andre Marshall are presently studying the application of FDS to under-ventilated fires.

At Worcester Polytechnic Institute (WPI), Prof. Johnathan Barnett has supervised several students, in particular Jay Ierardi and Chris Lautenberger, who have experimented with more detailed combustion models for small-scale applications.

At Northwestern University, Prof. Richard Lueptow has advised doctoral students Dave Sheppard and Jay Schwille whose research involved measurements of water sprays from sprinklers and mist nozzles.

At the University of Illinois, Chicago, Prof. Ishwar Puri along with students Anurag Jhalani and Achintya Mukhopadhyay validated the model against slot burner measurements. The purpose of their study was to quantify the effects of flame stretch.

At Virginia Tech, Prof. Uri Vandsburger hosted NIST Post-Doc Jason Floyd during his two-year tenure at NIST. Doctoral student Chris Wieczorek performed a series of compartment fire experiments used in part to validate FDS.

At Johns Hopkins University, Baltimore, Maryland, Jason Averill, a member of the NIST staff, has done graduate work with advisors Profs. Charles Meneveau and Omar Knio. The goal of the study was to evaluate the potential improvements to the large eddy simulation technique presently implemented in FDS.

At the University of Canterbury, Christchurch, New Zealand, Prof. Charles Fleischmann and his students have provided an extensive set of material properties of upholstered furnishings, plus performed validation studies. Doctoral student Jason Clement spent a semester at NIST validating the hydrodynamics of FDS against salt water data.

At Kingston University in Britain, Prof. Jennifer Wen and students have investigated the Smagorinsky model within FDS and experimented with various other approaches to model turbulence.

At Factory Mutual Research Corporation, John de Ris has contributed his expertise in developing an experimental soot growth model in FDS, along with Chris Lautenberger at WPI.

At Tyco Fire Products, Dave LeBlanc and James Golinveaux have contributed information and test data for various sprinkler designs.

At the US Nuclear Regulatory Commission, Monideep Dey has supported experiments to validate FDS as part of an international collaboration to study the application of fire models to nuclear power plants. NRC support also provided funding for the validation survey contained in this document. At another branch of the NRC, Chris Bajwa supported a modeling study of a recent tunnel fire in Baltimore, Maryland.

Grantees of the Building and Fire Research Laboratory at NIST who have contributed to FDS development include Prof. Pat Pagni of the University of California, Berkeley, Profs. G. Faeth and Arvind Atreya at

the University of Michigan, and Prof. Jay Gore at Purdue University.

Several guest researchers at NIST have made contributions in various areas, among them Prof. Yuji Nakamura, Nagoya University, Japan; Ales Jug, University of Iceland; Prof Bakhtier Farouk, Drexel University, Claudia Rexfort, Gerhard-Mercator-University Duisburg, Germany; Prof. Damian Rouson, City College, New York; Prof. Woe-Chul Park, Pukyong National University, Korea.

At National Fire Protection Association (NFPA), Rick Mulhaupt and Eric Peterson of the Research Foundation have extended invitations to various researchers to speak at a series of conferences about their efforts with FDS.

There have been many others who have contributed to the development of FDS, many of whom are listed in the References of this document.

Kevin McGrattan, July 2004

Contents

Chapter 1

Introduction

The idea that the dynamics of a fire might be studied numerically dates back to the beginning of the computer age. Indeed, the fundamental conservation equations governing fluid dynamics, heat transfer, and combustion were first written down over a century ago. Despite this, practical mathematical models of fire (as distinct from controlled combustion) are relatively recent due to the inherent complexity of the problem. Indeed, in his brief history of the early days of fire research, Hoyt Hottel noted "A case can be made for fire being, next to the life processes, the most complex of phenomena to understand" [4].

The difficulties revolve about three issues: First, there are an enormous number of possible fire scenarios to consider due to their accidental nature. Second, the physical insight and computing power required to perform all the necessary calculations for most fire scenarios are limited. Any fundamentally based study of fires must consider at least some aspects of bluff body aerodynamics, multi-phase flow, turbulent mixing and combustion, radiative transport, and conjugate heat transfer; all of which are active research areas in their own right. Finally, the "fuel" in most fires was never intended as such. Thus, the mathematical models and the data needed to characterize the degradation of the condensed phase materials that supply the fuel may not be available. Indeed, the mathematical modeling of the physical and chemical transformations of real materials as they burn is still in its infancy.

In order to make progress, the questions that are asked have to be greatly simplified. To begin with, instead of seeking a methodology that can be applied to all fire problems, we begin by looking at a few scenarios that seem to be most amenable to analysis. Hopefully, the methods developed to study these "simple" problems can be generalized over time so that more complex scenarios can be analyzed. Second, we must learn to live with idealized descriptions of fires and approximate solutions to our idealized equations. Finally, the methods should be capable of systematic improvement. As our physical insight and computing power grow more powerful, the methods of analysis can grow with them.

To date, three distinct approaches to the simulation of fires have emerged. Each of these treats the fire as an inherently three dimensional process evolving in time. The first to reach maturity, the "zone" models, describe compartment fires. Each compartment is divided into two spatially homogeneous volumes, a hot upper layer and a cooler lower layer. Mass and energy balances are enforced for each layer, with additional models describing other physical processes appended as differential or algebraic equations as appropriate. Examples of such phenomena include fire plumes, flows through doors, windows and other vents, radiative and convective heat transfer, and solid fuel pyrolysis. Descriptions of the physical and mathematical assumptions behind the zone modeling concept are given in separate papers by Jones [5] and Quintiere [6], who chronicle developments through 1983. Model development since then has progressed to the point where documented and supported software implementing these models are widely available [7].

The relative physical and computational simplicity of the zone models has led to their widespread use in the analysis of fire scenarios. So long as detailed spatial distributions of physical properties are not required,

and the two layer description reasonably approximates reality, these models are quite reliable. However, by their very nature, there is no way to systematically improve them. The rapid growth of computing power and the corresponding maturing of computational fluid dynamics (CFD), has led to the development of CFD based "field" models applied to fire research problems. Virtually all this work is based on the conceptual framework provided by the Reynolds-averaged form of the Navier-Stokes equations (RANS), in particular the $k-\varepsilon$ turbulence model pioneered by Patankar and Spalding [8]. The use of CFD models has allowed the description of fires in complex geometries, and the incorporation of a wide variety of physical phenomena. However, these models have a fundamental limitation for fire applications – the averaging procedure at the root of the model equations.

RANS models were developed as a time-averaged approximation to the conservation equations of fluid dynamics. While the precise nature of the averaging time is not specified, it is clearly long enough to require the introduction of large eddy transport coefficients to describe the unresolved fluxes of mass, momentum and energy. This is the root cause of the smoothed appearance of the results of even the most highly resolved fire simulations. The smallest resolvable length scales are determined by the product of the local velocity and the averaging time rather than the spatial resolution of the underlying computational grid. This property of RANS models is typically exploited in numerical computations by using implicit numerical techniques to take large time steps.

Unfortunately, the evolution of large eddy structures characteristic of most fire plumes is lost with such an approach, as is the prediction of local transient events. It is sometimes argued that the averaging process used to define the equations is an "ensemble average" over many replicates of the same experiment or postulated scenario. However, this is a moot point in fire research since neither experiments nor real scenarios are replicated in the sense required by that interpretation of the equations. The application of "Large Eddy Simulation" (LES) techniques to fire is aimed at extracting greater temporal and spatial fidelity from simulations of fire performed on the more finely meshed grids allowed by ever faster computers.

The phrase LES refers to the description of turbulent mixing of the gaseous fuel and combustion products with the local atmosphere surrounding the fire. This process, which determines the burning rate in most fires and controls the spread of smoke and hot gases, is extremely difficult to predict accurately. This is true not only in fire research but in almost all phenomena involving turbulent fluid motion. The basic idea behind the LES technique is that the eddies that account for most of the mixing are large enough to be calculated with reasonable accuracy from the equations of fluid dynamics. The hope (which must ultimately be justified by comparison to experiments) is that small-scale eddy motion can either be crudely accounted for or ignored.

The equations describing the transport of mass, momentum, and energy by the fire-induced flows must be simplified so that they can be efficiently solved for the fire scenarios of interest. The general equations of fluid dynamics describe a rich variety of physical processes, many of which have nothing to do with fires. Retaining this generality would lead to an enormously complex computational task that would shed very little additional insight on fire dynamics. The simplified equations, developed by Rehm and Baum [9], have been widely adopted by the larger combustion research community, where they are referred to as the "low Mach number" combustion equations. They describe the low speed motion of a gas driven by chemical heat release and buoyancy forces. Oran and Boris provide a useful discussion of the technique as applied to various reactive flow regimes in the chapter entitled "Coupled Continuity Equations for Fast and Slow Flows" in Ref. [10]. They comment that "There is generally a heavy price for being able to use a single algorithm for both fast and slow flows, a price which translates into many computer operations per timestep often spent in solving multiple and complicated matrix operations."

The low Mach number equations are solved numerically by dividing the physical space where the fire is to be simulated into a large number of rectangular cells. Within each cell the gas velocity, temperature, *etc.*, are assumed to be uniform; changing only with time. The accuracy with which the fire dynamics can be simulated depends on the number of cells that can be incorporated into the simulation. This number is

ultimately limited by the computing power available. Present day, single processor desktop computers limit the number of such cells to at most a few million. This means that the ratio of largest to smallest eddy length scales that can be resolved by the computation (the “dynamic range” of the simulation) is on the order of 100. Parallel processing can be used to extend this range to some extent, but the range of length scales that need to be accounted for if all relevant fire processes are to be simulated is roughly 10^4 to 10^5 because combustion processes take place at length scales of 1 mm or less, while the length scales associated with building fires are of the order of tens of meters. The form of the numerical equations discussed below depends on which end of the spectrum one wants to capture directly, and which end is to be ignored or approximated.

Chapter 2

Model and Scenario Definition

2.1 Model Documentation

This section provides a short description of the Fire Dynamics Simulator following the framework suggested by ASTM E 1355 [3]. It is intended to outline the major features of the model, its history, the underlying physical assumptions, and so on. More detailed information about the algorithm itself can be found in the next chapter.

2.1.1 Name and Version of the Model

The name of the program is the NIST Fire Dynamics Simulator or FDS. FDS is a Fortran 90 computer program that solves the governing equations of fluid dynamics, and Smokeview is a companion program written in C/OpenGL programming language that produces images and animations of the results. Version 1 of FDS was publicly released in February 2000, version 2 in December 2001, and version 3 in November 2002. The present version of FDS is 4, released in July 2004. Changes in the version number correspond to major changes in the physical model or input parameters. For minor changes and bug fixes, incremental versions are released, referenced according to fractions of the integer version number. For example, version 3.1 would be an updated release of version 3.0. In addition, day-to-day bug fixes made in response to user feedback are referenced by a compilation date that is printed at the top of the diagnostic output file.

2.1.2 Type of Model

FDS is a Computational Fluid Dynamics (CFD) model of fire-driven fluid flow. The model solves numerically a form of the Navier-Stokes equations appropriate for low-speed, thermally-driven flow with an emphasis on smoke and heat transport from fires. This type of model solves the fundamental equations of mass, momentum and energy. Since there is no analytical solution for the fully-turbulent Navier-Stokes equations, the solution requires the use of numerical methods where the compartment is divided into a three-dimensional grid of small cubes (grid cells). The model calculates the physical conditions in each cell as a function of time.

2.1.3 Model Developers

The Fire Dynamics Simulator (FDS) was developed and is currently maintained by the Fire Research Division in the Building and Fire Research Laboratory (BFRL) at the National Institute of Standards and Technology (NIST). A substantial contribution to the development of the model was made by VTT Building and Transport in Finland. Additional contributors are cited in the Acknowledgments .

2.1.4 Relevant Publications

Each version of FDS and Smokeview are documented by three separate publications – the FDS Technical Reference Guide, the FDS User's Guide [11], and the Smokeview User's Guide [12]. The User's Guides only describe the mechanics of using the computer programs. The Technical Reference Guide provides the theory and algorithm details, plus a description of the verification and validation studies.

There are numerous sources that describe various parts of the model. The basic set of equations solved in FDS were formulated by Rehm and Baum in the *Journal of Research of the National Bureau of Standards* [9]. The basic hydrodynamic algorithm evolved at NIST through the 1980s and 1990s, incorporating fairly well-known numerical schemes that are documented in books by Anderson, Tannehill and Pletcher [13], Peyret and Taylor [14], and Ferziger and Perić [15]. This last book provides a good description of the large eddy simulation technique and provides references to many current publications on the subject. Numerical techniques appropriate for combustion systems are described by Oran and Boris [10]. The mixture fraction combustion model is described by Bilger [16]. Basic heat transfer theory is provided by Holman [17] and Incropera [18]. Thermal radiation is described in Siegel and Howell [19]. Much of the current knowledge of fire is found in the *SFPE Handbook of Fire Protection Engineering* [20]. Textbooks in fire protection engineering include those by Drysdale [21] and Quintiere [22].

2.1.5 Governing Equations and Assumptions

Following is a brief description of the major components of FDS. Detailed information regarding the assumptions and governing equations associated with the model is provided in Section 3.2.

Hydrodynamic Model: FDS solves numerically a form of the Navier-Stokes equations appropriate for low-speed, thermally-driven flow with an emphasis on smoke and heat transport from fires. The core algorithm is an explicit predictor-corrector scheme, second order accurate in space and time. Turbulence is treated by means of the Smagorinsky form of Large Eddy Simulation (LES). It is possible to perform a Direct Numerical Simulation (DNS) if the underlying numerical grid is fine enough. LES is the default mode of operation.

Combustion Model: For most applications, FDS uses a mixture fraction combustion model. The mixture fraction is a conserved scalar quantity that is defined as the fraction of gas at a given point in the flow field that originated as fuel. The model assumes that combustion is mixing-controlled, and that the reaction of fuel and oxygen is infinitely fast. The mass fractions of all of the major reactants and products can be derived from the mixture fraction by means of "state relations," empirical expressions arrived at by a combination of simplified analysis and measurement.

Radiation Transport: Radiative heat transfer is included in the model via the solution of the radiation transport equation for a non-scattering gray gas, and in some limited cases using a wide band model. The equation is solved using a technique similar to finite volume methods for convective transport, thus the name given to it is the Finite Volume Method (FVM). Using approximately 100 discrete angles, the finite volume solver requires about 15 % of the total CPU time of a calculation, a modest cost given the complexity of radiation heat transfer. Water droplets can absorb thermal radiation. This is important in cases involving mist sprinklers, but also plays a role in all sprinkler cases. The absorption coefficients are based on Mie theory.

Geometry: FDS approximates the governing equations on one or more rectilinear grids. The user prescribes rectangular obstructions that are forced to conform with the underlying grid.

Boundary Conditions: All solid surfaces are assigned thermal boundary conditions, plus information about the burning behavior of the material. Usually, material properties are stored in a database and invoked by name. Heat and mass transfer to and from solid surfaces is usually handled with empirical correlations, although it is possible to compute directly the heat and mass transfer when performing a Direct Numerical

Simulation (DNS).

2.1.6 Input Data Required to Run the Model

All of the input parameters required by FDS to describe a particular scenario are conveyed via one or two text files created by the user. These files contain information about the numerical grid, ambient environment, building geometry, material properties, combustion kinetics, and desired output quantities. The numerical grid is one or more rectilinear meshes with (usually) uniform cells. All geometric features of the scenario have to conform to this numerical grid. Objects smaller than a single grid cell are either approximated as a single cell, or rejected. The building geometry is input as a series of rectangular blocks. Boundary conditions are applied to solid surfaces as rectangular patches. Materials are defined by their thermal conductivity, specific heat, density, thickness, and burning behavior. There are various ways that this information is conveyed, depending on the desired level of detail.

A significant part of the FDS input file directs the code to output various quantities in various ways. Much like in an actual experiment, the user must decide before the calculation begins what information to save. There is no way to recover information after the calculation is over if it was not requested at the start.

A complete description of the input parameters required by FDS can be found in the FDS User's Guide [11].

2.1.7 Property Data

Any simulation of a real fire scenario involves prescribing material properties for the walls, floor, ceiling, and furnishings. FDS treats all of these objects as homogenous solids, thus the physical parameters for many real objects can only be viewed as approximations to the actual properties. Describing these materials in the input file is the single most challenging task for the user. Thermal properties such as thermal conductivity, specific heat, density, and thickness can be found in various handbooks, or in manufacturers literature, or from bench-scale measurements. More difficult is the burning behavior at different heat fluxes. Even though entire books are devoted to the subject [23], it is still difficult to find information on a particular item.

There is a small file listing thermal properties of various common materials that is distributed with the FDS software. However, this data is meant to serve as examples. The data is not necessarily validated, and none of it is to be referenced as NIST data. The users of FDS are responsible for verifying the accuracy or appropriateness of each input parameter used. The FDS manuals describe the governing equations in which the material properties are used, but ultimately the user must decide if a given material conforms to the assumptions underlying the physical model.

2.1.8 Model Results

FDS computes the temperature, density, pressure, velocity and chemical composition within each numerical grid cell at each discrete time step. There are typically hundreds of thousands to several million grid cells and thousands to hundreds of thousands of time steps. In addition, FDS computes at solid surfaces the temperature, heat flux, mass loss rate, and various other quantities. The user must carefully select what data to save, much like one would do in designing an actual experiment. Even though only a small fraction of the computed information can be saved, the output typically consists of fairly large data files.

Time histories of various quantities at a single point in space or global quantities like the fire's heat release rate (HRR) are saved in simple, comma-delimited text files that can be plotted using a spreadsheet program. However, most field or surface data are visualized with a program called Smokeview, a tool specifically designed to analyze data generated by FDS. FDS and Smokeview are used in concert to model and visualize fire phenomena. Smokeview performs this visualization by presenting animated tracer particle

flow, animated contour slices of computed gas variables and animated surface data. Smokeview also presents contours and vector plots of static data anywhere within a scene at a fixed time.

A complete list of FDS output quantities and formats is given in Ref. [11]. Details on the use of Smokeview are found in Ref. [12].

2.1.9 Uses and Limitations

Throughout its development, FDS has been aimed at solving practical fire problems in fire protection engineering, while at the same time providing a tool to study fundamental fire dynamics and combustion. FDS can be used to model flame spread, smoke transport, heat transfer to surfaces (*e.g.* fuel surfaces or compartment walls), the activation of sprinklers, water droplet transport, and fire suppression by water droplets. Although FDS was designed specifically for fire simulations, it can be used for other low-speed fluid flow simulations that do not necessarily include fire or thermal effects. To date, about half of the applications of the model have been for design of smoke control systems and sprinkler/detector activation studies. The other half consist of residential and industrial fire reconstructions.

Although FDS can address most fire scenarios, there are limitations in all of its various algorithms. Some of the more prominent limitations of the model are listed here. More specific limitations are discussed as part of the description of the governing equations in Section 3.2.

Low Speed Flow: The use of FDS is limited to low-speed[1] flow with an emphasis on smoke and heat transport from fires. This assumption rules out using the model for any scenario involving flow speeds approaching the speed of sound, such as explosions, choke flow at nozzles, and detonations.

Geometry: The efficiency of FDS is due to the simplicity of its rectilinear numerical grid and the use of fast, direct solvers for the pressure field. This can be a limitation in some situations where certain geometric features do not conform to the rectangular grid, although most building components do. There are techniques in FDS to lessen the effect of "sawtooth" obstructions used to represent non-rectangular objects, but these cannot be expected to produce good results if, for example, the intent of the calculation is to study boundary layer effects. For most practical large-scale simulations, the increased grid resolution afforded by the fast pressure solver offsets the approximation of a curved boundary by small rectangular grid cells.

Fire Growth and Spread: Because the model was originally designed to analyze industrial-scale fires, it can be used reliably when the heat release rate (HRR) of the fire is specified and the transport of heat and exhaust products is the principal aim of the simulation. In these cases, the model predicts flow velocities and temperatures to an accuracy within 5 % to 20 % of experimental measurements, depending on the resolution of the numerical grid [2]. However, for fire scenarios where the heat release rate is *predicted* rather than *prescribed*, the uncertainty of the model is higher. There are several reasons for this: (1) properties of real materials and real fuels are often unknown or difficult to obtain, (2) the physical processes of combustion, radiation and solid phase heat transfer are more complicated than their mathematical representations in FDS, (3) the results of calculations are sensitive to both the numerical and physical parameters. Current research is aimed at improving this situation, but it is safe to say that modeling fire growth and spread will always require a higher level of user skill and judgment than that required for modeling the transport of smoke and heat from prescribed fires.

Combustion: For most applications, FDS uses a mixture fraction combustion model. The mixture fraction is a conserved scalar quantity that is defined as the fraction of gas at a given point in the flow field that originated as fuel. The model assumes that combustion is mixing-controlled, and that the reaction of fuel and oxygen is infinitely fast, regardless of the temperature. For large-scale, well-ventilated fires, this is a

[1] Mach numbers less than about 0.3

[2] It is extremely rare to find measurements of local velocities and/or temperatures from fire experiments that have reported error estimates that are less than 5 %. Thus, the most accurate calculations using FDS do not introduce significantly greater errors in these quantities than the vast majority of fire experiments.

good assumption. However, if a fire is in an under-ventilated compartment, or if a suppression agent like water mist or CO_2 is introduced, fuel and oxygen may mix but may not burn. Also, a shear layer with high strain rate separating the fuel stream from an oxygen supply can prevent combustion from taking place. The physical mechanisms underlying these phenomena are complex, and even simplified models still rely on an accurate prediction of the flame temperature and local strain rate. Sub-grid scale modeling of gas phase suppression and extinction is still an area of active research in the combustion community. Until reliable models can be developed for building-scale fire simulations, simple empirical rules can be used that prevent burning from taking place when the atmosphere immediately surrounding the fire cannot sustain the combustion. Details are found in Section 3.3.

Radiation: Radiative heat transfer is included in the model via the solution of the radiation transport equation for a non-scattering gray gas, and in some limited cases using a wide band model. The equation is solved using a technique similar to finite volume methods for convective transport, thus the name given to it is the Finite Volume Method (FVM). There are several limitations of the model. First, the absorption coefficient for the smoke-laden gas is a complex function of its composition and temperature. Because of the simplified combustion model, the chemical composition of the smokey gases, especially the soot content, can effect both the absorption and emission of thermal radiation. Second, the radiation transport is discretized via approximately 100 solid angles. For targets far away from a localized source of radiation, like a growing fire, the discretization can lead to a non-uniform distribution of the radiant energy. This can be seen in the visualization of surface temperatures, where "hot spots" show the effect of the finite number of solid angles. The problem can be lessened by the inclusion of more solid angles, but at a price of longer computing times. In most cases, the radiative flux to far-field targets is not as important as those in the near-field, where coverage by the default number of angles is much better.

2.2 Scenarios for Which Evaluation is Sought

Scenario documentation provides a description of the scenarios or phenomena of interest in the evaluation to facilitate appropriate application of the model, to aid in developing realistic inputs for the model, and criteria for judging the results of the evaluation. Such scenarios include the following information: a description of the scenarios or phenomenon of interest, a list of quantities predicted by the model for which evaluation is sought and the degree of accuracy required for each quantity.

2.2.1 Description of Scenarios or Phenomenon of Interest

FDS is suited for a wide range of problems associated with unwanted fires, both in the open (*e.g.* unconfined fire plumes) as well as within the built environment. Such phenomena include flame spread, smoke transport, heat transfer to surfaces, pyrolysis, sprinkler/detector activation, water droplet transport, and fire suppression. Although FDS was designed specifically for fire simulations, it can be used for other fluid flow simulations that do not necessarily involve fire or thermal processes.

2.2.2 List of Quantities Predicted by Model

For each gas phase grid cell, FDS predicts the gas temperature, density, major species concentrations, velocity, pressure, heat release rate per unit volume, soot volume fraction, visibility, plus other quantities related to the numerical scheme. On solid surfaces, FDS predicts the temperature, heat flux, burning rate, plus other quantities related to the overall energy balance at the surface. These various extra quantities are used by the developers for debugging purposes and not always listed in the manuals. For a complete list of user-accessible output quantities, consult the FDS User's Guide [11].

2.2.3 Degree of Accuracy Required for Each Output Quantity

The degree of accuracy for each output variable required by the user is highly dependent on the technical issues associated with the analysis. The user must ask: How accurate does the analysis have to be to answer the technical question posed? Thus, a generalized definition of the accuracy required with no regard as to the specifics of a particular analysis is not practical and would be limited in its usefulness.

Chapter 3

Theoretical Basis for the Model

3.1 Introduction

This chapter presents the theoretical basis for FDS, followed by a discussion of the model review process. The physical model is first presented as a set of partial differential equations, with appropriate simplifications and approximations noted. Then, the finite difference form of the equations are presented. This latter set constitutes the numerical algorithm.

3.2 Hydrodynamic Model

An approximate form of the Navier-Stokes equations appropriate for low Mach number applications is used in the model. The approximation involves the filtering out of acoustic waves while allowing for large variations in temperature and density [9]. This gives the equations an elliptic character, consistent with low speed, thermal convective processes. The computation can either be treated as a Direct Numerical Simulation (DNS), in which the dissipative terms are computed directly, or as a Large Eddy Simulation (LES), in which the large-scale eddies are computed directly and the sub-grid scale dissipative processes are modeled. The choice of DNS vs. LES depends on the objective of the calculation and the resolution of the computational grid. If, for example, the problem is to simulate the flow of smoke through a large, multi-room enclosure, it is not possible to resolve the combustion and transport processes directly. However, for small-scale combustion experiments, it is possible to compute the transport directly and the combustion processes to some extent.

3.2.1 Conservation Equations

FDS solves the basic conservation of mass, momentum and energy equations for a thermally-expandable, multi-component mixture of ideal gases [9]. The basic set of equations are presented here:
Conservation of Mass

$$\frac{\partial \rho}{\partial t} + \nabla \cdot \rho \mathbf{u} = 0 \tag{3.1}$$

Conservation of Species

$$\frac{\partial}{\partial t}(\rho Y_l) + \nabla \cdot \rho Y_l \mathbf{u} = \nabla \cdot \rho D_l \nabla Y_l + \dot{m}_l''' \tag{3.2}$$

Conservation of Momentum

$$\rho\left(\frac{\partial \mathbf{u}}{\partial t}+(\mathbf{u}\cdot\nabla)\mathbf{u}\right)+\nabla p=\rho\mathbf{g}+\mathbf{f}+\nabla\cdot\tau \tag{3.3}$$

Conservation of Energy

$$\frac{\partial}{\partial t}(\rho h)+\nabla\cdot\rho h\mathbf{u}=\frac{Dp}{Dt}-\nabla\cdot\mathbf{q}_r+\nabla\cdot k\nabla T+\sum_l \nabla\cdot h_l\rho D_l\nabla Y_l \tag{3.4}$$

Note that the external force on the fluid, represented by the term **f** in the above equations, consists of the drag exerted by water droplets emanating from sprinklers plus other external forces. The term $Dp/Dt = \partial p/\partial t + \mathbf{u}\cdot\nabla p$ is a material derivative.

3.2.2 State, Mass, and Energy Equations

The conservation equations are supplemented by an equation of state relating the thermodynamic quantities. An approximation to the ideal gas law is made by decomposing the pressure into a "background" component, a hydrostatic component, and a flow-induced perturbation

$$p = p_0 - \rho_\infty g z + \tilde{p} \tag{3.5}$$

For most applications, p_0 is constant and the other two components are relatively small. Adjustments to this assumption can be made in the case when the pressure rises due to a fire in a tightly sealed enclosure, or when the height of the domain is on the order of a kilometer and p_0 can no longer be assumed constant and must be considered a function of the altitude [24].

The purpose of decomposing the pressure is that for low-Mach number flows, it can be assumed that the temperature and density are inversely proportional, and thus the equation of state can be approximated [9]

$$p_0 = \rho T\mathcal{R}\sum(Y_i/M_i) = \rho T\mathcal{R}/M \tag{3.6}$$

The pressure p in the state and energy equations is replaced by the background pressure p_0 to filter out sound waves that travel at speeds that are much faster than typical flow speeds expected in fire applications. The low Mach number assumption serves two purposes. First, the filtering of acoustic waves means that the time step in the numerical algorithm is bound only by the flow speed as opposed to the speed of sound, and second, the modified state equation leads to a reduction in the number of dependent variables in the system of equations by one. The energy equation (3.4) is never explicitly solved, but its source terms are included in the expression for the flow divergence, an important quantity in the analysis to follow.

The divergence of the flow is obtained by taking the material derivative of the equation of state, and then substituting terms from the mass and energy conservation equations. First, define the constant-pressure specific heat of the mixture: $c_p = \sum_l c_{p,l} Y_l$ where $c_{p,l}$ is the temperature-dependent specific heat of species l. Next, define the enthalpy $h = \sum_l h_l Y_l$ where

$$h_l = h_l^0 + \int_{T^0}^{T} c_{p,l}(T')\,dT' \tag{3.7}$$

and h_l^0 is the heat of formation of species l. Now the divergence can be written

$$\begin{aligned}\nabla\cdot\mathbf{u} \;=\; & \frac{1}{\rho c_p T}\left(\nabla\cdot k\nabla T+\nabla\cdot\sum_l \int c_{p,l}dT\;\rho D_l\nabla Y_l-\nabla\cdot\mathbf{q}_r\right)+\\ & \frac{M}{\rho}\sum_l \nabla\cdot\rho D_l\nabla(Y_l/M_l)-\frac{1}{\rho c_p T}\sum_l \int c_{p,l}dT\;\nabla\cdot\rho D_l\nabla Y_l+\\ & \frac{1}{\rho}\sum_l\left(\frac{M}{M_l}-\frac{h_l}{c_p T}\right)\dot{m}_l'''+\left(\frac{1}{\rho c_p T}-\frac{1}{p_0}\right)\frac{dp_0}{dt}\end{aligned} \tag{3.8}$$

This expression can be simplified by making some approximations. Assume that $\int c_{p,l} dT \approx c_{p,l}\, T$. Further, assume the specific heat can be expressed in terms of the number of internal degrees of freedom ν_l active in the molecule.

$$c_{p,l} = \left(\frac{2+\nu_l}{2}\right)\frac{\mathcal{R}}{M_l} = \left(\frac{\gamma_l}{\gamma_l - 1}\right)\frac{\mathcal{R}}{M_l} \tag{3.9}$$

If the ratio of specific heats γ_l for each species is assumed to be constant, the second line of Eq. (3.8) disappears, and the only term left from the production term in line 3 is

$$\frac{1}{\rho}\sum_l \left(\frac{M}{M_l} - \frac{h_l}{c_p\, T}\right)\dot{m}_l''' = -\frac{1}{\rho\, c_p\, T}\sum_l h_l^0\, \dot{m}_l''' \tag{3.10}$$

which can be regarded as the energy due to the reaction. From here on, the reaction energy release rate per unit volume will be written $\dot{q}''' = -\sum_l h_l^0\, \dot{m}_l'''$.

The approximate form of the divergence used in the calculation is

$$\nabla\cdot\mathbf{u} = \frac{1}{\rho\, c_p\, T}\left(\nabla\cdot k\nabla T + \nabla\cdot\sum_l \int c_{p,l} dT\ \rho D_l \nabla Y_l - \nabla\cdot\mathbf{q}_r + \dot{q}'''\right) + \left(\frac{1}{\rho\, c_p\, T} - \frac{1}{p_0}\right)\frac{dp_0}{dt} \tag{3.11}$$

Notice that the assumption of a temperature-independent specific heat was made only to eliminate minor terms in the divergence expression, and thereby reduce the cost of the calculation. In general, it is not assumed that the specific heat is independent of temperature. The pressure rise term on the right hand side of the divergence expression is non-zero only if it assumed that the enclosure is tightly sealed, in which case the background pressure p_0 can no longer be assumed constant due to the increase (or decrease) in mass and thermal energy within the enclosure. The evolution equation for the pressure is found by integrating Eq. (3.11) over the entire domain Ω

$$\frac{dp_0}{dt} = \left[\int_\Omega \frac{1}{\rho\, c_p\, T}\left(\nabla\cdot k\nabla T + \ldots\right) dV - \int_{\partial\Omega}\mathbf{u}\cdot d\mathbf{S}\right] \Bigg/ \int_\Omega \left(\frac{1}{p_0} - \frac{1}{\rho\, c_p\, T}\right) dV \tag{3.12}$$

3.2.3 The Momentum Equation

The momentum equation is simplified to make it easier to solve numerically. First, start with the non-conservative form of the momentum equation introduced above

$$\rho\left(\frac{\partial\mathbf{u}}{\partial t} + (\mathbf{u}\cdot\nabla)\mathbf{u}\right) + \nabla p = \rho\mathbf{g} + \mathbf{f} + \nabla\cdot\tau \tag{3.13}$$

Next, make the following substitutions:

1. Subtract the hydrostatic pressure gradient, $\rho_\infty\mathbf{g}$, from both sides. Note that $\nabla p = \rho_\infty\mathbf{g} + \nabla\tilde{p}$.
2. Apply the vector identity: $(\mathbf{u}\cdot\nabla)\mathbf{u} = \nabla|\mathbf{u}|^2/2 - \mathbf{u}\times\omega$
3. Divide all terms by the density, ρ
4. Decompose the pressure term:
$$\frac{\nabla\tilde{p}}{\rho} = \frac{\nabla\tilde{p}}{\rho_\infty} + \left(\frac{1}{\rho} - \frac{1}{\rho_\infty}\right)\nabla\tilde{p}$$
5. Define $\mathcal{H} = |\mathbf{u}|^2/2 + \tilde{p}/\rho_\infty$

Now the momentum equation can be written

$$\frac{\partial \mathbf{u}}{\partial t} - \mathbf{u} \times \omega + \nabla \mathcal{H} + \left(\frac{1}{\rho} - \frac{1}{\rho_\infty} \right) \nabla \tilde{p} = \frac{1}{\rho} \left[(\rho - \rho_\infty)\mathbf{g} + \mathbf{f} + \nabla \cdot \tau \right] \tag{3.14}$$

The numerical solution of the pressure equation obtained by taking the divergence of Eq. (3.14) is greatly simplified by either neglecting the last term on the left hand side, or in cases where it cannot be neglected, treating it with some care. The decision to either neglect the extra pressure term or to approximate it depends on its relative contribution to the creation of vorticity. When the momentum equation is integrated around a closed loop that moves with the fluid, in the absence of any external forces, **f**, one can readily identify the sources of vorticity:

$$\frac{d\Gamma}{dt} = \oint \frac{1}{\rho_\infty} \left(1 - \frac{\rho_\infty}{\rho} \right) \nabla \tilde{p} \cdot d\mathbf{x} + \oint \frac{\rho - \rho_\infty}{\rho} \mathbf{g} \cdot d\mathbf{x} + \oint (\nabla \cdot \tau) \cdot d\mathbf{x} \tag{3.15}$$

The first term on the right hand side represents the baroclinic torque. The second term is buoyancy-induced vorticity. The third term represents the vorticity generated by viscosity or sub-grid scale mixing, as in boundary and shear layers. In most practical large scale fire simulations, the fire itself occupies a small part of the computational domain. Hence, the fire is often not well resolved by the numerical grid, in which case the vorticity generated in regions where there are large deviations in density is not captured directly. The mixing of air and combustion products occurs in the plume above the fire where buoyancy is the dominant source of vorticity. In these calculations, the baroclinic torque can be neglected to simplify the numerical solution. In simulations where detailed flame dynamics are resolvable, the pressure term responsible for the baroclinic torque cannot be neglected, but for reasons to be made clear below, must be treated differently than the other pressure term. In neither of these cases is the Boussinesq approximation invoked. The fluid is still considered thermally-expandable; the divergence is non-zero; the mass and energy equations are not modified.

The reason for either neglecting the baroclinic torque or decomposing the pressure term in the momentum equation is to simplify the elliptic partial differential equation obtained by taking the divergence of the momentum equation

$$\nabla^2 \mathcal{H} = -\frac{\partial (\nabla \cdot \mathbf{u})}{\partial t} - \nabla \cdot \mathbf{F} \quad ; \quad \mathbf{F} = -\mathbf{u} \times \omega + \left(\frac{1}{\rho} - \frac{1}{\rho_\infty} \right) \nabla \tilde{p} - \frac{1}{\rho} \left((\rho - \rho_\infty)\mathbf{g} + \mathbf{f} + \nabla \cdot \tau \right) \tag{3.16}$$

Note that the pressure $\tilde{p}$ appears on both sides of Eq. (3.16). The pressure on the right hand side is taken from the previous time step of the overall explicit time-marching scheme. It can be neglected if the baroclinic torque is not considered important in a given simulation. The pressure on the left hand side (incorporated in the variable $\mathcal{H}$) is (always) solved for directly. The reason for the decomposition of the pressure term is so that the linear algebraic system arising from the discretization of Eq. (3.16) has constant coefficients (*i.e.* it is *separable*) and can be solved to machine accuracy by a fast, direct (*i.e.* non-iterative) method that utilizes Fast Fourier Transforms (FFT). No-flux or forced-flow boundary conditions are specified by asserting that

$$\frac{\partial \mathcal{H}}{\partial n} = -F_n - \frac{\partial u_n}{\partial t} \tag{3.17}$$

where F_n is the normal component of **F** at the vent or solid wall, and $\partial u_n / \partial t$ is the prescribed rate of change in the normal component of velocity at a forced vent. Initially, the velocity is zero everywhere.

At open external boundaries the pressure-like term $\mathcal{H}$ is prescribed, depending on whether the flow is outgoing or incoming

$$\begin{array}{ll} \mathcal{H} = |\mathbf{u}|^2/2 & \text{outgoing} \\ \mathcal{H} = 0 & \text{incoming} \end{array} \tag{3.18}$$

The outgoing boundary condition assumes that the pressure perturbation $\tilde{p}$ is zero at an outgoing boundary and that $\mathcal{H}$ is constant along streamlines. The incoming boundary condition assumes that $\mathcal{H}$ is zero infinitely far away. At the boundary between two meshes, the pressure boundary condition is similar to that at an external open boundary, except that where the flow is incoming, $\mathcal{H}$ is taken from the adjacent mesh.

3.2.4 Diffusive Terms (LES)

The viscous stress tensor in the momentum equation is given by

$$\tau = \mu\left(2\,\mathrm{def}\,\mathbf{u} - \frac{2}{3}(\nabla\cdot\mathbf{u})\mathbf{I}\right) \tag{3.19}$$

where **I** is the identity matrix and the deformation tensor is defined

$$\mathrm{def}\,\mathbf{u} \equiv \frac{1}{2}\left[\nabla\mathbf{u} + (\nabla\mathbf{u})^t\right] = \begin{pmatrix} \frac{\partial u}{\partial x} & \frac{1}{2}\left(\frac{\partial u}{\partial y}+\frac{\partial v}{\partial x}\right) & \frac{1}{2}\left(\frac{\partial u}{\partial z}+\frac{\partial w}{\partial x}\right) \\ \frac{1}{2}\left(\frac{\partial v}{\partial x}+\frac{\partial u}{\partial y}\right) & \frac{\partial v}{\partial y} & \frac{1}{2}\left(\frac{\partial v}{\partial z}+\frac{\partial w}{\partial y}\right) \\ \frac{1}{2}\left(\frac{\partial w}{\partial x}+\frac{\partial u}{\partial z}\right) & \frac{1}{2}\left(\frac{\partial w}{\partial y}+\frac{\partial v}{\partial z}\right) & \frac{\partial w}{\partial z} \end{pmatrix} \tag{3.20}$$

In the numerical model, there are two options for treating the dynamic viscosity μ. For a Large Eddy Simulation (LES) where the grid resolution is not fine enough to capture the mixing processes at all relevant scales, a sub-grid scale model for

the viscosity is applied. Following the analysis of Smagorinsky [25], the viscosity can be modeled as

$$\mu_{\mathrm{LES}} = \rho\,(C_s\Delta)^2\left(2(\mathrm{def}\,\mathbf{u})\cdot(\mathrm{def}\,\mathbf{u}) - \frac{2}{3}(\nabla\cdot\mathbf{u})^2\right)^{\frac{1}{2}} \tag{3.21}$$

where C_s is an empirical constant, Δ is a length on the order of the size of a grid cell, and the deformation term is related to the Dissipation Function

$$\Phi \equiv \tau\cdot\nabla\mathbf{u} \equiv \mu\left(2(\mathrm{def}\,\mathbf{u})\cdot(\mathrm{def}\,\mathbf{u}) - \frac{2}{3}(\nabla\cdot\mathbf{u})^2\right) \tag{3.22}$$

$$= \mu\left[2\left(\frac{\partial u}{\partial x}\right)^2 + 2\left(\frac{\partial v}{\partial y}\right)^2 + 2\left(\frac{\partial w}{\partial z}\right)^2 + \right. \tag{3.23}$$

$$\left.\left(\frac{\partial v}{\partial x}+\frac{\partial u}{\partial y}\right)^2 + \left(\frac{\partial w}{\partial y}+\frac{\partial v}{\partial z}\right)^2 + \left(\frac{\partial u}{\partial z}+\frac{\partial w}{\partial x}\right)^2 - \frac{2}{3}\left(\frac{\partial u}{\partial x}+\frac{\partial v}{\partial y}+\frac{\partial w}{\partial z}\right)^2\right] \tag{3.24}$$

The dissipation function is the rate at which kinetic energy is transferred to thermal energy. It is a source term in the energy conservation equation that is usually neglected because it is small – an approximation consistent with the low Mach number equations.

In an LES calculation, the thermal conductivity and material diffusivity are related to the turbulent viscosity by

$$k_{\mathrm{LES}} = \frac{\mu_{\mathrm{LES}}\,c_p}{\mathrm{Pr}} \quad ; \quad (\rho D)_{l,\mathrm{LES}} = \frac{\mu_{\mathrm{LES}}}{\mathrm{Sc}} \tag{3.25}$$

The Prandtl number Pr and the Schmidt number Sc are assumed to be constant for a given scenario.

There have been numerous refinements of the original Smagorinsky model [26, 27, 28], but it is difficult to assess the improvements offered by these newer schemes. There are two reasons for this. First, the structure of the fire plume is so dominated by the large-scale resolvable eddies that even a constant eddy viscosity gives results almost identical to those obtained using the Smagorinsky model [29]. Second, the lack of precision in most large-scale fire test data makes it difficult to assess the relative accuracy of each model. The Smagorinsky model with constant C_s produces satisfactory results for most large-scale applications where boundary layers are not well resolved.

3.2.5 Diffusive Terms (DNS)

For a Direct Numerical Simulation (DNS), the viscosity, thermal conductivity and material diffusivity are approximated from kinetic theory. The viscosity of the lth species is given by

$$\mu_l = \frac{26.69 \times 10^{-7} (M_l\, T)^{\frac{1}{2}}}{\sigma_l^2\, \Omega_v} \qquad \frac{\text{kg}}{\text{m s}} \tag{3.26}$$

where σ_l is the Lennard-Jones hard-sphere diameter (Å) and Ω_v is the collision integral, an empirical function of the temperature T. The thermal conductivity of the lth species is given by

$$k_l = \frac{\mu_l\, c_{p,l}}{\text{Pr}} \qquad \frac{\text{W}}{\text{m K}} \tag{3.27}$$

where the Prandtl number Pr is 0.7. The viscosity and thermal conductivity of a gas mixture are given by

$$\mu_{\text{DNS}} = \sum_l Y_l\, \mu_l \quad ; \quad k_{\text{DNS}} = \sum_l Y_l\, k_l \tag{3.28}$$

The binary diffusion coefficient of the lth species diffusing into the mth species is given by

$$D_{lm} = \frac{2.66 \times 10^{-7}\, T^{3/2}}{M_{lm}^{\frac{1}{2}}\, \sigma_{lm}^2\, \Omega_D} \qquad \frac{\text{m}^2}{s} \tag{3.29}$$

where $M_{lm} = 2(1/M_l + 1/M_m)^{-1}$, $\sigma_{lm} = (\sigma_l + \sigma_m)/2$, and Ω_D is the diffusion collision integral, an empirical function of the temperature T [30]. It is assumed that nitrogen is the dominant species in any combustion scenario considered here, thus the diffusion coefficient in the species mass conservation equations is that of the given species diffusing into nitrogen

$$(\rho D)_{l,\text{DNS}} = \rho\, D_{l0} \tag{3.30}$$

where species 0 is nitrogen.

3.3 Combustion

There are two types of combustion models used in FDS. The choice depends on the resolution of the underlying grid. For a DNS calculation where the diffusion of fuel and oxygen can be modeled directly, a global one-step, finite-rate chemical reaction is most appropriate. However, in an LES calculation where the grid is not fine enough to resolve the diffusion of fuel and oxygen, a mixture fraction-based combustion model is used.

3.3.1 Mixture Fraction Combustion Model

The mixture fraction combustion model is based on the assumption that large-scale convective and radiative transport phenomena can be simulated directly, but physical processes occurring at small length and time scales must be represented in an approximate manner. The nature of the approximations employed are necessarily a function of the spatial and temporal resolution limits of the computation, as well as our current (often limited) understanding of the phenomena involved.

The actual chemical rate processes that control the combustion energy release are often unknown in fire scenarios. Even if they were known, the spatial and temporal resolution limits imposed by both present and foreseeable computer resources places a detailed description of combustion processes beyond reach. Thus, the model adopted here is based on the assumption that the combustion is mixing-controlled. This implies that all species of interest can be described in terms of a mixture fraction $Z(\mathbf{x},t)$. The mixture fraction is a conserved quantity representing the fraction of material at a given point that originated in the fuel stream. The relations between the mass fraction of each species and the mixture fraction are known as "state relations". The state relation for the oxygen mass fraction provides the information needed to calculate the local oxygen mass consumption rate. The form of the state relation that emerges from classical laminar diffusion flame theory is a piecewise linear function. This leads to a "flame sheet" model, where the flame is a two dimensional surface embedded in a three dimensional space. The local heat release rate is computed from the local oxygen consumption rate at the flame surface, assuming that the heat release rate is directly proportional to the oxygen consumption rate, independent of the fuel involved. This relation, originally proposed by Huggett [31], is the basis of oxygen calorimetry.

Start with the most general form of the combustion reaction

$$\nu_F \text{ Fuel} + \nu_O \text{ O}_2 \rightarrow \sum_i \nu_{P,i} \text{ Products} \tag{3.31}$$

The numbers ν_i are the stoichiometric coefficients for the overall combustion process that reacts fuel "F" with oxygen "O" to produce a number of products "P". The stoichiometric equation (3.31) implies that the mass consumption rates for fuel and oxidizer are related as follows:

$$\frac{\dot{m}_F'''}{\nu_F M_F} = \frac{\dot{m}_O'''}{\nu_O M_O} \tag{3.32}$$

The mixture fraction Z is defined as:

$$Z = \frac{sY_F - (Y_O - Y_O^\infty)}{sY_F^I + Y_O^\infty} \quad ; \quad s = \frac{\nu_O M_O}{\nu_F M_F} \tag{3.33}$$

By design, it varies from $Z = 1$ in a region containing only fuel to $Z = 0$ where the oxygen mass fraction takes on its un depleted ambient value, Y_O^∞. Note that Y_F^I is the fraction of fuel in the fuel stream. The quantities M_F and M_O are the fuel and oxygen molecular weights, respectively. The mixture fraction satisfies the conservation law

$$\rho \frac{DZ}{Dt} = \nabla \cdot \rho D \nabla Z \tag{3.34}$$

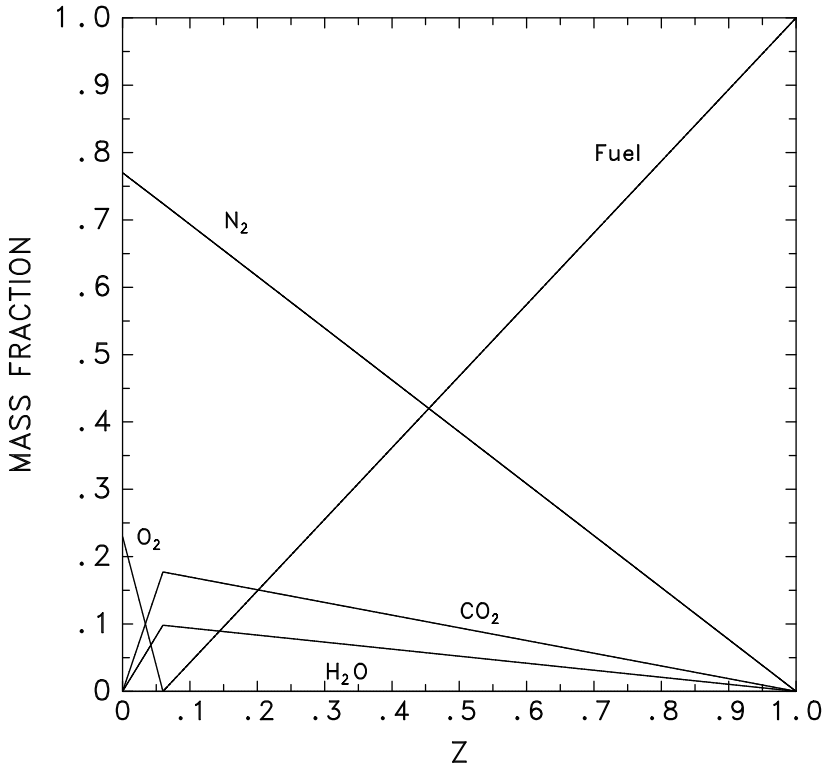

Figure 3.1: State relations for propane.

obtained from a linear combination of the fuel and oxygen conservation equations. The assumption that the chemistry is "fast" means that the reactions that consume fuel and oxidizer occur so rapidly that the fuel and oxidizer cannot co-exist. The requirement that fuel and oxidizer simultaneously vanish defines a flame surface as:

$$Z(\mathbf{x},t) = Z_f \quad ; \quad Z_f = \frac{Y_O^\infty}{sY_F^I + Y_O^\infty} \tag{3.35}$$

The assumption that fuel and oxidizer cannot co-exist leads to the "state relation" between the oxygen mass fraction Y_O and Z

$$Y_O(Z) = \begin{cases} Y_O^\infty(1 - Z/Z_f) & Z < Z_f \\ 0 & Z > Z_f \end{cases} \tag{3.36}$$

State relations for both reactants and products can be derived by considering the following ideal reaction of a hydrocarbon fuel:

$$\begin{aligned} \mathrm{C_xH_y} + \eta(\mathrm{x}+\mathrm{y}/4)\ (\mathrm{O_2} + 3.76\,\mathrm{N_2}) \quad &\rightarrow \quad \max(0, 1-\eta)\ \mathrm{C_xH_y} + \min(1,\eta)\ \mathrm{x\ CO_2} + \\ \min(1,\eta)\ (\mathrm{y}/2)\ \mathrm{H_2O} \quad &+ \quad \max(0,\eta-1)\ (\mathrm{x}+\mathrm{y}/4)\ \mathrm{O_2} + \eta(\mathrm{x}+\mathrm{y}/4)3.76\,\mathrm{N_2} \end{aligned} \tag{3.37}$$

Here η is a parameter ranging from 0 (all fuel with no oxygen) to infinity (all oxygen with no fuel). A correspondence between η and Z is obtained by applying the definition of Z (Eq. 3.33) to the left hand side of Eq. (3.37). Mass fractions of the products of the infinitely fast reaction (including excess fuel or oxygen) can be obtained from the right hand side of Eq. (3.37).

An expression for the local heat release rate can be derived from the conservation equations and the state relation for oxygen. The starting point is Huggett's [31] relationship for the heat release rate as a function of the oxygen consumption

$$\dot{q}''' = \Delta H_O\, \dot{m}_O''' \tag{3.38}$$

Here, ΔH_O is the heat release rate per unit mass of oxygen consumed (about 13,100 kJ/kg for most fuels). The oxygen mass conservation equation

$$\rho \frac{DY_O}{Dt} = \nabla \cdot \rho D \nabla Y_O + \dot{m}_O''' \tag{3.39}$$

can be transformed into an expression for the local heat release rate using the conservation equation for the mixture fraction (3.34) and the state relation for oxygen $Y_O(Z)$.

$$-\dot{m}_O''' = \nabla \cdot \left(\rho D \frac{dY_O}{dZ} \nabla Z \right) - \frac{dY_O}{dZ} \nabla \cdot \rho D \nabla Z = \rho D \, \frac{d^2 Y_O}{dZ^2} |\nabla Z|^2 \tag{3.40}$$

Neither of these expressions for the local oxygen consumption rate is particularly convenient to apply numerically because of the discontinuity of the derivative of $Y_O(Z)$ at $Z = Z_f$. However, an expression for the oxygen consumption rate per unit area of flame sheet can be derived from Eq. (3.40) by integrating $\dot{m}_O'''$ over a small volume through which the flame sheet cuts. Working with the middle terms of Eq. (3.40) and noting that dY_O/dZ is constant on one side of the flame sheet and zero on the other, the volume integral can be rewritten as a surface integral over the flame sheet by applying the divergence theorem and seeing that the two terms cancel at the exterior boundary of the control volume. At this point, it is more convenient to express the oxygen consumption rate in units of mass per unit time per unit area of flame sheet:

$$-\dot{m}_O'' = \left. \frac{dY_O}{dZ} \right|_{Z<Z_f} \rho D \, \nabla Z \cdot \mathbf{n} \tag{3.41}$$

In the numerical algorithm, the local heat release rate is computed by first locating the flame sheet, then computing the local heat release rate per unit area, and finally distributing this energy to the grid cells cut by the flame sheet. In this way, the ideal, infinitely thin flame sheet is smeared out over the width of a grid cell, consistent with all other gas phase quantities.

3.3.2 Enhancements to the Mixture Fraction Model

The mixture fraction model described in the previous section has several limitations, both numerical and physical. Its numerical limitations are related to the resolution of the underlying numerical grid. On coarse grids, the accuracy of the fuel transport and combustion processes is diminished by the high levels of numerical diffusion. The above procedure for determining the local heat release rate works well for calculations in which the fire is adequately resolved. A measure of how well the fire is resolved is given by the nondimensional expression $D^*/\delta x$, where D^* is a characteristic fire diameter

$$D^* = \left(\frac{\dot{Q}}{\rho_\infty c_p T_\infty \sqrt{g}} \right)^{\frac{2}{5}} \tag{3.42}$$

and δx is the nominal size of a grid cell[1]. The quantity $D^*/\delta x$ can be thought of as the number of computational cells spanning the characteristic (not necessarily the physical) diameter of the fire. The more cells spanning the fire, the better the resolution of the calculation. For fire scenarios where D^* is small relative to the physical diameter of the fire, and/or the numerical grid is relatively coarse, the stoichiometric surface $Z = Z_f$ will underestimate the observed flame height [32, 33, 34]. It has been found empirically that a good

[1]The characteristic fire diameter is related to the characteristic fire size via the relation $Q^* = (D^*/D)^{5/2}$, where D is the physical diameter of the fire.

estimate of flame height can be found for crude grids if a different value of Z is used to define the combustion region

$$\frac{Z_{f,\mathrm{eff}}}{Z_f} = \min\left(1\ ,\ C\,\frac{D^*}{\delta x}\right) \tag{3.43}$$

Here C is an empirical constant equal to 0.6 to be used for all fire scenarios. As the resolution of the calculation increases, the $Z_{f,\mathrm{eff}}$ approaches the ideal value, Z_f, at which point the approximation is no longer required. The benefit of the expression is that it provides a quantifiable measure of the grid resolution that takes into account not only the size of the grid cells, but also the size of the fire.

Another consequence of a coarse numerical grid is that a disproportionate amount of the combustion energy is released near the edges of the burner. From Eq. 3.41, it can be seen that the heat release rate per unit area of the flame sheet is proportional to the local gradient of the mixture fraction and the local value of the material diffusivity. The gradient of the mixture fraction is large at the base of the fire because there a stream of pure fuel meets surrounding air. The diffusivity is large on a coarse grid because it is related to the Smagorinsky viscosity. To prevent too much of the energy from being released too close to the burner when a coarse grid is used, there is a maximum bound imposed on the local heat release rate per unit area of flame sheet. This upper bound is based on a simple analysis in which the fire is assumed to be conical in shape with surface area, A, and a flame height, H, given by Heskestad's correlation [35]

$$H/D = 3.7\,Q^{*2/5} - 1.02 \quad ; \quad A = \pi r\sqrt{r^2+h^2} \tag{3.44}$$

The surface area of a real flame is larger than that of a cone, so the upper bound estimate will prevent too much energy from being released too close to the fire when a coarse grid is used, but will be high enough not to interfere with the calculation when the grid is well-resolved. Any energy that is "clipped" off due to the upper bound is redistributed over the entire flame volume.

The physical limitation of the mixture fraction approach is that it is assumed that fuel and oxygen burn instantaneously when mixed. For large-scale, well-ventilated fires, this is a good assumption. However, if a fire is in an under-ventilated compartment, or if a suppression agent like water mist or CO_2 is introduced, fuel and oxygen may mix but may not burn. Also, a shear layer with high strain rate separating the fuel stream from an oxygen supply can prevent combustion from taking place. The physical mechanisms underlying these phenomena are complex, and even simplified models still rely on an accurate prediction of the flame temperature and local strain rate. Sub-grid scale modeling of gas phase suppression and extinction is still an area of active research in the combustion community. Until reliable models can be developed for building-scale fire simulations, simple empirical rules can be used that prevent burning from taking place when the atmosphere immediately surrounding the fire cannot sustain the combustion. Based on the work of Quintiere [6], Beyler [36] and others, a simple model for flame extinction has been implemented in FDS. The mixture fraction continues to be used to track the progress of the fuel mixing with the surrounding air, but now the surrounding volume is assessed to determine if it is more or less likely to support combustion. Figure 3.2 shows values of temperature and oxygen concentration for which burning can and cannot take place.

Note that once the gas environment falls in the "No Burn" zone, the state relations (Fig. 3.1) are no longer valid for values of Z below stoichiometric, since now some fuel may be mixed with the other combustion products. To account for the deviation from the ideal state relations, at least one other scalar quantity in addition to the mixture fraction would have to be tracked in the calculation. Research is ongoing to add this second scalar to the model.

3.3.3 Finite-Rate Reaction (DNS)

In a DNS calculation, the diffusion of fuel and oxygen can be modeled directly, thus it is possible to implement a relatively simple one-step chemical reaction. Consider the reaction of oxygen and a hydrocarbon

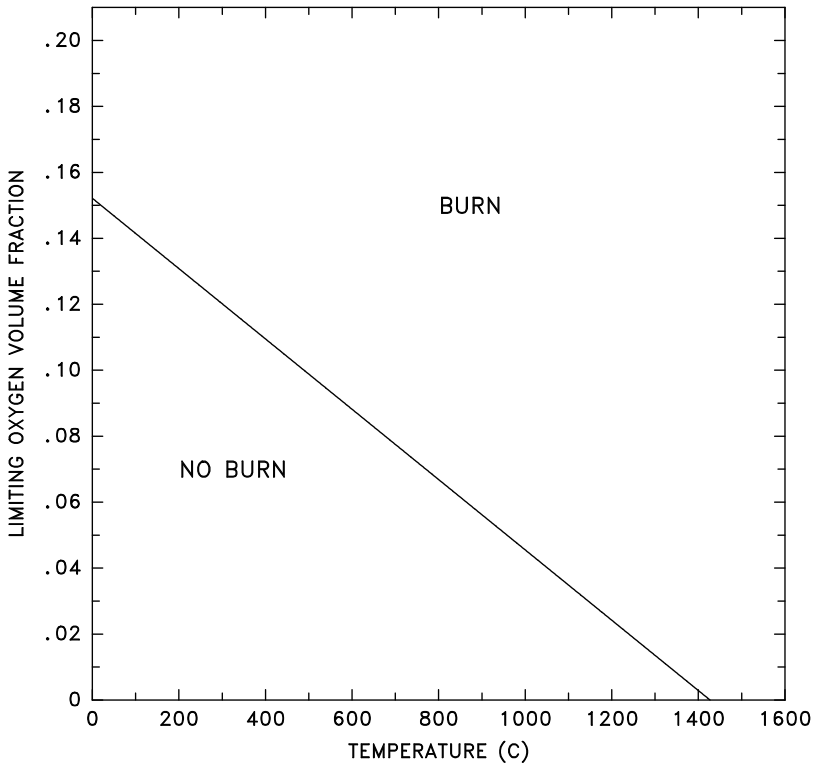

Figure 3.2: Oxygen-temperature phase space showing where combustion is allowed and not allowed to take place.

fuel

$$\nu_{C_xH_y} C_xH_y + \nu_{O_2} O_2 \longrightarrow \nu_{CO_2} CO_2 + \nu_{H_2O} H_2O \tag{3.45}$$

The reaction rate is given by the expression

$$\frac{d[C_xH_y]}{dt} = -B\,[C_xH_y]^a\,[O_2]^b\,e^{-E/RT} \tag{3.46}$$

Suggested values of B, E, a and b for various hydrocarbon fuels are given in Refs. [37, 38]. It should be understood that the implementation of any of these one-step reaction schemes is still very much a research exercise because it is not universally accepted that combustion phenomena can be represented by such a simple mechanism. Efforts are currently underway to determine in what cases a one-step reaction mechanism provides a valid description of the combustion process.

3.4 Thermal Radiation Model

The Radiative Transport Equation (RTE) for an absorbing/emitting and scattering medium is

$$\mathbf{s}\cdot\nabla I_\lambda(\mathbf{x},\mathbf{s}) = -\left[\kappa(\mathbf{x},\lambda)+\sigma_s(\mathbf{x},\lambda)\right] I(\mathbf{x},\mathbf{s}) + B(\mathbf{x},\lambda) + \frac{\sigma_s(\mathbf{x},\lambda)}{4\pi}\int_{4\pi}\Phi(\mathbf{s},\mathbf{s}')\, I_\lambda(\mathbf{x},\mathbf{s}')\, d\Omega' \tag{3.47}$$

where $I_\lambda(\mathbf{x},\mathbf{s})$ is the radiation intensity at wavelength λ, $\mathbf{s}$ is the direction vector of the intensity, $\kappa(\mathbf{x},\lambda)$ and $\sigma_s(\mathbf{x},\lambda)$ are the local absorption and scattering coefficients, respectively, and $B(\mathbf{x},\lambda)$ is the emission source term. The integral on the right hand side describes the in-scattering from other directions. In the case of a non-scattering gas the RTE becomes

$$\mathbf{s}\cdot\nabla I_\lambda(\mathbf{x},\mathbf{s}) = \kappa(\mathbf{x},\lambda)\ \left[I_b(\mathbf{x}) - I(\mathbf{x},\mathbf{s})\right] \tag{3.48}$$

where $I_b(\mathbf{x})$ is the source term given by the Planck function. This section describes the radiation transport in the gas phase.

In practical simulations the spectral dependence can not be solved accurately. Instead, the radiation spectrum is divided into a relatively small number of bands, and a separate RTE is derived for each band. The limits of the bands are selected to give an accurate representation of the most important radiation bands of CO_2 and water. The band specific RTE's are now

$$\mathbf{s}\cdot\nabla I_n(\mathbf{x},\mathbf{s}) = \kappa_n(\mathbf{x})\ \left[I_{b,n}(\mathbf{x}) - I(\mathbf{x},\mathbf{s})\right],\ \ n = 1...N \tag{3.49}$$

where I_n is the intensity integrated over the band n, and κ_n is the appropriate mean absorption coefficient inside the band. The source term can be written as a fraction of the blackbody radiation

$$I_{b,n} = F_n(\lambda_{\min},\lambda_{\max})\ \sigma\, T^4/\pi \tag{3.50}$$

where σ is the Stefan-Boltzmann constant. The calculation of factors F_n is explained in Ref. [19]. When the intensities corresponding to the bands are known, the total intensity is calculated by summing over all the bands

$$I(\mathbf{x},\mathbf{s}) = \sum_{n=1}^{N} I_n(\mathbf{x},\mathbf{s}) \tag{3.51}$$

From a series of numerical experiments it has been found that six bands are usually enough ($N = 6$). If the absorption of the fuel is known to be important, separate bands can be reserved for fuel, and the total number of bands is increased to ten ($N = 10$). For simplicity, the fuel is assumed to be CH_4. The limits of the bands are shown in Table 3.1.

Table 3.1: Limits of the spectral bands.

9 Band Model	1	2	3	4	5	6	7	8	9
Major Species	Soot	CO_2 H_2O, Soot	CH_4 Soot	Soot	CO_2 Soot	H_2O Soot	H_2O CH_4, Soot	Soot	Soot
ν (1/cm)	10000	3800	3400	2800	2400	2174	1429	1160	1000 50
λ (μm)	1.00	2.63	2.94	3.57	4.17	4.70	7.00	8.62	10.0 200

6 Band Model	1	2	3	4	5	6
Major Species	Soot	CO_2 H_2O, Soot	CH_4 Soot	CO_2 Soot	H_2O, CH_4, Soot	Soot

Even with a reasonably small number of bands, the solution of N RTE's is very time consuming. Fortunately, in most large-scale fire scenarios soot is the most important combustion product controlling the

thermal radiation from the fire and hot smoke. As the radiation spectrum of soot is continuous, it is possible to assume that the gas behaves as a gray medium. The spectral dependence is lumped into one absorption coefficient ($N = 1$) and the source term is given by the blackbody radiation intensity

$$I_b(\mathbf{x}) = \sigma T(\mathbf{x})^4/\pi \tag{3.52}$$

In optically thin flames, where the amount of soot is small compared to the amount of CO_2 and water, the gray gas assumption may produce significant overpredictions of the emitted radiation.

For the calculation of the gray or band-mean absorption coefficients, κ_n, a narrow-band model, RadCal [39], has been implemented in FDS. At the start of a simulation the absorption coefficient(s) are tabulated as a function of mixture fraction and temperature. During the simulation the local absorption coefficient is found by table-lookup.

In calculations of limited spatial resolution, the source term, I_b, in the RTE requires special treatment in the neighborhood of the flame sheet because the temperatures are smeared out over a grid cell and are thus considerably lower than one would expect in a diffusion flame. Because of its dependence on the temperature raised to the fourth power, the source term must be modeled in those grid cells cut by the flame sheet. Elsewhere, there is greater confidence in the computed temperature, and the source term can assume its ideal value there

$$\kappa I_b = \begin{cases} \kappa\sigma T^4/\pi & \text{Outside flame zone} \\ \chi_r \dot{q}'''/4\pi & \text{Inside flame zone} \end{cases} \tag{3.53}$$

Here, $\dot{q}'''$ is the chemical heat release rate per unit volume and χ_r is the *local* fraction of that energy emitted as thermal radiation. Note the difference between the prescription of a local χ_r and the resulting global equivalent. For a small fire ($D < 1$ m), the local χ_r is approximately equal to its global counterpart. However, as the fire increases in size, the global value will typically decrease due to a net re-absorption of the thermal radiation by the increasing smoke mantle.

The boundary condition for the radiation intensity leaving a gray diffuse wall is given as

$$I_w(\mathbf{s}) = \varepsilon I_{bw} + \frac{1-\varepsilon}{\pi} \int_{\mathbf{s}'\cdot\mathbf{n}_w<0} I_w(\mathbf{s}')\ |\mathbf{s}'\cdot\mathbf{n}_w|\ d\Omega \tag{3.54}$$

where $I_w(\mathbf{s})$ is the intensity at the wall, ε is the emissivity, and I_{bw} is the black body intensity at the wall.

The radiative transport equation (3.49) is solved using techniques similar to those for convective transport in finite volume methods for fluid flow [40], thus the name given to it is the Finite Volume Method (FVM).

To obtain the discretized form of the RTE, the unit sphere is divided into a finite number of solid angles. In each grid cell a discretized equation is derived by integrating equation (3.48) over the cell ijk and the control angle $\delta\Omega^l$, to obtain

$$\int_{\Omega^l}\int_{V_{ijk}} \mathbf{s}\cdot\nabla I_n(\mathbf{x},\mathbf{s}) dV d\Omega = \int_{\Omega^l}\int_{V_{ijk}} \kappa_n(\mathbf{x})\ [I_{b,n}(\mathbf{x}) - I_n(\mathbf{x},\mathbf{s})]\, dV d\Omega \tag{3.55}$$

The volume integral on the left hand side is replaced by a surface integral over the cell faces using the divergence theorem. Assuming that the radiation intensity $I(\mathbf{x},\mathbf{s})$ is constant on each of the cell faces, the surface integral can be approximated by a sum over the cell faces. More detail on the discretization and solution of the RTE can be found in Section 3.7.7.

The radiant heat flux vector $\mathbf{q}_r$ is defined

$$\mathbf{q}_r(\mathbf{x}) = \int \mathbf{s} I(\mathbf{x},\mathbf{s})\ d\Omega \tag{3.56}$$

The radiative loss term in the energy equation is

$$-\nabla\cdot\mathbf{q}_r(\mathbf{x}) = \kappa(\mathbf{x})\,[U(\mathbf{x}) - 4\pi I_b(\mathbf{x})] \quad ; \quad U(\mathbf{x}) = \int_{4\pi} I(\mathbf{x},\mathbf{s})\,d\Omega \tag{3.57}$$

In words, the net radiant energy gained by a grid cell is the difference between that which is absorbed and that which is emitted.

3.5 Thermal Boundary Conditions

The type of thermal boundary condition applied at any given surface depends on whether that surface is to heat up and burn, whether the burning rate will simply be prescribed, or whether there is to be any burning at all.

3.5.1 Convective Heat Transfer to Walls

The heat fluxes to a solid surface consist of gains and losses from convection and radiation. The radiative flux at the surface is obtained from the boundary condition for the radiation equation, Eq. (3.54).

The calculation of the convective heat flux depends on whether one is performing a Direct Numerical Simulation (DNS) or a Large Eddy Simulation (LES). In a DNS calculation, the convective heat flux to a solid surface $\dot{q}''_c$ is obtained directly from the gas temperature gradient at the boundary

$$\dot{q}''_c = -k\,\frac{\partial T}{\partial n} \tag{3.58}$$

where n is the spatial coordinate pointing into the solid. In an LES calculation, the convective heat flux to the surface is obtained from a combination of natural and forced convection correlations

$$\dot{q}''_c = h\,\Delta T \quad \mathrm{W/m^2} \quad ; \quad h = \max\left[C\,|\Delta T|^{\frac{1}{3}} \quad , \quad \frac{k}{L}\,0.037\,\mathrm{Re}^{\frac{4}{5}}\,\mathrm{Pr}^{\frac{1}{3}}\right] \quad \mathrm{W/m^2/K} \tag{3.59}$$

where ΔT is the difference between the wall and the gas temperature (taken at the center of the grid cell abutting the wall), C is the coefficient for natural convection (1.43 for a horizontal surface and 0.95 for a vertical surface) [17], L is a characteristic length related to the size of the physical obstruction, k is the thermal conductivity of the gas, and the Reynolds Re and Prandtl Pr numbers are based on the gas flowing past the obstruction. Since the Reynolds number is proportional to the characteristic length, L, the heat transfer coefficient is weakly related to L. For this reason, L is taken to be 1 m for most calculations.

3.5.2 Thermoplastic Fuels

If it is assumed that the pyrolysis of the solid material occurs at the surface, or if no pyrolysis occurs at all, the treatment of boundary is as follows.

If the surface material is assumed to be thermally-thick, a one-dimensional heat conduction equation for the material temperature, $T_s(x,t)$, is applied in the direction x pointing into the solid (the point $x = 0$ represents the surface)

$$\rho_s\,c_s\,\frac{\partial T_s}{\partial t} = \frac{\partial}{\partial x}\left(k_s\frac{\partial T_s}{\partial x}\right) \quad ; \quad -k_s\frac{\partial T_s}{\partial x}(0,t) = \dot{q}''_c + \dot{q}''_r - \dot{m}''\,\Delta H_v \tag{3.60}$$

where ρ_s, c_s and k_s are the temperature-dependent density, specific heat and conductivity of the material; $\dot{q}''_c$ is the convective and $\dot{q}''_r$ is the (net) radiative heat flux at the surface, $\dot{m}''$ is the mass loss rate of fuel and ΔH_v is the heat of vaporization. It is assumed that fuel pyrolysis takes place at the surface, thus the heat required to vaporize fuel is extracted from the incoming energy flux. The pyrolysis rate is given by an Arrhenius expression

$$\dot{m}'' = A\,\rho_s\,e^{-E_A/RT} \tag{3.61}$$

R is the universal gas constant. The value of the pre-exponential factor A and the activation energy E_A can be prescribed so that the material burns in the neighborhood of a prescribed temperature. The actual burning rate is governed by the overall energy balance in the solid. These parameters are often difficult to obtain for

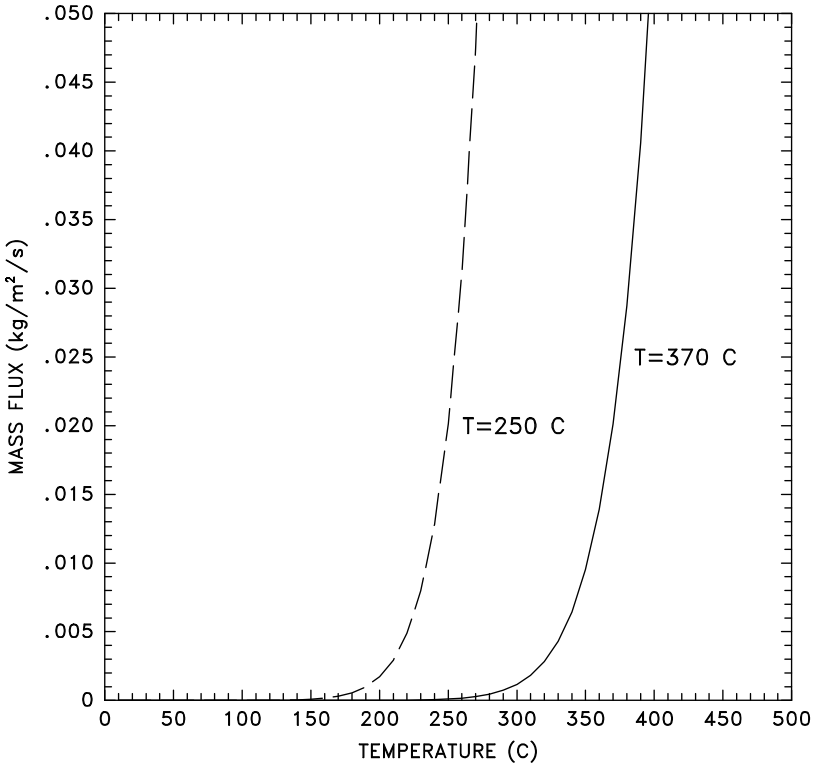

Figure 3.3: Fuel pyrolysis rates for two given "ignition" temperatures. See Eq. 3.61.

real fuels; the intent of using the given expression for the mass loss rate is to mimic the behavior of burning objects when details of their pyrolysis mechanisms are unknown. Figure 3.3 displays a few plots of the mass flux versus temperature for two different temperatures.

If the surface material is assumed to be thermally-thin, that is, its temperature is assumed uniform across its width, $T_s(t)$ is affected by gains and losses due to convection, radiation and pyrolysis. The thermal lag of the material is a function of the product of its density, specific heat and thickness δ

$$\frac{dT_s}{dt} = \frac{\dot{q}''_c + \dot{q}''_r - \dot{m}''\,\Delta H_v}{\rho_s c_s \delta} \tag{3.62}$$

The convective and radiative fluxes are summed over the front and back surfaces of the thin fuel. Unless otherwise specified, the back surface is assumed to face an ambient temperature void. Note that the individual values of the parameters ρ_s, c_s and δ are not as important as their product, thus often in the literature and in the computer program, the three values are lumped together as a product. The pyrolysis rate for a thermally-thin fuel is the same as for a thermally-thick; see Eq. 3.61.

3.5.3 Liquid Fuels

The rate at which liquid fuel evaporates when burning is a function of the liquid temperature and the concentration of fuel vapor above the pool surface. Equilibrium is reached when the partial pressure of the fuel vapor above the surface equals the Clausius-Clapeyron pressure

$$p_{cc} = p_0 \exp\left[-\frac{h_v M_f}{\mathcal{R}}\left(\frac{1}{T_s} - \frac{1}{T_b}\right)\right] \tag{3.63}$$

where h_v is the heat of vaporization, M_f is the molecular weight, T_s is the surface temperature, and T_b is the boiling temperature of the fuel [41].

For simplicity, the liquid fuel itself is treated like a thermally-thick solid for the purpose of computing the heat conduction. There is no computation of the convection of the liquid within the pool.

3.5.4 Charring Fuels

The heat transfer and pyrolysis of charring materials like wood are described using a one-dimensional model, originally developed by Atreya [42], and further developed by Ritchie *et al.* [43]. To simplify the original model, the pyrolysis is assumed to take place over an infinitesimally thin front. The model includes the conduction of heat inside the material, the evaporation of moisture and the degradation of the virgin material to gaseous fuel and char. The volatile gases are instantaneously transported to the surface. The governing equation for energy is

$$\overline{\rho c}\,\frac{\partial T_s}{\partial t} = \frac{\partial}{\partial x} k_s \frac{\partial T_s}{\partial x} + \frac{\partial \rho_s}{\partial t}\,\left[\Delta H_{pyr} - C(T-T_0)\right] + \frac{\partial \rho_m}{\partial t}\,\left[\Delta H_{ev} - D(T-T_0)\right] \tag{3.64}$$

where ρ_s is the total density of the solid and ρ_m is the moisture density. ΔH_{pyr} and ΔH_{ev} are the heats of pyrolysis and water vaporization, respectively. The boundary condition on the surface is

$$-k_s \frac{\partial T_s}{\partial x}(0,t) = \dot{q}''_c + \dot{q}''_r \tag{3.65}$$

Notice that the energy required to pyrolyze the fuel is not extracted from the incoming heat flux, as is done in the thermoplastic model, but rather the energy is drawn from inside the material at the point where the pyrolysis is occurring.

The coefficients C and D are defined

$$C = \frac{\rho_{s0}\overline{c_{p,s0}} - \rho_{char}\overline{c_{p,char}}}{\rho_{s0} - \rho_{char}} - \overline{c_{p,g}} \quad ; \quad D = \overline{c_{p,m}} - \overline{c_{p,g}} \tag{3.66}$$

where the subscripts $s0$ and *char* refer to the virgin material and char, and the subscripts g and m refer to the gaseous products of pyrolysis and the moisture. An overbar denotes the average value for the quantity between the temperature T and ambient temperature T_0.

The pyrolysis rate of the material is modeled with a single first order Arrhenius reaction

$$\dot{m}'' = A\,(\rho_{s0} - \rho_{char})\,e^{-E_A/RT} \tag{3.67}$$

The coefficients A and E_A are chosen so that the pyrolysis takes place very close to the desired pyrolysis temperature. The pyrolysis is assumed to take place over a thin front moving inside the material. The velocity of the front is given by

$$v = \frac{\dot{m}''}{\rho_{s0} - \rho_{char}} \tag{3.68}$$

and the front moves a distance $\Delta x = v\,\Delta t$. The evaporation rate of moisture is modeled in a similar manner.

The following definitions are used to calculate the thermal properties of the material during the drying and charring processes.

$$\overline{\rho c} = \rho_a c_{p,s0} + \rho_c c_{p,char} + \rho_m c_{p,m} \quad ; \quad k_s = k_{s0}\frac{\rho_a}{\rho_{s0}} + k_{char}\frac{\rho_c}{\rho_{char}} \tag{3.69}$$

$$\rho_a = \rho_{s0}\frac{\rho_s - \rho_{char}}{\rho_{s0} - \rho_{char}} \quad ; \quad \rho_c = \rho_s - \rho_a \tag{3.70}$$

where the thermal properties of the virgin material and char may be temperature dependent.

The selection of the proper material properties and pyrolysis coefficients is a difficult task. To reduce the uncertainty related to the coefficients of the pyrolysis rate, a thin pyrolysis front is assumed so that the burning rate is controlled mainly by the heat of pyrolysis and the heat transfer inside the material.

3.6 Sprinklers

Simulating the effects of a sprinkler spray involves a number of pieces: predicting activation, computing the droplet trajectories and tracking the water as it drips onto the burning commodity.

3.6.1 Sprinkler Activation

The temperature of the sensing element of a given sprinkler is estimated from the differential equation put forth by Heskestad and Bill [44], with the addition of a term to account for the cooling of the link by water droplets in the gas stream from previously activated sprinklers

$$\frac{dT_l}{dt} = \frac{\sqrt{|\mathbf{u}|}}{\mathrm{RTI}}(T_g - T_l) - \frac{C}{\mathrm{RTI}}(T_l - T_m) - \frac{C_2}{\mathrm{RTI}}\beta|\mathbf{u}| \tag{3.71}$$

Here T_l is the link temperature, T_g is the gas temperature in the neighborhood of the link, T_m is the temperature of the sprinkler mount (assumed ambient), and β is the volume fraction of (liquid) water in the gas stream. The sensitivity of the detector is characterized by the value of RTI. The amount of heat conducted away from the link by the mount is indicated by the "C-Factor", C. The constant C_2 has been empirically determined by DiMarzo and co-workers [45, 46, 47] to be 6×10^6 K/(m/s)$^{\frac{1}{2}}$, and its value is relatively constant for different types of sprinklers.

3.6.2 Sprinkler Droplet Size Distribution

Once activation is predicted, a sampled set of spherical water droplets is tracked from the sprinkler to either the floor or the burning commodity. In order to compute the droplet trajectories, the initial size and velocity of each droplet must be prescribed. This is done in terms of random distributions. The initial droplet size distribution of the sprinkler spray is expressed in terms of its Cumulative Volume Fraction (CVF), a function that relates the fraction of the water volume (mass) transported by droplets less than a given diameter. Researchers at Factory Mutual have suggested that the CVF for an industrial sprinkler may be represented by a combination of log-normal and Rosin-Rammler distributions [48]

$$F(d) = \begin{cases} \frac{1}{\sqrt{2\pi}} \int_0^d \frac{1}{\sigma d'} e^{-\frac{[\ln(d'/d_m)]^2}{2\sigma^2}} \, dd' & (d \le d_m) \\ 1 - e^{-0.693\left(\frac{d}{d_m}\right)^\gamma} & (d_m < d) \end{cases} \tag{3.72}$$

where d_m is the median droplet diameter (*i.e.* half the mass is carried by droplets with diameters of d_m or less), and γ and σ are empirical constants equal to about 2.4 and 0.6, respectively [2]. The median drop diameter is a function of the sprinkler orifice diameter, operating pressure, and geometry. Research at Factory Mutual has yielded a correlation for the median droplet diameter [49]

$$\frac{d_m}{D} \propto \mathrm{We}^{-\frac{1}{3}} \tag{3.73}$$

where D is the orifice diameter of the sprinkler. The Weber number, the ratio of inertial forces to surface tension forces, is given by

$$\mathrm{We} = \frac{\rho_w U^2 D}{\sigma_w} \tag{3.74}$$

where ρ_w is the density of water, U is the water discharge velocity, and σ_w is the water surface tension (72.8×10^{-3} N/m at 20 °C). The discharge velocity can be computed from the mass flow rate, which is a

[2] The Rosin-Rammler and log-normal distributions are smoothly joined if $\sigma = 2/(\sqrt{2\pi}\,(\ln 2)\,\gamma) = 1.15/\gamma$.

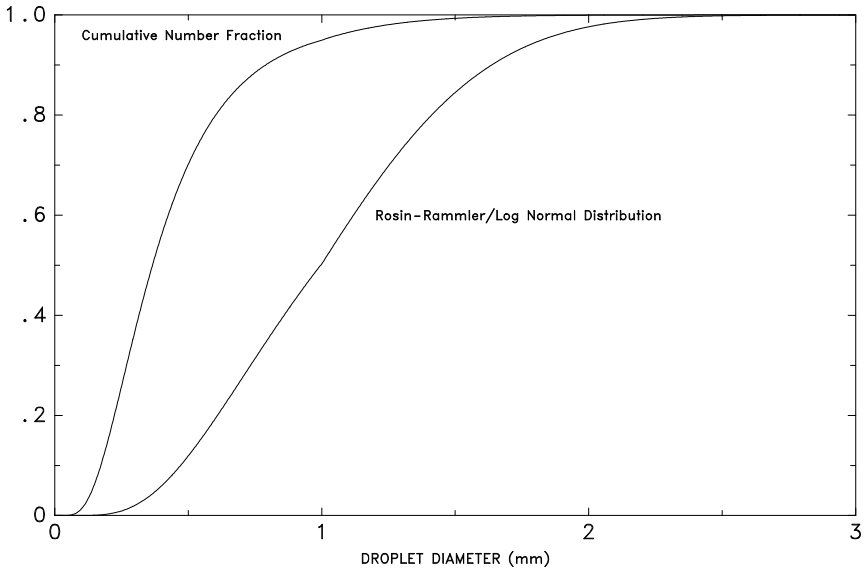

Figure 3.4: Cumulative Volume Fraction and Cumulative Number Fraction functions of the droplet size distribution from a typical industrial-scale sprinkler. The median diameter d_m is 1 mm, $\sigma = 0.6$ and $\gamma = 2.4$.

function of the sprinkler's operating pressure and K-Factor. FM reports that the constant of proportionality in Eq. (3.73) appears to be independent of flow rate and operating pressure. Three different sprinklers were tested in their study with orifice diameters of 16.3 mm, 13.5 mm, 12.7 mm and the constants were approximately 4.3, 2.9, 2.3, respectively. The strike plates of the two smaller sprinklers were notched, while that of the largest sprinkler was not [49].

In the numerical algorithm, the size of the sprinkler droplets are chosen to mimic the Rosin-Rammler/log-normal distribution. A Probability Density Function (PDF) for the droplet diameter is defined

$$f(d) = \frac{F'(d)}{d^3} \Big/ \int_0^\infty \frac{F'(d')}{d'^3}\, dd' \tag{3.75}$$

Droplet diameters are randomly selected by equating the Cumulative Number Fraction of the droplet distribution with a uniformly distributed random variable U

$$U(d) = \int_0^d f(d')\, dd' \tag{3.76}$$

Figure 3.4 displays typical Cumulative Volume Fraction and Cumulative Number Fraction functions.

Every droplet from a given sprinkler is not tracked. Instead, a sampled set of the droplets is tracked. Typically, 1,000 droplets per sprinkler per second are tracked (50 droplets every 0.05 s, depending on user preference). The procedure for selecting droplet sizes is as follows: Suppose water is leaving the sprinkler at a mass flow rate of $\dot{m}$. Suppose also that the time interval for droplet insertion into the numerical simulation is δt, and the number of droplets inserted each time interval is N. Choose N uniformly distributed random numbers between 0 and 1, call them U_i, obtain N droplet diameters d_i based on the given droplet size distribution (Eq. (3.76), and then compute a weighting constant C from the mass balance

$$\dot{m}\, \delta t = C \sum_{i=1}^{N} \frac{4}{3} \pi \rho_w \left(\frac{d_i}{2} \right)^3 \tag{3.77}$$

The mass and heat tranferred from each droplet will be multiplied by the weighting factor C.

3.6.3 Sprinkler Droplet Trajectory in Air

For a sprinkler spray, the force term **f** in Eq. (3.3) represents the momentum transferred from the water droplets to the gas. It is obtained by summing the force transferred from each droplet in a grid cell and dividing by the cell volume

$$\mathbf{f} = \frac{1}{2}\frac{\sum \rho C_D \pi r_d^2 (\mathbf{u}_d - \mathbf{u})|\mathbf{u}_d - \mathbf{u}|}{\delta x\, \delta y\, \delta z} \tag{3.78}$$

where C_D is the drag coefficient, r_d is the droplet radius, $\mathbf{u}_d$ is the velocity of the droplet, $\mathbf{u}$ is the velocity of the gas, ρ is the density of the gas, and $\delta x\, \delta y\, \delta z$ is the volume of the grid cell. The trajectory of an individual droplet is governed by the equation

$$\frac{d}{dt}(m_d \mathbf{u}_d) = m_d\, \mathbf{g} - \frac{1}{2}\rho\, C_D\, \pi r_d^2\, (\mathbf{u}_d - \mathbf{u})|\mathbf{u}_d - \mathbf{u}| \tag{3.79}$$

where m_d is the mass of the droplet. The drag coefficient is a function of the local Reynolds number

$$C_D = \begin{cases} 24/\mathrm{Re} & \mathrm{Re} < 1 \\ 24\left(1 + 0.15\,\mathrm{Re}^{0.687}\right)/\mathrm{Re} & 1 < \mathrm{Re} < 1000 \\ 0.44 & 1000 < \mathrm{Re} \end{cases} \tag{3.80}$$

$$\mathrm{Re} = \frac{\rho\, |\mathbf{u}_d - \mathbf{u}|\, 2 r_d}{\mu} \tag{3.81}$$

where μ is the dynamic viscosity of air.

3.6.4 Sprinkler Droplet Transport on a Surface

When a water droplet hits a solid horizontal surface, it is assigned a random horizontal direction and moves at a fixed velocity until it reaches the edge, at which point it drops straight down at the same fixed velocity. This "dripping" velocity has been measured to be on the order of 0.5 m/s [50, 51]. Penetration of water into porous materials is handled very crudely by assigning a fraction of the water droplets that strike a solid horizontal surface to go straight through the solid at a slow velocity. Neither the fraction nor the velocity has been validated.

3.6.5 Mass and Energy Transfer from Droplets

The evaporation of water droplets is handled semi-empirically. A water droplet suspended in air will evaporate as a function of the droplet equilibrium vapor mass fraction, the local gas phase vapor mass fraction, the heat transfer to the droplet, and the droplet's motion relative to the gas. A correlation for the mass loss rate of a droplet that involves these parameters is given here [52]

$$\frac{dm_d}{dt} = -2\pi\, r_d\, \mathrm{Sh}\, \rho D\, (Y_d - Y_g) \tag{3.82}$$

The subscripts d and g refer to the droplet and gas, respectively, m_d is the droplet mass, D is the diffusion coefficient for water vapor into air, Y is the water vapor mass fraction, and Sh is the droplet Sherwood number, given by a correlation involving the Reynolds and Schmidt numbers

$$\mathrm{Sh} = 2 + 0.6\, \mathrm{Re}^{\frac{1}{2}}\, \mathrm{Sc}^{\frac{1}{3}} \tag{3.83}$$

The vapor mass fraction of the gas, Y_g, is obtained from the overall set of mass conservation equations and the vapor mass fraction of the droplet is obtained from the Clausius-Clapeyron equation

$$X_d = \exp\left[\frac{h_v M_w}{\mathcal{R}}\left(\frac{1}{T_b} - \frac{1}{T_d}\right)\right] \quad ; \quad Y_d = \frac{X_d}{X_d(1 - M_a/M_w) + M_a/M_w} \tag{3.84}$$

where X_d is the droplet water vapor volume fraction, h_v is the heat of vaporization, M_w is the molecular weight of water, M_a is the molecular weight of air, $\mathcal{R}$ is the gas constant, T_b is the boiling temperature of water and T_d is the droplet temperature.

In addition to calculating the mass transfer due to evaporation, the transfer of energy must also be calculated. The droplet heats up due to the convective heat transfer across the surface of the droplet minus the energy required to evaporate water

$$m_d\, c_{p,w}\, \frac{dT_d}{dt} = A_d\, h_d\, (T_g - T_d) - \frac{dm_d}{dt}\, h_v \tag{3.85}$$

Here $c_{p,w}$ is the specific heat of water, $A_d = 4\pi r_d^2$ is the surface area of the droplet, h_d is the heat transfer coefficient, given by

$$h_d = \frac{\mathrm{Nu}\, k}{2r_d} \quad ; \quad \mathrm{Nu} = 2 + 0.6\, \mathrm{Re}^{\frac{1}{2}}\, \mathrm{Pr}^{\frac{1}{3}} \tag{3.86}$$

Nu is the Nusselt number, k is the thermal conductivity of air, and the Prandtl number, Pr, is about 0.7 for air. The Sherwood number, Sh, is analogous to the Nusselt number, with the Schmidt number about 0.6 compared to the 0.7 for the Prandtl number.

Finally, the exchange of mass and energy between the droplets and the gas results in an additional term that must be added to the expression for the divergence, Eq. (3.8)

$$\nabla \cdot \mathbf{u} = \quad \ldots \quad + \frac{\mathcal{R}}{\gamma\, p_0} \left(\rho \sum (Y_i/M_i)\, \frac{\partial T}{\partial t} + \frac{T}{M_w} \dot{m}_w''' \right) \tag{3.87}$$

where $\dot{m}_w'''$ is the water evaporation rate per unit volume. The liquid water droplets are assumed to occupy no volume, simplifying the analysis.

3.6.6 Interaction of Droplets and Radiation

The attenuation of thermal radiation by water droplets is an important consideration, especially for water mist systems [53]. Water droplets attenuate thermal radiation through a combination of scattering and absorption [54]. The radiation-droplet interaction must therefore be solved for both the accurate prediction of the radiation field and for the droplet energy balance.

If the gas phase absorption and emission in Eq. (3.47) are temporarily neglected for simplicity, the radiative transport equation becomes

$$\mathbf{s} \cdot \nabla I_\lambda(\mathbf{x}, \mathbf{s}) = -\left[\kappa_d(\mathbf{x}, \lambda) + \sigma_d(\mathbf{x}, \lambda)\right] I(\mathbf{x}, \mathbf{s}) + \kappa_d(\mathbf{x}, \lambda)\, I_{b,d}(\mathbf{x}, \lambda) + \frac{\sigma_d(\mathbf{x}, \lambda)}{4\pi} \int_{4\pi} \Phi(\mathbf{s}, \mathbf{s}')\, I_\lambda(\mathbf{x}, \mathbf{s}')\, d\Omega' \tag{3.88}$$

where κ_d is the droplet absorption coefficient, σ_d is the droplet scattering coefficient and $I_{b,d}$ is the emission term of the droplets. $\Phi(\mathbf{s}, \mathbf{s}')$ is a scattering phase function that gives the scattered intensity from direction $\mathbf{s}'$ to $\mathbf{s}$. The local absorption and scattering coefficients are calculated from the local droplet number density $N(\mathbf{x})$ and mean diameter $d_m(\mathbf{x})$ as

$$\begin{aligned} \kappa_d(\mathbf{x}, \lambda) &= N(\mathbf{x}) \textstyle\int_0^\infty f(r, d_m(\mathbf{x}))\, C_a(r, \lambda)\, dr \\ \sigma_d(\mathbf{x}, \lambda) &= N(\mathbf{x}) \textstyle\int_0^\infty f(r, d_m(\mathbf{x}))\, C_s(r, \lambda)\, dr \end{aligned} \tag{3.89}$$

where r is the droplet radius and C_a and C_s are absorption and scattering cross sections, respectively, given by Mie theory. The droplet number density function $f(r, d_m)$ is assumed to have the same form as the droplet size distribution, but a different mean.

An accurate computation of the in-scattering integral on the right hand side of Eq (3.88) would be extremely time consuming. It is here approximated by dividing the total 4π solid angle to a "forward angle"

$\delta\Omega^l$ and "ambient angle" $\delta\Omega^* = 4\pi - \delta\Omega^l$. For compatibility with the FVM solver, $\delta\Omega^l$ is set equal to the control angle given by the angular discretization. However, it is assumed to be symmetric around the center of the control angle. Within $\delta\Omega^l$ the intensity is $I_\lambda(\mathbf{x},\mathbf{s})$ and elsewhere it is approximated as

$$U^*(\mathbf{x},\lambda) = \frac{U(\mathbf{x},\lambda) - \delta\Omega^l I_\lambda(\mathbf{x},\mathbf{s})}{\delta\Omega^*} \tag{3.90}$$

where $U(\mathbf{x})$ is the total integrated intensity. The in-scattering integral can now be written as

$$\frac{\sigma_d(\mathbf{x},\lambda)}{4\pi}\int_{4\pi}\Phi(\mathbf{s},\mathbf{s}')\,I_\lambda(\mathbf{x},\mathbf{s}')\,d\Omega' = \sigma_d(\mathbf{x},\lambda)\left[\chi_f\,I_\lambda(\mathbf{x},\mathbf{s}) + (1-\chi_f)U^*(\mathbf{x})\right] \tag{3.91}$$

where $\chi_f = \chi_f(r,\lambda)$ is a fraction of the total intensity originally within the solid angle $\delta\Omega^l$ that is scattered into the same angle $\delta\Omega^l$. Defining now an effective scattering coefficient section

$$\bar{\sigma}_d(\mathbf{x},\lambda) = \frac{4\pi N(\mathbf{x})}{4\pi - \delta\Omega^l}\int_0^\infty (1-\chi_f)\,C_s(r,\lambda)\,dr \tag{3.92}$$

the spray RTE becomes

$$\mathbf{s}\cdot\nabla I_\lambda(\mathbf{x},\mathbf{s}) = -\left[\kappa_d(\mathbf{x},\lambda) + \bar{\sigma}_d(\mathbf{x},\lambda)\right]I(\mathbf{x},\mathbf{s}) + \kappa_d(\mathbf{x},\lambda)\,I_{b,d}(\mathbf{x},\lambda) + \frac{\bar{\sigma}_d(\mathbf{x},\lambda)}{4\pi}U(\mathbf{x},\lambda) \tag{3.93}$$

This equation can be integrated over the spectrum to get the band specific RTE's. The procedure is exactly the same as what is used for the gas phase RTE. After the band integrations, the spray RTE for band *n* becomes

$$\mathbf{s}\cdot\nabla I_n(\mathbf{x},\mathbf{s}) = -\left[\kappa_{d,n}(\mathbf{x}) + \bar{\sigma}_{d,n}(\mathbf{x})\right]I_n(\mathbf{x},\mathbf{s}) + \kappa_{d,n}(\mathbf{x})\,I_{b,d,n}(\mathbf{x}) + \frac{\bar{\sigma}_d(\mathbf{x},\lambda)}{4\pi}U_n(\mathbf{x}) \tag{3.94}$$

where the source function is based on the average droplet temperature within a cell. The absorption and scattering cross sections and the scattering phase function are calculated using the MieV code developed by Wiscombe [55]. Both κ_d and $\bar{\sigma}_d$ are averaged over the possible droplet radii and wavelength before the actual simulation. A single constant temperature is used in the wavelength averaging. This "radiation temperature" T_{rad} should be selected to represent a typical radiating flame temperature. A value 1173 K is used by default. The averaged quantities, being now functions of the droplet mean diameter only, are saved in one-dimensional arrays. During the simulation, the local properties are calculated as a table lookup using the local mean droplet diameter [56]. Details of the computation are given in Section 3.7.8.

3.6.7 Fire Suppression by Water

The above two sections describe heat transfer from a droplet of water to a hot gas, a hot solid, or both. Although there is some uncertainty in the values of the respective heat transfer coefficients, the fundamental physics are fairly well understood. However, when the water droplets encounter burning surfaces, simple heat transfer correlations become more difficult to apply. The reason for this is that the water is not only cooling the surface and the surrounding gas, but it is also changing the pyrolysis rate of the fuel. If the surface of the fuel is planar, it is possible to characterize the decrease in the pyrolysis rate as a function of the decrease in the total heat feedback to the surface. Unfortunately, most fuels of interest in fire applications are multi-component solids with complex geometry at scales unresolvable by the computational grid.

To date, most of the work in this area has been performed at Factory Mutual. An important paper on the subject is by Yu *et al.* [57]. The authors consider dozens of rack storage commodity fires of different geometries and water application rates, and characterize the suppression rates in terms of a few global

parameters. Their analysis yields an expression for the total heat release rate from a rack storage fire after sprinkler activation

$$\dot{Q} = \dot{Q}_0 \, e^{-k(t-t_0)} \tag{3.95}$$

where $\dot{Q}_0$ is the total heat release rate at the time of application t_0, and k is a fuel-dependent constant. For the FMRC Standard Plastic commodity k is given as

$$k = 0.716 \, \dot{m}''_w - 0.0131 \quad \mathrm{s}^{-1} \tag{3.96}$$

where $\dot{m}''_w$ is the flow rate of water impinging on the box tops, divided by the area of exposed surface (top and sides). It is expressed in units of kg/m^2/s. For the Class II commodity, k is given as

$$k = 0.536 \, \dot{m}''_w - 0.0040 \quad \mathrm{s}^{-1} \tag{3.97}$$

Unfortunately, this analysis is based on global water flow and burning rates. Equation (3.95) accounts for both the cooling of non-burning surfaces as well as the decrease in heat release rate of burning surfaces. In the FDS model, the cooling of unburned surfaces and the reduction in the heat release rate are computed locally, thus it is awkward to apply a global suppression rule. However, the exponential nature of suppression by water is observed both locally and globally, thus it is assumed that the local burning rate of the fuel can be expressed in the form [50, 51]

$$\dot{m}''_f(t) = \dot{m}''_{f,0}(t) \, e^{-\int k(t)\,dt} \tag{3.98}$$

Here $\dot{m}''_{f,0}(t)$ is the burning rate per unit area of the fuel when no water is applied and $k(t)$ is a linear function of the local water mass per unit area, m''_w, expressed in units of kg/m^2,

$$k(t) = a \, m''_w(t) \quad \mathrm{s}^{-1} \tag{3.99}$$

Note that a is an empirical constant.

3.7 Numerical Method

First the equations that are being solved are presented. Each of the conservation equations emphasize the importance of the velocity divergence and vorticity fields, as well as the close relationship between the thermally expandable fluid equations [9] and the Boussinesq equations for which the authors have developed highly efficient solution procedures [58, 59]. All spatial derivatives are approximated by second order finite differences and the flow variables are updated in time using an explicit second order predictor-corrector scheme.

3.7.1 Simplified Equations

Regardless of whether one is performing an LES or a DNS calculation, the overall solution algorithm is the same.

Conservation of Mass

$$\frac{\partial \rho}{\partial t} + \mathbf{u} \cdot \nabla \rho = -\rho \nabla \cdot \mathbf{u} \tag{3.100}$$

Conservation of Species

$$\frac{\partial \rho Y_l}{\partial t} + \mathbf{u} \cdot \nabla \rho Y_l = -\rho Y_l \nabla \cdot \mathbf{u} + \nabla \cdot \rho D \nabla Y_l + \dot{m}_l''' \tag{3.101}$$

Conservation of Momentum

$$\frac{\partial \mathbf{u}}{\partial t} + \mathbf{u} \times \omega + \nabla \mathcal{H} = \frac{1}{\rho} \left((\rho - \rho_\infty)\mathbf{g} + \mathbf{f} + \nabla \cdot \tau \right) \tag{3.102}$$

Divergence Constraint

$$\nabla \cdot \mathbf{u} = \frac{1}{\rho c_p T} \left(\nabla \cdot k \nabla T + \nabla \cdot \sum_l \int c_{p,l} dT \; \rho D_l \nabla Y_l - \nabla \cdot \mathbf{q}_r + \dot{q}''' \right) + \left(\frac{1}{\rho c_p T} - \frac{1}{p_0} \right) \frac{dp_0}{dt} \tag{3.103}$$

Equation of State

$$p_0(t) = \rho T \mathcal{R} \sum_l Y_l / M_l \tag{3.104}$$

Notice that the source terms from the energy conservation equation have been incorporated into the divergence and ultimately are involved in the mass conservation equation. The temperature is found from the density and background pressure via the equation of state.

3.7.2 Temporal Discretization

All calculations start with ambient initial conditions. At the beginning of each time step, the quantities ρ^n, Y_i^n, $\mathbf{u}^n$, $\mathcal{H}^n$, and p_0^n are known. All other quantities can be derived from them. Note that the superscript $(n+1)_e$ refers to an estimate of the value of the quantities at the $(n+1)$st time step.

1. The thermodynamic quantities ρ, Y_i, and p_0 are estimated at the next time step with an explicit Euler step. For example, the density is estimated

$$\rho^{(n+1)_e} = \rho^n - \delta t (\mathbf{u}^n \cdot \nabla \rho^n + \rho^n \nabla \cdot \mathbf{u}^n) \tag{3.105}$$

   The divergence $(\nabla \cdot \mathbf{u})^{(n+1)_e}$ is formed from these estimated thermodynamic quantities. The normal velocity components at boundaries that are needed to form the divergence are assumed known.

2. A Poisson equation for the pressure is solved with a direct solver

$$\nabla^2 \mathcal{H}^n = -\frac{(\nabla \cdot \mathbf{u})^{(n+1)_e} - (\nabla \cdot \mathbf{u})^n}{\delta t} - \nabla \cdot \mathbf{F}^n \tag{3.106}$$

Note that the vector **F** contains the convective, diffusive and force terms of the momentum equation. These will be described in detail below. Then the velocity is estimated at the next time step

$$\mathbf{u}^{(n+1)_e} = \mathbf{u}^n - \delta t \left(\mathbf{F}^n + \nabla \mathcal{H}^n\right) \tag{3.107}$$

Note that the divergence of the estimated velocity field is identically equal to the estimated divergence $(\nabla \cdot \mathbf{u})^{(n+1)_e}$ that was derived from the estimated thermodynamic quantities. The time step is checked at this point to ensure that

$$\delta t \max\left(\frac{\delta x}{|u|}, \frac{\delta y}{|v|}, \frac{\delta z}{|w|}\right) < 1 \quad ; \quad 2\,\delta t\,\nu\left(\frac{1}{\delta x^2} + \frac{1}{\delta y^2} + \frac{1}{\delta z^2}\right) < 1 \tag{3.108}$$

If the time step is too large, it is reduced so that it satisfies both constraints and the procedure returns to the beginning of the time step. If the time step satisfies the stability criteria, the procedure continues to the corrector step. See Section 3.7.10 for more details on stability.

3. The thermodynamic quantities ρ, Y_i, and p_0 are corrected at the next time step. For example, the density is corrected

$$\rho^{n+1} = \frac{1}{2}\left(\rho^n + \rho^{(n+1)_e} - \delta t(\mathbf{u}^{(n+1)_e} \cdot \nabla \rho^{(n+1)_e} + \rho^{(n+1)_e} \nabla \cdot \mathbf{u}^{(n+1)_e})\right) \tag{3.109}$$

The divergence $(\nabla \cdot \mathbf{u})^{(n+1)}$ is derived from the corrected thermodynamic quantities.

4. The pressure is recomputed using estimated quantities

$$\nabla^2 \mathcal{H}^{(n+1)_e} = -\frac{2(\nabla \cdot \mathbf{u})^{n+1} - (\nabla \cdot \mathbf{u})^{(n+1)_e} - (\nabla \cdot \mathbf{u})^n}{\delta t} - \nabla \cdot \mathbf{F}^{(n+1)_e} \tag{3.110}$$

The velocity is then corrected

$$\mathbf{u}^{n+1} = \frac{1}{2}\left[\mathbf{u}^n + \mathbf{u}^{(n+1)_e} - \delta t\left(\mathbf{F}^{(n+1)_e} + \nabla \mathcal{H}^{(n+1)_e}\right)\right] \tag{3.111}$$

Note again that the divergence of the corrected velocity field is identically equal to the corrected divergence.

3.7.3 Spatial Discretization

Spatial derivatives in the governing equations are written as second order accurate finite differences on a rectilinear grid. The overall domain is a rectangular box that is divided into rectangular grid cells. Each cell is assigned indices *i*, *j* and *k* representing the position of the cell in the *x*, *y* and *z* directions, respectively. Scalar quantities are assigned in the center of each grid cell, thus ρ^n_{ijk} is the density at the *n*th time step in the center of the cell whose indices are *i*, *j* and *k*. Vector quantities like velocity are assigned at cell faces, thus the *x* component of velocity *u* is defined at the faces whose normals are parallel to the *x*-axis, the *y* component *v* is defined at the faces whose normals are parallel to the *y*-axis, and the *z* component *w* is defined at the faces whose normals are parallel to the *z*-axis. The quantity u^n_{ijk} is the *x* component of velocity at the forward pointing face of the *ijk*th cell; $u^n_{i-1,jk}$ is at the backward pointing face of the *ijk*th cell.

3.7.4 Large Eddy vs. Direct Numerical Simulation

The major difference between an LES and a DNS calculation is the form of the viscosity, and the thermal and material diffusivities. For a Large Eddy Simulation, the dynamic viscosity is defined at cell centers

$$\mu_{ijk} = \rho_{ijk} (C_s \Delta)^2 |S| \tag{3.112}$$

where C_s is an empirical constant, $\Delta = (\delta x \delta y \delta z)^{\frac{1}{3}}$, and

$$|S|^2 = 2\left(\frac{\partial u}{\partial x}\right)^2 + 2\left(\frac{\partial v}{\partial y}\right)^2 + 2\left(\frac{\partial w}{\partial z}\right)^2 + \left(\frac{\partial u}{\partial y} + \frac{\partial v}{\partial x}\right)^2 + \left(\frac{\partial u}{\partial z} + \frac{\partial w}{\partial x}\right)^2 + \left(\frac{\partial v}{\partial z} + \frac{\partial w}{\partial y}\right)^2 - \frac{2}{3}(\nabla \cdot \mathbf{u})^2 \tag{3.113}$$

The quantity $|S|$ consists of second order spatial differences averaged at cell centers. The thermal conductivity and material diffusivity of the fluid are related to the viscosity by

$$k_{ijk} = \frac{c_{p,0}\,\mu_{ijk}}{\mathrm{Pr}} \quad ; \quad (\rho D)_{ijk} = \frac{\mu_{ijk}}{\mathrm{Sc}} \tag{3.114}$$

where Pr is the Prandtl number and Sc is the Schmidt number, both assumed constant. Note that the specific heat $c_{p,0}$ is that of the dominant species of the mixture. Based on simulations of smoke plumes, C_s is 0.20, Pr and Sc are 0.5. There are no rigorous justifications for these choices other than through comparison with experimental data [60].

The dynamic viscosity, thermal conductivity and diffusion coefficients for a DNS calculation are defined at cell centers

$$\mu_{ijk} = \sum_l Y_{l,ijk}\, \mu_l(T_{ijk}) \tag{3.115}$$

$$k_{ijk} = \sum_l Y_{l,ijk}\, k_l(T_{ijk}) \tag{3.116}$$

$$D_{l,ijk} = D_{l0}(T_{ijk}) \tag{3.117}$$

where the values for each individual species are approximated from kinetic theory [30]. The term D_{l0} is the binary diffusion coefficient for species l diffusing into the predominant species 0, usually nitrogen. It is often the case that the numerical grid is too coarse to resolve steep gradients in flow quantities when the temperature is near ambient. However, as the temperature increases and the diffusion coefficients increase in value, the situation improves. As a consequence, there is a provision in the numerical algorithm to place a lower bound on the viscous coefficients to avoid numerical instabilities at temperatures close to ambient.

3.7.5 The Mass Transport Equations

Due to the low Mach number approximation being used in the model, the mass and energy equations are combined by way of the divergence. The divergence of the flow field contains much of the fire-specific source terms described above.

Convective and Diffusive Transport

The density at the center of the ijkth cell is updated in time with the following predictor-corrector scheme. In the predictor step, the density at the $(n+1)$st time level is estimated based on information at the nth level

$$\frac{\rho_{ijk}^{(n+1)_e} - \rho_{ijk}^n}{\delta t} + (\mathbf{u} \cdot \nabla \rho)_{ijk}^n = -\rho_{ijk}^n (\nabla \cdot \mathbf{u})_{ijk}^n \tag{3.118}$$

Following the prediction of the velocity and background pressure at the $(n+1)$st time level, the density is corrected

$$\frac{\rho_{ijk}^{(n+1)} - \frac{1}{2}\left(\rho_{ijk}^{n} + \rho_{ijk}^{(n+1)_e}\right)}{\frac{1}{2}\delta t} + (\mathbf{u}\cdot\nabla\rho)_{ijk}^{(n+1)_e} = -\rho_{ijk}^{(n+1)_e}(\nabla\cdot\mathbf{u})_{ijk}^{(n+1)_e} \tag{3.119}$$

The species conservation equations are differenced the same way

$$\frac{(\rho Y_l)_{ijk}^{(n+1)_e} - (\rho Y_l)_{ijk}^{n}}{\delta t} + (\mathbf{u}\cdot\nabla\rho Y_l)_{ijk}^{n} = -(\rho Y_l)_{ijk}^{n}(\nabla\cdot\mathbf{u})_{ijk}^{n} + (\nabla\cdot\rho D\nabla Y_l)_{ijk}^{n} + \dot{m}_{ijk}^{'''} \tag{3.120}$$

at the predictor step, and

$$\frac{(\rho Y_l)_{ijk}^{(n+1)} - \frac{1}{2}\left((\rho Y_l)_{ijk}^{n} + (\rho Y_l)_{ijk}^{(n+1)_e}\right)}{\frac{1}{2}\delta t} + (\mathbf{u}\cdot\nabla\rho Y_l)_{ijk}^{(n+1)_e} = -(\rho Y_l)_{ijk}^{(n+1)_e}(\nabla\cdot\mathbf{u})_{ijk}^{(n+1)_e} + (\nabla\cdot\rho D\nabla Y_l)_{ijk}^{(n+1)_e} + \dot{m}_{ijk}^{'''} \tag{3.121}$$

at the corrector step.

The convective terms are written as upwind-biased differences in the predictor step and downwind-biased differences in the corrector step. In the expressions to follow, the symbol $\pm$ means $+$ in the predictor step and $-$ in the corrector step. The opposite is true for $\mp$.

$$\begin{aligned}(\mathbf{u}\cdot\nabla\rho)_{ijk} &= \frac{1\mp\varepsilon_u}{2}u_{ijk}\frac{\rho_{i+1,jk}-\rho_{ijk}}{\delta x} + \frac{1\pm\varepsilon_u}{2}u_{i-1,jk}\frac{\rho_{ijk}-\rho_{i-1,jk}}{\delta x} + \\ &\quad \frac{1\mp\varepsilon_v}{2}v_{ijk}\frac{\rho_{i,j+1,k}-\rho_{ijk}}{\delta y} + \frac{1\pm\varepsilon_v}{2}v_{i,j-1,k}\frac{\rho_{ijk}-\rho_{i,j-1,k}}{\delta y} + \\ &\quad \frac{1\mp\varepsilon_w}{2}w_{ijk}\frac{\rho_{ij,k+1}-\rho_{ijk}}{\delta z} + \frac{1\pm\varepsilon_w}{2}w_{ij,k-1}\frac{\rho_{ijk}-\rho_{ij,k-1}}{\delta z}\end{aligned} \tag{3.122}$$

$$\begin{aligned}(\mathbf{u}\cdot\nabla\rho Y_l)_{ijk} &= \frac{1\mp\varepsilon_u}{2}u_{ijk}\frac{(\rho Y_l)_{i+1,jk}-(\rho Y_l)_{ijk}}{\delta x} + \frac{1\pm\varepsilon_u}{2}u_{i-1,jk}\frac{(\rho Y_l)_{ijk}-(\rho Y_l)_{i-1,jk}}{\delta x} + \\ &\quad \frac{1\mp\varepsilon_v}{2}v_{ijk}\frac{(\rho Y_l)_{i,j+1,k}-(\rho Y_l)_{ijk}}{\delta y} + \frac{1\pm\varepsilon_v}{2}v_{i,j-1,k}\frac{(\rho Y_l)_{ijk}-(\rho Y_l)_{i,j-1,k}}{\delta y} + \\ &\quad \frac{1\mp\varepsilon_w}{2}w_{ijk}\frac{(\rho Y_l)_{ij,k+1}-(\rho Y_l)_{ijk}}{\delta z} + \frac{1\pm\varepsilon_w}{2}w_{ij,k-1}\frac{(\rho Y_l)_{ijk}-(\rho Y_l)_{ij,k-1}}{\delta z}\end{aligned} \tag{3.123}$$

Note that without the inclusion of the ε's, these are simple central difference approximations. The ε's are local Courant numbers, $\varepsilon_u = u\delta t/\delta x$, $\varepsilon_v = v\delta t/\delta y$, and $\varepsilon_w = w\delta t/\delta z$, where the velocity components are those that immediately follow. Their role is to bias the differencing upwind. Where the local Courant number is near unity, the difference becomes nearly fully upwinded. Where the local Courant number is much less than unity, the differencing is more centralized [61].

3.7.6 Discretizing the Divergence

The divergence in both the predictor and corrector step is discretized

$$(\nabla\cdot\mathbf{u})_{ijk} = \frac{1}{\rho T c_p}\left(\dot{q}_{ijk}^{'''} + (\nabla\cdot k\nabla T)_{ijk} + \sum_l(\nabla\cdot h_l\rho D\nabla Y_l)_{ijk}\right) + \left(\frac{1}{\rho T c_p} - \frac{1}{p_0}\right)\frac{dp_0}{dt} \tag{3.124}$$

The thermal and material diffusion terms are pure central differences, with no upwind or downwind bias, thus they are differenced the same way in both the predictor and corrector steps. For example, the thermal

conduction term is differenced as follows:

$$
\begin{aligned}
(\nabla \cdot k \nabla T)_{ijk} \quad = \quad & \frac{1}{\delta x}\left[k_{i+\frac{1}{2},jk}\frac{T_{i+1,jk}-T_{ijk}}{\delta x} - k_{i-\frac{1}{2},jk}\frac{T_{ijk}-T_{i-1,jk}}{\delta x}\right] + \\
& \frac{1}{\delta y}\left[k_{i,j+\frac{1}{2},k}\frac{T_{i,j+1,k}-T_{ijk}}{\delta y} - k_{i,j-\frac{1}{2},k}\frac{T_{ijk}-T_{i,j-1,k}}{\delta y}\right] + \\
& \frac{1}{\delta z}\left[k_{ij,k+\frac{1}{2}}\frac{T_{ij,k+1}-T_{ijk}}{\delta z} - k_{ij,k-\frac{1}{2}}\frac{T_{ijk}-T_{ij,k-1}}{\delta z}\right]
\end{aligned} \tag{3.125}
$$

The temperature is extracted from the density via the equation of state

$$
T_{ijk} = \frac{p_0}{\rho_{ijk}\mathcal{R}\sum_{l=0}^{N}(Y_{l,ijk}/M_l)} \tag{3.126}
$$

Because only species 1 through N are explicitly computed, the summation is rewritten

$$
\sum_{l=0}^{N}\frac{Y_{l,ijk}}{M_l} = \frac{1}{M_0} + \sum_{l=1}^{N}\left(\frac{1}{M_l}-\frac{1}{M_0}\right)Y_l \tag{3.127}
$$

In isothermal calculations involving multiple species, the density can be extracted from the average molecular weight

$$
\rho_{ijk} = \frac{p_0}{T_\infty \mathcal{R}\sum_{l=0}^{N} Y_{l,ijk}/M_l} \tag{3.128}
$$

Again, because only species 1 through N are explicitly computed, this expression can be written

$$
\rho_{ijk} = \frac{M_0\, p_0}{T_\infty \mathcal{R}} + \sum_{l=1}^{N}\left(1-\frac{M_0}{M_l}\right)(\rho Y_l)_{ijk} \tag{3.129}
$$

Heat Release Rate (Mixture Fraction)

When using the mixture fraction-based combustion model, we must extract the local heat release rate per unit volume from the computed mixture fraction field. Ideally, the reaction of fuel and oxygen is assumed to occur at an infinitesimally thin sheet where $Z = Z_f$, the stoichiometric value of the mixture fraction. In the finite difference calculation, the location of the sheet must be determined, and then the energy that is released must be distributed to the appropriate grid cells. To motivate the numerical procedure, we will work with the exact (*i.e.* non-discrete) form of the relevant expressions.

The heat release rate per unit area of flame sheet is

$$
\dot{q}'' = \Delta H_O \left.\frac{dY_O}{dZ}\right|_{Z<Z_f} \rho D\, \nabla Z \cdot \mathbf{n} \tag{3.130}
$$

where $\mathbf{n}$ is the outward facing unit normal. Note that both dY_O/dZ and $\nabla Z \cdot \mathbf{n}$ are negative. The finite difference approximation for this expression must be accurate to ensure that the integrated heat release rate over the flame sheet is consistent with the prescribed fuel flow rate. For the sake of simplicity, take a simple gas burner with a constant fuel flow rate $\dot{m}_b$. At any instant in time, the mass flow of fuel (plus fuel by-products) through the flame sheet above the burner is given by

$$
\dot{m}_f(t) = \int_f \rho Z \mathbf{u}\cdot\mathbf{n}\, dS - \int_f \rho D\, \nabla Z \cdot \mathbf{n}\, dS \tag{3.131}
$$

where the surface integrals are over the flame sheet whose normal direction points away from the fuel side. Averaged over time, the mass of fuel and its by-products flowing through the flame will equal the mass of fuel flowing out of the burner. At the flame sheet ($Z = Z_f$) the convective term can be simplified

$$\int_f \rho Z \mathbf{u}\cdot\mathbf{n}\, dS = Z_f \int_f \rho \mathbf{u}\cdot\mathbf{n}\, dS \quad ; \quad Z_f = \frac{Y_O^\infty}{s Y_F^I + Y_O^\infty} \quad ; \quad s = \frac{\nu_O M_O}{\nu_F M_F} \tag{3.132}$$

Averaged over time, both the integral $\int_f \rho \mathbf{u}\cdot\mathbf{n}\, dS$ and the quantity $\dot{m}_f(t)$ will equal the mass flow of fuel from the burner $\dot{m}_b$, yielding

$$\dot{m}_b\,(1-Z_f) = \overline{-\int_f \rho D \nabla Z\cdot\mathbf{n}\, dS} \tag{3.133}$$

Using the identities

$$\left.\frac{dY_O}{dZ}\right|_{Z<Z_f} = -\frac{Y_O^\infty}{Z_f} = -(s Y_F^I + Y_O^\infty) \quad ; \quad 1-Z_f = \frac{s Y_F^I}{s Y_F^I + Y_O^\infty} \tag{3.134}$$

we arrive at

$$\dot{m}_b\, Y_F^I\, s\, \Delta H_O = \Delta H_O \left.\frac{dY_O}{dZ}\right|_{Z<Z_f} \overline{\int_f \rho D\, \nabla Z\cdot\mathbf{n}\, dS} \tag{3.135}$$

The quantity $\dot{m}_b\, Y_F^I$ is the mass flow of fuel (allowing for the possibility that the fuel is diluted), and $s\,\Delta H_O$ is the heat of combustion. This exercise confirms that if we integrate Eq. (3.130) over the flame sheet and time-average the result, we obtain the total heat release rate of the fire.

Suppose now we repeat the exercise with the finite difference form of the equations. Ultimately, we seek a discretization of Eq. (3.130) so that when we numerically integrate it over the flame sheet, we obtain the desired heat release rate. The flame sheet is now approximated by a stair-stepped surface formed by grid cell interfaces such that cells inside the surface have mixture fraction values greater than stoichiometric ($Z > Z_f$) and cells outside the surface have values that are less ($Z < Z_f$). Remember that the mixture fraction and all other scalar quantities are defined at cell centers. The mass flux of mixture fraction at the interface between cell ijk and cell $i+1, jk$ is written in conservative form (excluding the subscript jk to reduce clutter)

$$\dot{m}''_f = u_i\,(\rho Z)_{i+\frac{1}{2}} - (\rho D)_{i+\frac{1}{2}} \frac{Z_{i+1}-Z_i}{\delta x} \tag{3.136}$$

Note that the horizontal component of velocity u_i is defined at the interface between the cell i and cell $(i+1)$, and that the subscript $(i+\frac{1}{2})$ denotes the average of the values of a given quantity in cell i and $(i+1)$. It is important to remember that the value of the mixture fraction at the cell interface is close, but not exactly equal to, Z_f. To account for this, we rewrite the convective component of the mass flux as follows:

$$u_i\,(\rho Z)_{i+\frac{1}{2}} = u_i\,\rho_{i+\frac{1}{2}}\,Z_f + u_i\,\rho_{i+\frac{1}{2}}\,(\overline{Z}-Z_f) \quad ; \quad \overline{Z} = \frac{(\rho Z)_{i+\frac{1}{2}}}{\rho_{i+\frac{1}{2}}} = \frac{\rho_{i+1}Z_{i+1}+\rho_i Z_i}{\rho_{i+1}+\rho_i} \tag{3.137}$$

The term $u_i\,\rho_{i+\frac{1}{2}}\,Z_f$ when summed over the stair-stepped flame surface will equal exactly (via telescoping sums) Z_f multiplied by the mass flow through the surface. When averaged over time, the mass flow through the flame surface will be equal to the mass flow of fuel through the burner. This reasoning is completely analogous to that above which resulted in Eq. (3.133). The term $u_i\,\rho_{i+\frac{1}{2}}\,(\overline{Z}-Z_f)$ does not appear in the analytical derivation above. It represents the error associated with approximating the flame sheet at the interface between two grid cells. It must be accounted for in the finite difference approximation to Eq. (3.130):

$$\dot{q}'' = \Delta H_O \left.\frac{dY_O}{dZ}\right|_{Z<Z_f} \begin{cases} (\rho D)_{i+\frac{1}{2}}\,(Z_{i+1}-Z_i)/\delta x - u_i\,\rho_{i+\frac{1}{2}}\,(\overline{Z}-Z_f) & Z_i > Z_f > Z_{i+1} \\ (\rho D)_{i+\frac{1}{2}}\,(Z_i-Z_{i+1})/\delta x + u_i\,\rho_{i+\frac{1}{2}}\,(\overline{Z}-Z_f) & Z_i < Z_f < Z_{i+1} \end{cases} \tag{3.138}$$

The energy released at the cell interfaces that make up the approximate flame surface is divided between the two cells on either side of the interface.

Heat Release Rate (Finite-Rate Reaction)

In a DNS calculation (usually), a one-step, finite-rate reaction of a hydrocarbon fuel is assumed

$$\nu_{C_xH_y} C_x\mathrm{H}_y + \nu_{O_2} O_2 \longrightarrow \nu_{CO_2} CO_2 + \nu_{H_2O} \mathrm{H}_2O \tag{3.139}$$

The single step finite rate reaction model provides a chemical "switch" that can turn the idealized combustion process on or off without arbitrarily introducing rules governing combustible oxygen concentrations or ignition temperatures. In any cell where the reaction is "on," the chemical reaction time scale is much shorter than any convective or diffusive transport time scale. Thus, it makes sense to calculate the consequences of the reaction assuming all other processes are frozen in a state corresponding to the beginning of the time step. For each grid cell, at the start of a time step where $t = t^n$ and $Y^n_{C_xH_y,ijk} \equiv Y_F(t^n)$ and $Y^n_{O_2,ijk} \equiv Y_O(t^n)$, the following ODE is solved numerically with a 2nd order Runge-Kutta scheme

$$\frac{dY_F}{dt} = -\frac{B\rho^{a+b-1}_{ijk}}{M^b_O M^{a-1}_F} Y_F(t)^a Y_O(t)^b \, e^{-E/RT_{ijk}} \tag{3.140}$$

$$\frac{dY_O}{dt} = -\frac{\nu_O M_O}{\nu_F M_F} \frac{dY_F}{dt} \tag{3.141}$$

The temperature T_{ijk} and density ρ_{ijk} are fixed at their values at time t^n and the ODE is iterated from t^n to t^{n+1} in about 100 time steps. The pre-exponential factor B, the activation energy E, and the exponents a and b are input parameters. The average heat release rate over the entire time step is given by

$$\dot{q}'''^n_{ijk} = \Delta H \, \rho^n_{ijk} \frac{Y_F(t^n) - Y_F(t^{n+1})}{\delta t} \tag{3.142}$$

where $\delta t = t^{n+1} - t^n$. The species mass fractions are adjusted at this point in the calculation (before the convection and diffusion update)

$$Y^n_{l,ijk} = Y_l(t^n) - \frac{\nu_l M_l}{\nu_F M_F} (Y_F(t^n) - Y_F(t^{n+1})) \tag{3.143}$$

3.7.7 Thermal Radiation

The discretized RTE is derived by integrating equation (3.48) over the grid cell ijk and the control angle $\delta\Omega^l$

$$\int_{\Omega^l} \int_{V_{ijk}} \mathbf{s} \cdot \nabla I(\mathbf{x},\mathbf{s}) dV d\Omega = \int_{\Omega^l} \int_{V_{ijk}} \kappa(\mathbf{x}) \, [I_b(\mathbf{x}) - I(\mathbf{x},\mathbf{s})] \, dV d\Omega \tag{3.144}$$

The volume integral on the left hand side is replaced by a surface integral over the cell faces using the divergence theorem. Assuming that the radiation intensity $I(\mathbf{x},\mathbf{s})$ is constant on each of the cell faces, the surface integral can be approximated by a sum over the cell faces. Assuming further that $I(\mathbf{x},\mathbf{s})$ is constant within the volume V_{ijk} and over the angle $\delta\Omega^l$ we obtain

$$\sum_{m=1}^{6} A_m \, I^l_m \int_{\Omega^l} (\mathbf{s} \cdot \mathbf{n}_m) d\Omega = \kappa_{ijk} \left[I_{b,ijk} - I^l_{ijk} \right] V_{ijk} \, \delta\Omega^l \tag{3.145}$$

where

I^l_{ijk}	radiant intensity in direction l
I^l_m	radiant intensity at cell face m
$I_{b,ijk}$	radiant blackbody Intensity in cell

$\delta\Omega^l$	solid angle corresponding to direction l
V_{ijk}	volume of cell ijk
A_m	area of cell face m
$\mathbf{n}_m$	unit normal vector of the cell face m

It must be noticed, that while the intensity is assumed constant within the angle $\delta\Omega^l$, its direction covers the angle $\delta\Omega^l$ exactly.

In Cartesian coordinates[3], the normal vectors $\mathbf{n}_m$ are the base vectors of the coordinate system and the integrals over the solid angle do not depend on the physical coordinate, but the direction only. The intensities on the cell boundaries, I^l_m, are calculated using a first order upwind scheme. If the physical space is swept in the direction $\mathbf{s}^l$, the intensity I^l_{ijk} can be directly solved from an algebraic equation. This makes the numerical solution of the FVM very fast. Iterations are needed only to account for the reflective boundaries. However, this is seldom necessary in practice, because of the small time step set by the flow solver.

The spatial discretization for the RTE solver is the same as for the fluid solver. The coordinate system used to discretize the solid angle is shown in Figure 3.5. The discretization of the solid angle is done by

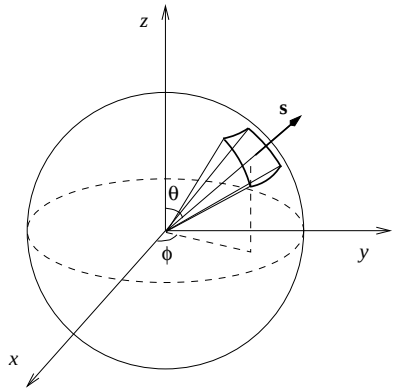

Figure 3.5: Coordinate system of the angular discretization.

dividing first the polar angle, θ, into N_θ bands, where N_θ is an even integer. Each θ-band is then divided into $N_\phi(\theta)$ parts in the azimuthal (ϕ) direction. $N_\phi(\theta)$ must be divisible by 4. The numbers N_θ and $N_\phi(\theta)$ are chosen to give the total number of angles N_Ω as close to the value defined by the user as possible. N_Ω is calculated as

$$N_\Omega = \sum_{i=1}^{N_\theta} N_\phi(\theta_i) \tag{3.146}$$

The distribution of the angles is based on empirical rules that try to produce equal solid angles $\delta\Omega^l = 4\pi/N_\Omega$. The number of θ-bands is

$$N_\theta = 1.17\, N_\Omega^{1/2.26} \tag{3.147}$$

rounded to the nearest even integer. The number of ϕ-angles on each band is

$$N_\phi(\theta) = \max\left\{4, 0.5 N_\Omega \left[\cos(\theta^-) - \cos(\theta^+)\right]\right\} \tag{3.148}$$

rounded to the nearest integer that is divisible by 4. θ^- and θ^+ are the lower and upper bounds of the θ-band, respectively. The discretization is symmetric with respect to the planes $x = 0$, $y = 0$, and $z = 0$.

[3]In the axisymmetric case equation (3.145) becomes a little bit more complicated, as the cell face normal vectors $\mathbf{n}_m$ are not always constant. However, the computational efficiency can still be retained.

This symmetry has three important benefits: First, it avoids the problems caused by the fact that first order upwind scheme, used to calculate intensities on the cell boundaries, is more diffusive in non-axial directions than axial. Second, the treatment of the mirror boundaries becomes very simple, as will be shown later. Third, it avoids so called "overhang" situations, where $\mathbf{s}\cdot\mathbf{i}$, $\mathbf{s}\cdot\mathbf{j}$ or $\mathbf{s}\cdot\mathbf{k}$ changes sign inside the control angle. These "overhangs" would make the resulting system of linear equations more complicated.

In the axially symmetric case these "overhangs" can not be avoided, and a special treatment, developed by Murthy and Mathur [62], is applied. In these cases $N_\phi(\theta_i)$ is kept constant, and the total number of angles is $N_\Omega = N_\theta \times N_\phi$. In addition, the angle of the vertical slice of the cylinder is chosen to be same as $\delta\phi$.

The cell face intensities, I^l_m appearing on the left hand side of (3.145) are calculated using a first order upwind scheme. Consider, for example, a control angle having a direction vector $\mathbf{s}$. If the radiation is traveling in the positive x-direction, *i.e.* $\mathbf{s}\cdot\mathbf{i} \geq 0$, the intensity on the upwind side, I^l_{xu} is assumed to be the intensity in the neighboring cell, $I^l_{i-1\,jk}$, and the intensity on the downwind side is the intensity in the cell itself I^l_{ijk}.

On a rectilinear grid, the normal vectors $\mathbf{n}_m$ are the base vectors of the coordinate system and the integrals over the solid angle can be calculated analytically. Equation (3.145) can be simplified

$$a^l_{ijk} I^l_{ijk} = a^l_x I^l_{xu} + a^l_y I^l_{yu} + a^l_z I^l_{zu} + b^l_{ijk} \tag{3.149}$$

where

$$a^l_{ijk} = A_x|D^l_x| + A_y|D^l_y| + A_z|D^l_z| + \kappa_{ijk}\, V_{ijk}\delta\Omega^l \tag{3.150}$$

$$a^l_x = A_x|D^l_x| \tag{3.151}$$

$$a^l_y = A_y|D^l_y| \tag{3.152}$$

$$a^l_z = A_z|D^l_z| \tag{3.153}$$

$$b^l_{ijk} = \kappa_{ijk}\, I_{b,ijk}\, V_{ijk}\, \delta\Omega^l \tag{3.154}$$

$$\delta\Omega^l = \int_{\Omega^l} d\Omega = \int_{\delta\phi}\int_{\delta\theta} \sin\theta\, d\theta\, d\phi \tag{3.155}$$

$$\begin{aligned} D^l_x &= \int_{\Omega^l} (\mathbf{s}^l\cdot\mathbf{i}) d\Omega \\ &= \int_{\delta\phi}\int_{\delta\theta} (\mathbf{s}^l\cdot\mathbf{i}) \sin\theta\, d\theta d\phi \\ &= \int_{\delta\phi}\int_{\delta\theta} \cos\phi\sin\theta\sin\theta\, d\theta d\phi \\ &= \frac{1}{2}\left(\sin\phi^+ - \sin\phi^-\right)\left[\Delta\theta - \left(\cos\theta^+\sin\theta^+ - \cos\theta^-\sin\theta^-\right)\right] \end{aligned} \tag{3.156}$$

$$\begin{aligned} D^l_y &= \int_{\Omega^l} (\mathbf{s}^l\cdot\mathbf{j}) d\Omega \\ &= \int_{\delta\phi}\int_{\delta\theta} \sin\phi\sin\theta\sin\theta\, d\theta d\phi \\ &= \frac{1}{2}\left(\cos\phi^- - \cos\phi^+\right)\left[\Delta\theta - \left(\cos\theta^+\sin\theta^+ - \cos\theta^-\sin\theta^-\right)\right] \end{aligned} \tag{3.157}$$

$$D^l_z = \int_{\Omega^l} (\mathbf{s}^l\cdot\mathbf{k}) d\Omega \tag{3.158}$$

$$= \int_{\delta\phi}\int_{\delta\theta} \cos\theta \sin\theta \, d\theta d\phi$$
$$= \frac{1}{2}\Delta\phi\left[\left(\sin\theta^{+}\right)^2 - \left(\sin\theta^{-}\right)^2\right]$$

Here **i**, **j** and **k** are the base vectors of the Cartesian coordinate system. θ^+, θ^-, ϕ^+ and ϕ^+ are the upper and lower boundaries of the control angle in the polar and azimuthal directions, respectively, and $\Delta\theta = \theta^+ - \theta^-$ and $\Delta\phi = \phi^+ - \phi^-$. The solution method of (3.149) is based on an explicit marching sequence [63]. The marching direction depends on the propagation direction of the radiation intensity. As the marching is done in the "downwind" direction, the "upwind" intensities in all three spatial directions are known, and the intensity I^l_{ijk} can be solved directly. Iterations may be needed only with the reflective walls and optically thick situations. Currently, no iterations are made.

The boundary condition on a solid wall is given as

$$I^l_w = \varepsilon \frac{\sigma T^4_w}{\pi} + \frac{1-\varepsilon}{\pi} \sum_{D^{l'}_w<0} I^{l'}_w \, |D^{l'}_w| \tag{3.159}$$

where $D^{l'}_w = \int_{\Omega^{l'}} (\mathbf{s}\cdot\mathbf{n}_w) d\Omega$. The constraint $D^{l'}_w < 0$ means that only the "incoming" directions are taken into account when calculating the reflection. The radiative heat flux on the wall is

$$q_w = \sum_{l=1}^{N_\Omega} I^l_w \int_{\delta\Omega^l} (\mathbf{s}\cdot\mathbf{n}_w) d\Omega = \sum_{l=1}^{N_\Omega} I^l_w D^l_n \tag{3.160}$$

where the coefficients D^l_n are equal to $\pm D^l_x$, $\pm D^l_y$ or $\pm D^l_z$, and can be calculated for each wall element beforehand.

The open boundaries are treated as black walls, where the incoming intensity is the black body intensity of the ambient temperature. On mirror boundaries the intensities leaving the wall are calculated from the incoming intensities using a predefined connection matrix.

$$I^l_{w,ijk} = I^{l'} \tag{3.161}$$

Computationally intensive integration over all the incoming directions is avoided by keeping the solid angle discretization symmetric x, y and z planes. The connection matrix associates one incoming direction l' to each mirrored direction on each wall cell.

The local incident radiation intensity is

$$U_{ijk} = \sum_{l=1}^{N_\Omega} I^l_{ijk} \delta\Omega^l \tag{3.162}$$

3.7.8 Interaction of Droplets and Radiation

The computation of χ_f for a similar but simpler situation has been derived in Ref. [64]. It can be shown that here χ_f becomes

$$\chi_f = \frac{1}{\delta\Omega^l} \int_0^{\mu^l} \int_0^{\mu^l} \int_{\mu_{d,0}}^{\mu_{d,\pi}} \frac{P_0(\theta_d)}{(1-\mu 2)(1-\mu'^2) - (\mu_d - \mu\mu')2} \, d\mu_d \, d\mu \, d\mu' \tag{3.163}$$

where μ_d is a cosine of the scattering angle θ_d and $P_0(\theta_d)$ is a single droplet scattering phase function

$$P_0(\theta_d) = \frac{\lambda^2 \left(|S_1(\theta_d)|^2 + |S_2(\theta_d)|^2\right)}{2 C_s(r,\lambda)} \tag{3.164}$$

$S_1(\theta_d)$ and $S_2(\theta_d)$ are the scattering amplitudes, given by Mie-theory. The integration limit μ^l is a cosine of the polar angle defining the boundary of the symmetric control angle $\delta\Omega^l$

$$\mu^l = \cos(\theta^l) = 1 - \frac{2}{N_\Omega} \tag{3.165}$$

The limits of the innermost integral are

$$\mu_{d,0} = \mu\mu' + \sqrt{1-\mu^2}\sqrt{1-\mu'^2} \quad ; \quad \mu_{d,\pi} = \mu\mu' - \sqrt{1-\mu^2}\sqrt{1-\mu'^2} \tag{3.166}$$

When χ_f is integrated over the droplet size distribution to get an averaged value, it is multiplied by $C_s(r,\lambda)$. It is therefore $|S_1|^2 + |S_2|^2$, not $P_0(\theta_d)$, that is integrated. Physically, this means that intensities are added, not probabilities [55].

3.7.9 Thermal and Material Boundary Conditions

Four types of thermal boundary conditions are applied at solid surfaces. The first, and simplest, is an adiabatic boundary condition that states that there is no temperature gradient normal to the surface. It is implemented by assigning to the grid cell that is embedded in the solid (the ghost cell) the same temperature as the first cell in the gas(the gas cell).

The second type of boundary condition is where the solid surface has a prescribed temperature (usually this prescribed temperature is a function of time).

The third type of boundary condition assumes the solid to be thermally-thin. The surface temperature is updated in time according to

$$T_w^{n+1} = T_w^n + \delta t_s \frac{\dot{q}_c'' + \dot{q}_r''}{\rho_s c_s \delta} \tag{3.167}$$

where T_w is the wall temperature, δt_s is the time step used when updating the thermal boundary conditions (usually greater than the hydrodynamic time step δt), and ρ_s, c_s, δ are the input density, specific heat and thickness of the wall. In a DNS calculation where the boundary layer is resolved, the convective flux to the wall is given by

$$\dot{q}_c'' = -k\frac{T_{gas} - T_w}{\delta n/2} \tag{3.168}$$

where δn is the size of a grid cell in the normal direction to the wall. In an LES calculation where the boundary layer is not resolved,

$$\dot{q}_c'' = C|T_{gas} - T_w|^{\frac{1}{3}}(T_{gas} - T_w) \quad \text{W/m}^2 \tag{3.169}$$

where C is an empirical coefficient (0.95 for vertical surface; 1.43 for horizontal), and T_{gas} is the temperature of the gas in the cell bordering the wall.

The fourth type of thermal boundary condition is for a thermally-thick solid. In this case, a one dimensional heat transfer calculation is performed at each boundary cell designated as thermally-thick. The width of the solid δ is partitioned into N cells, clustered near the front face. The cell boundaries are located at points x_i

$$x_i = f(\xi_i) = \delta\,\frac{e^{s\xi_i/\delta} - 1}{e^s - 1} \tag{3.170}$$

where $0 \le i \le N$, $\xi_i = i\,\delta\xi$, $\delta\xi = \delta/N$, and $0 < s \le 1$ is a measure of the degree of clustering of the cells at the front face. The width of each cell is $\delta x_i = f'(\xi_{i-\frac{1}{2}})\delta\xi$, $1 \le i \le N$ where $\xi_{i-\frac{1}{2}} = (i-\frac{1}{2})\,\delta\xi$. The temperature at the center of the ith cell is denoted $T_{s,i}$. The (temperature-dependent) thermal conductivity of the solid at the

center of the ith cell is denoted $k_{s,i}$. The temperatures are updated in time using an implicit Crank-Nicholson scheme

$$\frac{T_{s,i}^{n+1}-T_{s,i}^{n}}{\delta t}=\frac{1}{2(\rho_s c_s)_i \delta x_i}\qquad\left(k_{s,i+\frac{1}{2}}\frac{T_{s,i+1}^{n}-T_{s,i}^{n}}{\delta x_{s,i+\frac{1}{2}}}-k_{s,i-\frac{1}{2}}\frac{T_{s,i}^{n}-T_{s,i-1}^{n}}{\delta x_{s,i-\frac{1}{2}}}+\right.$$
$$\left.k_{s,i+\frac{1}{2}}\frac{T_{s,i+1}^{n+1}-T_{s,i}^{n+1}}{\delta x_{i+\frac{1}{2}}}-k_{s,i-\frac{1}{2}}\frac{T_{s,i}^{n+1}-T_{s,i-1}^{n+1}}{\delta x_{i-\frac{1}{2}}}\right) \tag{3.171}$$

for $1 \leq i \leq N$. The boundary condition is discretized

$$-k_{s,1}\frac{T_{s,1}^{n+1}-T_{s,0}^{n+1}}{\delta x_{\frac{1}{2}}}=\dot{q}_c''+\dot{q}_r''-4\,\varepsilon\,\sigma\,T_{s,\frac{1}{2}}^{n^3}\left(T_{s,\frac{1}{2}}^{n+1}-T_{s,\frac{1}{2}}^{n}\right) \tag{3.172}$$

where $T_{s,\frac{1}{2}}=(T_{s,1}+T_{s,0})/2$ is the temperature at the front face. Notice that the radiative emission term has been linearized

$$T_{s,\frac{1}{2}}^{(n+1)^4}-T_{s,\frac{1}{2}}^{n^4}\approx 4\,T_{s,\frac{1}{2}}^{n^3}\left(T_{s,\frac{1}{2}}^{n+1}-T_{s,\frac{1}{2}}^{n}\right) \tag{3.173}$$

The wall temperature is defined $T_w \equiv T_{s,\frac{1}{2}}=(T_{s,0}+T_{s,1})/2$.

Regardless of how the wall temperature is determined, there are two ways of coupling the wall temperature with the fluid calculation. Gas phase temperatures are defined at cell centers; the wall is defined at the boundary of the bordering gas phase cell and a "ghost" cell inside the wall. As far as the gas phase calculation is concerned, the normal temperature gradient at the wall is expressed in terms of the temperature difference between the "gas" cell and the "ghost" cell. The wall temperature affects the gas phase calculation through the prescription of the ghost cell temperature. This ghost cell temperature has no physical meaning on its own. Only the difference between ghost and gas cell temperatures matters, for this defines the heat transfer to the wall.

In a DNS calculation, the wall temperature is assumed to be an average of the ghost cell temperature and the temperature of the first cell in the gas, thus the ghost cell temperature is defined

$$T_{ghost}=2T_w-T_{gas} \tag{3.174}$$

For an LES calculation, the heat lost to the boundary is equated with an empirical expression

$$k\frac{T_{gas}-T_{ghost}}{\delta n}=C|T_{gas}-T_w|^{\frac{1}{3}}(T_{gas}-T_w) \tag{3.175}$$

where δn is the distance between the center of the ghost cell and the center of the gas cell. This equation is solved for T_{ghost}, so that when the conservation equations are updated, the amount of heat lost to the wall is equivalent to the empirical expression on the right hand side. Note that T_{ghost} is purely a numerical construct. It does not represent the temperature within the wall, but rather establishes a temperature gradient at the wall consistent with the empirical correlation.

At solid walls there is no transfer of mass, thus the boundary condition for the lth species at a wall is simply

$$Y_{l,ghost}=Y_{l,gas} \tag{3.176}$$

where the subscripts "ghost" and "gas" are the same as above since the mass fraction, like temperature, is defined at cell centers. At forced flow boundaries either the mass fraction $Y_{l,w}$ or the mass flux $\dot{m}_l''$ of species l may be prescribed. Then the ghost cell mass fraction can be derived because, as with temperature, the

normal gradient of mass fraction is needed in the gas phase calculation. For cases where the mass fraction is prescribed

$$Y_{l,ghost} = 2Y_{l,w} - Y_{l,gas} \tag{3.177}$$

For cases where the mass flux is prescribed, the following equation must be solved iteratively

$$\dot{m}_l'' = u_n \frac{\rho_{ghost} Y_{l,ghost} + \rho_{gas} Y_{l,gas}}{2} - \rho D \frac{Y_{l,gas} - Y_{l,ghost}}{\delta n} \mp \frac{\delta t\, u_n^2}{2} \frac{\rho_{gas} Y_{l,gas} - \rho_{ghost} Y_{l,ghost}}{\delta n} \tag{3.178}$$

where $\dot{m}_l''$ is the mass flux of species l per unit area, u_n is the normal component of velocity at the wall pointing into the flow domain, and δn is the distance between the center of the ghost cell and the center of the gas cell. Notice that the last term on the right hand side is subtracted at the predictor step and added at the corrector step, consistent with the biased unwinding introduced earlier.

Once the temperature and species mass fractions have been defined in the ghost cell, the density in the ghost cell is computed from the equation of state

$$\rho_{ghost} = \frac{p_0}{\mathcal{R}\, T_{ghost} \sum_l (Y_{l,ghost}/M_l)} \tag{3.179}$$

3.7.10 The Momentum Equation

The three components of the momentum equation are

$$\frac{\partial u}{\partial t} + F_x + \frac{\partial \mathcal{H}}{\partial x} = 0 \quad ; \quad F_x = w\,\omega_y - v\,\omega_z - \frac{1}{\rho}\left(f_x + \frac{\partial \tau_{xx}}{\partial x} + \frac{\partial \tau_{xy}}{\partial y} + \frac{\partial \tau_{xz}}{\partial z} \right) \tag{3.180}$$

$$\frac{\partial v}{\partial t} + F_y + \frac{\partial \mathcal{H}}{\partial y} = 0 \quad ; \quad F_y = u\,\omega_z - w\,\omega_x - \frac{1}{\rho}\left(f_y + \frac{\partial \tau_{yx}}{\partial x} + \frac{\partial \tau_{yy}}{\partial y} + \frac{\partial \tau_{yz}}{\partial z} \right) \tag{3.181}$$

$$\frac{\partial w}{\partial t} + F_z + \frac{\partial \mathcal{H}}{\partial z} = 0 \quad ; \quad F_z = v\,\omega_x - u\,\omega_y - \frac{1}{\rho}\left(f_z + \frac{\partial \tau_{zx}}{\partial x} + \frac{\partial \tau_{zy}}{\partial y} + \frac{\partial \tau_{zz}}{\partial z} \right) \tag{3.182}$$

The spatial discretization of the momentum equations take the form

$$\frac{\partial u}{\partial t} + F_{x,ijk} + \frac{\mathcal{H}_{i+1,jk} - \mathcal{H}_{ijk}}{\delta x} = 0 \tag{3.183}$$

$$\frac{\partial v}{\partial t} + F_{y,ijk} + \frac{\mathcal{H}_{i,j+1,k} - \mathcal{H}_{ijk}}{\delta y} = 0 \tag{3.184}$$

$$\frac{\partial w}{\partial t} + F_{z,ijk} + \frac{\mathcal{H}_{ij,k+1} - \mathcal{H}_{ijk}}{\delta z} = 0 \tag{3.185}$$

where $\mathcal{H}_{ijk}$ is taken at center of cell ijk, u_{ijk} and $F_{x,ijk}$ are taken at the side of the cell facing in the forward x direction, v_{ijk} and $F_{y,ijk}$ at the side facing in the forward y direction, and w_{ijk} and $F_{z,ijk}$ at the side facing in the forward z (vertical) direction. In the definitions to follow, the components of the vorticity $(\omega_x, \omega_y, \omega_z)$ are located at cell edges pointing in the x, y and z directions, respectively. The same is true for the off-diagonal terms of the viscous stress tensor: $\tau_{zy} = \tau_{yz}$, $\tau_{xz} = \tau_{zx}$, and $\tau_{xy} = \tau_{yx}$. The diagonal components of the stress tensor τ_{xx}, τ_{xx}, and τ_{xx}; the external force components (f_x, f_y, f_z); and the unwinding bias terms ε_u, ε_v, and ε_w are located at the respective cell faces.

$$\begin{aligned} F_{x,ijk} \;=\; & \left(\frac{1 \mp \varepsilon_w}{2} w_{i+\frac{1}{2},jk}\, \omega_{y,ijk} + \frac{1 \pm \varepsilon_w}{2} w_{i+\frac{1}{2},j,k-1}\, \omega_{y,ij,k-1} \right) \\ & - \left(\frac{1 \mp \varepsilon_v}{2} v_{i+\frac{1}{2},jk}\, \omega_{z,ijk} + \frac{1 \pm \varepsilon_v}{2} v_{i+\frac{1}{2},j-1,k}\, \omega_{z,i,j-1,k} \right) \end{aligned}$$

$$-\frac{1}{\rho_{i+\frac{1}{2},jk}}\left(f_{x,ijk}+\frac{\tau_{xx,i+1,jk}-\tau_{xx,ijk}}{\delta x}+\frac{\tau_{xy,ijk}-\tau_{xy,i,j-1,k}}{\delta y}+\frac{\tau_{xz,ijk}-\tau_{xz,i,j,k-1}}{\delta z}\right) \tag{3.186}$$

$$\begin{aligned} F_{y,ijk} &= \left(\frac{1\mp\varepsilon_u}{2}u_{i,j+\frac{1}{2},k}\,\omega_{z,ijk}+\frac{1\pm\varepsilon_u}{2}u_{i-1,j+\frac{1}{2},k}\,\omega_{z,i-1,jk}\right) \\ &\quad -\left(\frac{1\mp\varepsilon_w}{2}w_{i,j+\frac{1}{2},k}\,\omega_{x,ijk}+\frac{1\pm\varepsilon_w}{2}w_{i,j+\frac{1}{2},k-1}\,\omega_{x,ij,k-1}\right) \\ &\quad -\frac{1}{\rho_{i,j+\frac{1}{2},k}}\left(f_{y,ijk}+\frac{\tau_{yx,ijk}-\tau_{yx,i-1,jk}}{\delta x}+\frac{\tau_{yy,i,j+1,k}-\tau_{yy,ijk}}{\delta y}+\frac{\tau_{yz,ijk}-\tau_{yz,i,j,k-1}}{\delta z}\right) \end{aligned} \tag{3.187}$$

$$\begin{aligned} F_{z,ijk} &= \left(\frac{1\mp\varepsilon_v}{2}v_{ij,k+\frac{1}{2}}\,\omega_{x,ijk}+\frac{1\pm\varepsilon_v}{2}v_{i,j-1,k+\frac{1}{2}}\,\omega_{x,i,j-1,k}\right) \\ &\quad -\left(\frac{1\mp\varepsilon_u}{2}u_{ij,k+\frac{1}{2}}\,\omega_{y,ijk}+\frac{1\pm\varepsilon_u}{2}u_{i-1,j,k+\frac{1}{2}}\,\omega_{y,i-1,jk}\right) \\ &\quad -\frac{1}{\rho_{ij,k+\frac{1}{2}}}\left(f_{z,ijk}+\frac{\tau_{zx,ijk}-\tau_{zx,i-1,jk}}{\delta x}+\frac{\tau_{zy,ijk}-\tau_{zy,i,j-1,k}}{\delta y}+\frac{\tau_{zz,ij,k+1}-\tau_{zz,ijk}}{\delta z}\right) \end{aligned} \tag{3.188}$$

$$\omega_{x,ijk} = \frac{w_{i,j+1,k}-w_{ijk}}{\delta y}-\frac{v_{ij,k+1}-v_{ijk}}{\delta z} \tag{3.189}$$

$$\omega_{y,ijk} = \frac{u_{ij,k+1}-u_{ijk}}{\delta z}-\frac{w_{i+1,jk}-w_{ijk}}{\delta x} \tag{3.190}$$

$$\omega_{z,ijk} = \frac{v_{i+1,jk}-v_{ijk}}{\delta x}-\frac{u_{i,j+1,k}-u_{ijk}}{\delta y} \tag{3.191}$$

$$\tau_{xx,ijk} = \mu_{ijk}\left(2\frac{u_{ijk}-u_{i-1,jk}}{\delta x}-\frac{2}{3}(\nabla\cdot\mathbf{u})_{ijk}\right)\equiv\mu_{ijk}\left(\frac{4}{3}(\nabla\cdot\mathbf{u})_{ijk}-2\frac{v_{ijk}-v_{i,j-1,k}}{\delta y}-2\frac{w_{ijk}-w_{ij,k-1}}{\delta z}\right) \tag{3.192}$$

$$\tau_{yy,ijk} = \mu_{ijk}\left(2\frac{v_{ijk}-v_{i,j-1,k}}{\delta y}-\frac{2}{3}(\nabla\cdot\mathbf{u})_{ijk}\right)\equiv\mu_{ijk}\left(\frac{4}{3}(\nabla\cdot\mathbf{u})_{ijk}-2\frac{u_{ijk}-u_{i-1,jk}}{\delta x}-2\frac{w_{ijk}-w_{ij,k-1}}{\delta z}\right) \tag{3.193}$$

$$\tau_{zz,ijk} = \mu_{ijk}\left(2\frac{w_{ijk}-w_{ij,k-1}}{\delta z}-\frac{2}{3}(\nabla\cdot\mathbf{u})_{ijk}\right)\equiv\mu_{ijk}\left(\frac{4}{3}(\nabla\cdot\mathbf{u})_{ijk}-2\frac{u_{ijk}-u_{i-1,jk}}{\delta x}-2\frac{v_{ijk}-v_{ij-1,k}}{\delta y}\right) \tag{3.194}$$

$$\tau_{xy,ijk} = \tau_{yx,ijk}=\mu_{i+\frac{1}{2},j+\frac{1}{2},k}\left(\frac{u_{i,j+1,k}-u_{ijk}}{\delta y}+\frac{v_{i+1,jk}-v_{ijk}}{\delta x}\right) \tag{3.195}$$

$$\tau_{xz,ijk} = \tau_{zx,ijk}=\mu_{i+\frac{1}{2},j,k+\frac{1}{2}}\left(\frac{u_{ij,k+1}-u_{ijk}}{\delta z}+\frac{w_{i+1,jk}-w_{ijk}}{\delta x}\right) \tag{3.196}$$

$$\tau_{yz,ijk} = \tau_{zy,ijk}=\mu_{i,j+\frac{1}{2},k+\frac{1}{2}}\left(\frac{v_{ij,k+1}-v_{ijk}}{\delta z}+\frac{w_{i,j+1,k}-w_{ijk}}{\delta y}\right) \tag{3.197}$$

$$\varepsilon_u = \frac{u\,\delta t}{\delta x} \tag{3.198}$$

$$\varepsilon_v = \frac{v\,\delta t}{\delta y} \tag{3.199}$$

$$\varepsilon_w = \frac{w\,\delta t}{\delta z} \tag{3.200}$$

The variables ε_u, ε_v and ε_w are local Courant numbers evaluated at the same locations as the velocity component immediately following them, and serve to bias the differencing of the convective terms in the upwind direction. The subscript $i+\frac{1}{2}$ indicates that a variable is an average of its values at the ith and the $(i+1)$th cell. The divergence defined in Eq. (3.124) is identically equal to the divergence defined by

$$(\nabla\cdot\mathbf{u})_{ijk}=\frac{u_{ijk}-u_{i-1,jk}}{\delta x}+\frac{v_{ijk}-v_{i,j-1,k}}{\delta y}+\frac{w_{ijk}-w_{ij,k-1}}{\delta z} \tag{3.201}$$

The equivalence of the two definitions of the divergence is a result of the form of the discretized equations, the time-stepping scheme, and the direct solution of the Poisson equation for the pressure.

Force Terms

The external force term components, in addition to including the effects of buoyancy, may also include the drag force from sprinkler droplets.

$$f_{x,ijk} = \frac{1}{2}\frac{\sum \rho C_D \pi r_d^2 (u_d - u_{ijk})|\mathbf{u}_d - \mathbf{u}|}{\delta x \delta y \delta z} - (\rho_{i+\frac{1}{2},jk} - \rho_\infty) g_x \tag{3.202}$$

$$f_{y,ijk} = \frac{1}{2}\frac{\sum \rho C_D \pi r_d^2 (v_d - v_{ijk})|\mathbf{u}_d - \mathbf{u}|}{\delta x \delta y \delta z} - (\rho_{i,j+\frac{1}{2},k} - \rho_\infty) g_y \tag{3.203}$$

$$f_{z,ijk} = \frac{1}{2}\frac{\sum \rho C_D \pi r_d^2 (w_d - w_{ijk})|\mathbf{u}_d - \mathbf{u}|}{\delta x \delta y \delta z} - (\rho_{ij,k+\frac{1}{2}} - \rho_\infty) g_z \tag{3.204}$$

where $\mathbf{g} = (g_x, g_y, g_z)$ is the gravity vector, r_d is the radius of a droplet, $\mathbf{u} = (u_d, v_d, w_d)$ the velocity of a droplet, C_D the drag coefficient, and $\delta x \delta y \delta z$ the volume of the ijkth cell. The summations represent all droplets within a grid cell centered about the x, y and z faces of a grid cell respectively.

Time Step

The time step is constrained by the convective and diffusive transport speeds via two conditions. The first is known as the Courant-Friedrichs-Lewy (CFL) condition:

$$\delta t \max\left(\frac{|u_{ijk}|}{\delta x}, \frac{|v_{ijk}|}{\delta y}, \frac{|w_{ijk}|}{\delta z}\right) < 1 \tag{3.205}$$

The estimated velocities $u^{(n+1)_e}$, $v^{(n+1)_e}$ and $w^{(n+1)_e}$ are tested at each time step to ensure that the CFL condition is satisfied. If it is not, then the time step is set to 0.8 of its allowed maximum value and the estimated velocities are recomputed (and checked again). The CFL condition asserts that the solution of the equations cannot be updated with a time step larger than that allowing a parcel of fluid to cross a grid cell. For most large-scale calculations where convective transport dominates diffusive, the CFL condition is most important.

However, in small, finely-gridded domains, a second condition often dominates:

$$2 \max\left(\nu, D, \frac{k}{\rho c_p}\right) \delta t \left(\frac{1}{\delta x^2} + \frac{1}{dy^2} + \frac{1}{\delta z^2}\right) < 1 \tag{3.206}$$

Note that this constraint applied to the momentum, mass and energy equations via the relevant diffusion parameter – viscosity, material diffusivity or thermal conductivity. This constraint on the time step, often referred to as the Von Neumann criterion, is typical of any explicit, second-order numerical scheme for solving a parabolic partial differential equation. The Von Neumann criterion is only invoked for DNS calculations or for LES calculations with grid cells smaller than 5 mm.

3.7.11 The Pressure Equation

The divergence of the momentum equation yields a Poisson equation for the pressure

$$\frac{\mathcal{H}_{i+1,jk} - 2\mathcal{H}_{ijk} + \mathcal{H}_{i-1,jk}}{\delta x^2} + \frac{\mathcal{H}_{i,j+1,k} - 2\mathcal{H}_{ijk} + \mathcal{H}_{i,j-1,k}}{\delta y^2} + \frac{\mathcal{H}_{ij,k+1} - 2\mathcal{H}_{ijk} + \mathcal{H}_{ij,k-1}}{\delta z^2}$$
$$= -\frac{F_{x,ijk} - F_{x,i-1,jk}}{\delta x} - \frac{F_{y,ijk} - F_{y,i,j-1,k}}{\delta y} - \frac{F_{z,ijk} - F_{z,ij,k-1}}{\delta z} - \frac{\partial}{\partial t}(\nabla \cdot \mathbf{u})_{ijk} \tag{3.207}$$

The lack of a superscript implies that all quantities are to be evaluated at the same time level. This elliptic partial differential equation is solved using a direct (non-iterative) FFT-based solver that is part of a library of routines for solving elliptic PDEs called CRAYFISHPAK [65]. To ensure that the divergence of the fluid is consistent with the definition given in Eq. (3.8), the time derivative of the divergence is defined

$$\frac{\partial}{\partial t}(\nabla\cdot\mathbf{u})_{ijk}=\frac{(\nabla\cdot\mathbf{u})_{ijk}^{(n+1)_e}-(\nabla\cdot\mathbf{u})_{ijk}^{n}}{\delta t} \tag{3.208}$$

at the predictor step, and then

$$\frac{\partial}{\partial t}(\nabla\cdot\mathbf{u})_{ijk}=\frac{2(\nabla\cdot\mathbf{u})_{ijk}^{n+1}-(\nabla\cdot\mathbf{u})_{ijk}^{(n+1)_e}-(\nabla\cdot\mathbf{u})_{ijk}^{n}}{\delta t} \tag{3.209}$$

at the corrector step. The discretization of the divergence was given in Eq. (3.124).

Direct Poisson solvers are most efficient if the domain is a rectangular region, although other geometries such as cylinders and spheres can be handled almost as easily. For these solvers, the no-flux condition (3.210) is simple to prescribe at external boundaries. For example, at the floor, $z=0$, the Poisson solver is supplied with the Neumann boundary condition

$$\frac{\mathcal{H}_{ij,1}-\mathcal{H}_{ij,0}}{\delta z}=-F_{z,ij,0} \tag{3.210}$$

However, many practical problems involve more complicated geometries. For building fires, doors and windows within multi-room enclosures are very important features of the simulations. These elements may be included in the overall domain as masked grid cells, but the no-flux condition (3.210) cannot be directly prescribed at the boundaries of these blocked cells. Fortunately, it is possible to exploit the relatively small changes in the pressure from one time step to the next to enforce the no-flux condition. At the start of a time step, the components of the convection/diffusion term **F** are computed at all cell faces that do not correspond to walls. At those cell faces that do correspond to solid walls, prescribe

$$F_n=-\frac{\partial\mathcal{H}^*}{\partial n}+\frac{u_n}{\delta t} \tag{3.211}$$

where F_n is the normal component of **F** at the wall.

The asterisk indicates the most recent value of the pressure. Obviously, the pressure at this particular time step is not known until the Poisson equation is solved. Equation (3.211) asserts that following the solution of the Poisson equation for the pressure, the normal component of velocity u_n will be driven nearly (but not exactly) to zero. This is approximate because the true value of the velocity time derivative depends on the solution of the pressure equation, but since the most recent estimate of pressure is used, the approximation is very good. Also, even though there are small errors in normal velocity at solid surfaces, the divergence of each blocked cell remains exactly zero for the duration of the calculation. In other words, the total flux into a given obstruction is always identically zero, and the error in normal velocity is usually at least several orders of magnitude smaller than the characteristic flow velocity. When implemented as part of a predictor-corrector updating scheme, the no-flux condition at solid surfaces is maintained remarkably well.

At open boundaries (say $i=I$), $\mathcal{H}$ is prescribed depending on whether the flow is incoming or outgoing

$$\begin{array}{ll}\mathcal{H}_{I+\frac{1}{2},jk}=(u_{I,jk}^2+v_{I,j-\frac{1}{2},k}^2+w_{I,j-\frac{1}{2},k}^2)/2 & u_{I,jk}>0\\ \mathcal{H}_{I+\frac{1}{2},jk}=0 & u_{I,jk}<0\end{array} \tag{3.212}$$

where I is the index of the last gas phase cell in the x direction and $u_{I,jk}$ is the x component of velocity at the boundary. The value of H in the ghost cell is

$$\mathcal{H}_{I+1,jk}=2\mathcal{H}_{I+\frac{1}{2},jk}-\mathcal{H}_{I,jk} \tag{3.213}$$

3.7.12 Particle Tracking

Thermal elements are introduced into the flow field as a means of introducing heat and as a way to visualize the flow. The position $\mathbf{x}_p$ of each thermal element is governed by the equations

$$\frac{d\mathbf{x}_p}{dt} = \mathbf{u} \tag{3.214}$$

The thermal element positions are updated according to the same predictor-corrector scheme that is applied to the other flow quantities. Briefly, the position $\mathbf{x}_p$ of a given thermal element is updated according to the two step scheme

$$\mathbf{x}_p^{(n+1)_e} = \mathbf{x}_p^n + \delta t\, \overline{\mathbf{u}}^n \tag{3.215}$$

$$\mathbf{x}_p^{n+1} = \frac{1}{2}\left(\mathbf{x}_p^n + \mathbf{x}_p^{(n+1)_e} + \delta t\, \overline{\mathbf{u}}^{(n+1)_e}\right) \tag{3.216}$$

where the bar over the velocity vector indicates that the velocity of the fluid is interpolated at the element's position.

3.8 Review of the Theoretical Development of the Model

ASTM E 1355 [3] requires that the theoretical basis of the model be reviewed by one or more recognized experts fully conversant with the chemistry and physics of fire phenomenon, but not involved with the production of the model. FDS is reviewed in two ways, internally and externally. All documents issued by the National Institute of Standards and Technology are formally reviewed internally by members of the staff. The theoretical basis of FDS is laid out in the present document, and is subject to internal review by staff members who are not active participants in the development of the model, but who are members of the Fire Research Division and are considered experts in the fields of fire and combustion. Externally, papers detailing various parts of FDS are regularly published in peer-reviewed journals and conference proceedings. In addition, FDS is used world-wide by fire protection engineering firms who review the technical details of the model related to their particular application. Some of these firms also publish in the open literature reports documenting internal efforts to validate the model for a particular use. Many of these studies are referenced in the present document.

3.8.1 Assessment of the Completeness of Documentation

As discussed in Section 2.1.4, there are three relevant documents associated with FDS: the Technical Reference Guide, the FDS User's Guide [11], and the Smokeview User's Guide [12]. The Technical Reference Guide provides a description of the equations, assumptions, and approximations of the various sub-models. The User's Guide provides instruction on how to actually run the model, plus a description of the physical and numerical parameters.

The quality of the FDS and Smokeview User's Guides is checked implicitly by the fact that the majority of model users have not taken a formal training course in the actual use of the model, but are able to read the supporting documents, perform a few sample simulations, and then systematically build up a level of expertise appropriate for their applications. The developers receive daily feedback from users on the clarity of the documentation and add clarifications when needed. Before new versions of the model are released, there is a several month "beta test" period in which users test the new version using the updated documentation. This process is similar, although less formal, to that which most computer software programs undergo.

The FDS Technical Reference Guide contains a description of the governing equations and how these are solved numerically. However, it does not contain a detailed description of the derivation of the equations or the numerical techniques. For example, the basic conservation equations are solved numerically using Large Eddy Simulation (LES), a technique common to the CFD community. The documentation of FDS does not provide a detailed description of this technique, but rather makes appropriate references to supporting papers and reports.

3.8.2 Assessment of Justification of Approaches and Assumptions

The technical approach and assumptions of the model have been presented in the peer-reviewed scientific literature and at technical conferences. Also, all documents released by NIST are required to go through an internal editorial review and approval process. This process is designed to ensure compliance with the technical requirements, policy, and editorial quality required by NIST. The technical review includes a critical evaluation of the technical content and methodology, statistical treatment of data, uncertainty analysis, use of appropriate reference data and units, and bibliographic references. The FDS and Smokeview manuals are first reviewed by a member of the Fire Research Division, then by the immediate supervisor of the author of the document, then by the chief of the Fire Research Division, and finally by a reader from outside the division. Both the immediate supervisor and the division chief are technical experts in the field. Once the document has been reviewed, it is then brought before the Editorial Review Board (ERB), a body of repre-

sentatives from all the NIST laboratories. At least one reader is designated by the Board for each document that it accepts for review. This last reader is selected based on technical competence and impartiality. The reader is usually from outside the division producing the document and is responsible for checking that the document conforms with NIST policy on units, uncertainty and scope. He/she does not need to be a technical expert in fire or combustion.

Besides formal internal and peer review, FDS is subjected to continuous scrutiny because it is available free of charge to the general public and is used internationally by those involved in fire safety design and post-fire reconstruction. The source code for FDS is also released publicly, and has been used at various universities world-wide, both in the classroom as a teaching tool as well as for research. As a result, flaws in the theoretical development and the computer program itself have been identified and fixed. As FDS continues to evolve, the user base will continue to serve as a means to evaluate the model, as important to its development as the formal internal and external peer-review processes.

3.8.3 Assessment of Constants and Default Values

A comprehensive assessment of the numerical and physical parameters used in FDS is not available in one document. Instead, specific parameters have been exercised in various verification and validation studies performed at NIST and elsewhere. Numerical parameters are described in the Technical Reference Guide and are subject to the internal review process at NIST, but many physical parameters are extracted from the literature and do not undergo a formal review. The model user is expected to assess the appropriateness of default values provided by FDS and make changes to the default values if need be.

Chapter 4

Mathematical and Numerical Robustness

4.1 Introduction

ASTM E 1355 [3] outlines methods to evaluate the mathematical and numerical robustness of deterministic fire models. This process, often referred to as *model verification*, ensures the accuracy of the numerical solution of the governing equations. The methods include comparison with analytical solutions, code checking, and numerical tests.

4.2 Comparison with Analytical Solutions

Most complex combustion processes, including fire, are turbulent and time-dependant. There are no closed-form mathematical solutions for the fully-turbulent, time-dependant Navier-Stokes equations. CFD provides an approximate solution for the non-linear partial differential equations by replacing them with discretized algebraic equations that can be solved using a powerful computer. While there is no general analytical solution for fully-turbulent flows, certain sub-models address phenomenon that do have analytical solutions, for example, one-dimensional heat conduction through a solid. These analytical solutions can be used to test sub-models within a complex code such as FDS. The developers of FDS routinely use such practices to verify the correctness of the coding of the model [66, 67, 68]. Such verification efforts are relatively simple and routine and the results may not always be published nor included in the documentation.

Early in its development, the hydrodynamic solver that evolved to form the core of FDS was checked against analytical solutions of simplified fluid flow phenomena. These studies were conducted at the National Bureau of Standards (NBS)[1] by Rehm, Baum and co-workers [69, 70, 71]. The emphasis of this early work was to test the stability and consistency of the basic hydrodynamic solver, especially the velocity-pressure coupling that is vitally important in low Mach number applications. Many numerical algorithms developed up to that point in time were intended for use in high-speed flow applications, like aerospace. Many of the techniques adopted by FDS were originally developed for meteorogical models, and as such needed to be tested to assess whether they would be appropriate to describe relatively low-speed flow within enclosures.

A fundamental decision made by Rehm and Baum early in the FDS development was to use a direct (rather than iterative) solver for the pressure. In the low Mach number formulation of the Navier-Stokes equations, an elliptic partial differential equation for the pressure emerges, often referred to as the Poisson equation. Most CFD methods use iterative techniques to solve the governing conservation equations to avoid the necessity of directly solving the Poisson equation. The reason for this is that the equation is time-

[1] The National Institute of Standards and Technology (NIST) was formerly known as the National Bureau of Standards.

consuming to solve numerically on anything but a rectilinear grid. Because FDS is designed specifically for rectilinear grids, it can exploit fast, direct solvers of the Poisson equation, obtaining the pressure field with one pass through the solver to machine accuracy. FDS employs double-precision (8 byte) arithmetic, meaning that the relative difference between the computed and the exact solution of the discretized Poisson equation is on the order of 10^{-12}. The fidelity of the numerical solution of the entire system of equations is tied to the pressure/velocity coupling because often simulations can involve hundreds of thousands of time steps, with each time step consisting of two solutions of the Poisson equation to preserve second-order accuracy. Without the use of the direct Poisson solver, build-up of numerical error over the course of a simulation could produce spurious results. Indeed, an attempt to use single-precision (4 byte) arithmetic to conserve machine memory led to spurious results simply because the error per time step built up to an intolerable level.

4.3 Code Checking

An examination of the structure of the computer program can be used to detect potential errors in the numerical solution of the governing equations. The coding can be verified by a third party either manually or automatically with profiling programs to detect irregularities and inconsistencies [3].

At NIST, FDS has been compiled and run on computers manufactured by IBM, Hewlett-Packard, Sun Microsystems, Digital Equipment Corporation, Apple, Silicon Graphics, Dell, Compaq, and various other personal computer vendors. The operating systems on these platforms include Unix, Linux, Microsoft Windows, and Mac OSX. Compilers used include Lahey Fortran, Digital Visual Fortran, Intel Fortran, IBM XL Fortran, HPUX Fortran, Forte Fortran for SunOS, the Portland Group Fortran, and several others. Each combination of hardware, operating system and compiler involves a slightly different set of compiler and run-time options and a rigorous evaluation of the source code to test its compliance with the Fortran 90 ISO/ANSI standard [72]. Through this process, out-dated and potentially harmful code is updated or eliminated, and often the code is streamlined to improve its optimization on the various machines.

In addition, the source code for FDS is publicly released. Although it consists of on the order of 10,000 lines of Fortran statements, various researchers outside of NIST have been able to work with it and add enhancements needed for very specific applications or for research purposes. The source code is organized into 14 separate files, each containing subroutines related to a particular feature of the model, like the mass, momentum, and energy conservation equations, sprinkler activation and sprays, the pressure solver, *etc*. The lengthiest routines are devoted to input, output and initialization. Most of those working with the source code do not concern themselves with these lengthy routines but rather focus on the finite-difference algorithm contained in a few of the more important files. These external researchers provide feedback on the organization of the code and its internal documentation, that is, comments within the source code itself. Plus, they must compile the code on their own computers, adding to its portability.

4.4 Numerical Tests

Numerical techniques used to solve the governing equations within a model can be a source of error in the predicted results. The hydrodynamic model within FDS is second-order accurate in space and time. This means that the error terms associated with the approximation of the spatial partial derivatives by finite differences is of the order of the square of the grid cell size, and likewise the error in the approximation of the temporal derivatives is of the order of the square of the time step. As the numerical grid is refined, the "discretization error" decreases, and a more faithful rendering of the flow field emerges. The issue of grid sensitivity is extremely important to the proper use of the model and will be taken up in the next chapter.

A common technique of testing flow solvers is to systematically refine the numerical grid until the computed solution does not change, at which point the calculation is referred to as a Direct Numerical Solution (DNS) of the governing equations. For most practical fire scenarios, DNS is not possible on conventional computers. However, FDS does have the option of running in DNS mode, where the Navier-Stokes equations are solved without the use of sub-grid scale turbulence models of any kind. Because the basic numerical method is the same for LES and DNS, DNS calculations are a very effective way to test the basic solver, especially in cases where the solution is steady-state. Throughout its development, FDS has been used in DNS mode for special applications. For example, FDS has been used at a grid resolution of roughly 1 mm to look at flames spreading over paper in a microgravity environment [73, 74, 75]. Simulations have been compared to experiments performed aboard the US Space Shuttle. The flames are laminar and relatively simple in structure, and the comparisons are a qualitative assessment of the model solution. Similar studies have been performed comparing DNS simulations of a simple burner flame to laboratory experiments [76, 77]. Another study compared FDS simulations of a counterflow diffusion flames to experimental measurements and the results of a one-dimensional multi-step kinetics model [78].

Early work with the hydrodynamic solver compared two-dimensional simulations of gravity currents with salt-water experiments [58]. In these tests, the numerical grid was systematically refined until almost perfect agreement with experiment was obtained. Such convergence would not be possible if there were a fundamental flaw in the hydrodynamic solver.

Chapter 5

Model Sensitivity

5.1 Introduction

A sensitivity analysis considers the extent to which uncertainty in model inputs influences model output. Model parameters can be the physical properties of solids and gases, boundary conditions, initial conditions, *etc.* The parameters can also be purely numerical, like the size of the numerical grid. Conducting a sensitivity analysis is not a simple task, and it will differ depending on the application. FDS typically requires the user to provide several dozen input parameters that describe the geometry, materials, combustion phenomena, *etc.* It is usually not possible to extensively assess the influence of each on the solution. Plus, FDS by design does not limit the range of most of the input parameters because applications often push beyond the range for which the model has been validated. FDS is still used for research at NIST and elsewhere, and the developers do not presume to know in all cases what the acceptable range of any parameter is. The user is warned that he/she is responsible for the prescription of all parameters. The FDS manuals can only provide guidance.

The most important physical parameter in FDS, or indeed any fire model, is the heat release rate (HRR). Validation studies (Chapter 6) have shown that FDS predicts well the transport of heat and smoke when the HRR is known. It can be said that the model output is sensitive to the prescribed HRR, but no more so than an actual experiment would be. The same can be said of other physical parameters. For this reason, the influence of physical parameters will be assessed in Chapter 6. In this chapter, the effect of numerical parameters on the output will be examined.

5.2 Grid Sensitivity

The most important decision made by a model user is the size of the numerical grid. In general, the finer the numerical grid, the better the numerical solution of the equations. FDS is second-order accurate in space and time, meaning that halving the grid cell size will decrease the discretization error in the governing equations by a factor of 4. Because of the non-linearity of the equations, the decrease in discretization error does not necessarily translate into a comparable decrease in the error of a given FDS output quantity. To find out what effect a finer grid has on the solution, model users usually perform some form of grid sensitivity study in which the numerical grid is systematically refined until the output quantities do not change appreciably with each refinement. Of course, with each halving of the grid cell size, the time required for the simulation increases by a factor of $2^4 = 16$ (a factor of two for each spatial coordinate, plus time). In the end, a comprimise is struck between model accuracy and computer capacity.

Some grid sensitivity studies have been documented and published. Since FDS was first publicly released in 2000, significant changes in the combustion and radiation routines have been incorporated into the

Table 5.1: Grid Sizes for Computational Domain used in Ref. [80]

Cases	Grid Size (m)
Case 1	0.20 x 0.20 x 0.20
Case 2	0.14 x 0.14 x 0.14
Case 3	0.10 x 0.10 x 0.10
Case 4	0.08 x 0.08 x 0.08

Table 5.2: Plume Centerline Temperature Comparisons [80]

Heskestad	Case 1	Case 2	Case 3	Case 4
839 C	479 C	593 C	962 C	967 C

model. However, the basic transport algorithm is the same, as is the critical importance of grid sensitivity. In compiling sensitivity studies, only those that examined the sensitivity of routines no longer used have been excluded.

As part of a project to evaluate the use of FDS version 1 for large scale mechanically ventilated enclosures, Friday [79] performed a sensitivity analysis to find the approximate calculation time based on varying grid sizes. A propylene fire with a nominal heat release rate was modeled in FDS. There was no mechanical ventilation and the fire was assumed to grow as a function of the time from ignition squared. The compartment was a 3 m by 3 m by 6.1 m space. Temperatures were sampled 12 cm below the ceiling. Four grid sizes were chosen for the analysis: 30 cm, 15 cm, 10 cm, 7.5 cm. Temperature estimates were not found to change dramatically with different grid dimensions.

Using FDS version 1, Bounagui *et al.* [80] studied the effect of grid size on simulation results to determine the nominal grid size for future work. A propane burner 0.1 m by 0.1 m was modeled with a heat release rate of 1500 kW. The grid sizes used in the modeling are given in Table 5.1. The results of the model were compared against Heskestad's plume correlation. Table 5.2 shows the plume centerline temperature comparisons. Obviously, the smaller grids provide better agreements among predictive methods. A similar analysis was performed using Alpert's ceiling jet correlation [81] that also showed better predictions and reasonable agreement with smaller grid sizes.

Xin [82] used FDS (verson 1.0) to model a methane fueled square burner (1 m by 1 m) in the open. Engineering correlations for plume centerline temperature and velocity profiles were compared with model predictions to assess the influence of the numerical grid and the size of the computational domain. The results showed that FDS is sensitive to grid size effects, especially in the region near the fuel surface, and domain size effects when the domain width is less than twice the plume width. FDS uses a constant pressure assumption at open boundaries. This assumption will affect the plume behavior if the boundary of the computational domain is too close to the plume.

Ierardi and Barnett [83] used FDS version 3 to model a 0.3 m square methane diffusion burner with heat release rate values in the range of 14.4 kW to 57.5 kW. The physical domain used was 0.6 m by 0.6 m with uniform grid spacings of 15, 10, 7.5, 5, 3, 1.5 cm for all three coordinate directions. For both fire sizes, a grid spacing of 1.5 cm was found to provide the best agreement when compared to McCaffrey's centerline plume temperature and velocity correlations [35]. Two similar scenarios that form the basis for Alpert's ceiling jet correlation were also modeled with FDS. The first scenario was a 1 m by 1 m, 670 kW ethanol fire under a 7 m high unconfined ceiling. The planar dimensions of the computational domain were 14 m by 14 m. Four uniform grid spacings of 50, 33.3, 25, and 20 cm were used in the modeling. The best agreement

for maximum ceiling jet temperature was with the 33.3 cm grid spacing. The best agreement for maximum ceiling jet velocity was for the 50 cm grid spacing. The second scenario was a 0.6 m by 0.6 m 1000 kW ethanol fire under a 7.2 m high unconfined ceiling. The planar dimensions of the computational domain were 14.4 m by 14.4 m. Three uniform grid spacings of 60, 30, and 20 cm were used in the modeling. The results show that the 60 cm grid spacing exhibits the best agreement with the correlations for both maximum ceiling jet temperature and velocity on a qualitative basis.

Petterson [84] also completed work assessing the optimal grid size for FDS version 2. The FDS model predictions of varying grid sizes were compared to two separate fire experiments: The University of Canterbury McLeans Island Tests and the US Navy Hangar Tests in Hawaii. The first set of tests utilized a room with approximate dimensions of 2.4 m by 3.6 m by 2.4 m and fire sizes of 55 kW and 110 kW. The Navy Hangar tests were performed in a hangar measuring 98 m by 74 m by 15 m in height and had fires in the range of 5.5 MW to 6.6 MW. The results of this study indicate that FDS simulations with grids of 0.15 m had temperature predictions as accurate as models with grids as small as 0.10 m. Each of these grid sizes produced results within 15 % of the University of Canterbury temperature measurements. The 0.30 m grid produced less accurate results. For the comparison of the Navy Hangar tests, grid sizes ranging from 0.60 m to 1.80 m yielded results of comparable accuracy.

Musser *et al.* [85] investigated the use of FDS for course grid modeling of non-fire and fire scenarios. Determining the appropriate grid size was found to be especially important with respect to heat transfer at heated surfaces. The convective heat transfer from the heated surfaces was most accurate when the near surface grid cells were smaller than the depth of the thermal boundary layer. However, a finer grid size produced better results at the expense of computational time. Accurate contaminant dispersal modeling required a significantly finer grid. The results of her study indicate that non-fire simulations can be completed more quickly than fire simulations because the time step is not limited by the large flow speeds in a fire plume.

McGrattan *et al.* [86] showed that flame height is very sensitive to the grid size in simulations using coarse grids. To compensate, they implemented an alternative flame surface to account for the decrease in flame height with increasing grid cell size. This approximate flame surface is not needed when the grid is sufficiently refined. Details can be found in Section 3.3.2.

5.3 Large Eddy Simulation Parameters

FDS uses the Smagorinsky form of the Large Eddy Simulation (LES) technique. This means that instead of using the actual fluid viscosity, the model uses a viscosity of the form

$$\mu_{\rm LES} = \rho \left(C_s \Delta\right)^2 |S|^{\frac{1}{2}} \tag{5.1}$$

where C_s is an empirical constant, Δ is a length on the order of the size of a grid cell, and the deformation term $|S|$ is related to the Dissipation Function, given by Eq. (3.24). Related to the "turbulent viscosity" are comparable expressions for the thermal conductivity and material diffusivity:

$$k_{\rm LES} = \frac{\mu_{\rm LES}\, c_p}{\rm Pr} \quad ; \quad (\rho D)_{\rm LES} = \frac{\mu_{\rm LES}}{\rm Sc} \tag{5.2}$$

The Prandtl number Pr and the Schmidt number Sc are likewise considered to be "turbulent" values. Thus, C_s, Pr and Sc are a set of empirical constants. Most FDS users simply use the default values of (0.2,0.5,0.5), but some have explored their effect on the solution of the equations.

In an effort to validate FDS with some simple room temperature data, Zhang *et al.* [87] tried different combinations of the Smagorinsky parameters, and suggested the current default values. Of the three parameters, the Smagorinsky constant C_s is the most sensitive. Smagorinsky [25] originally proposed a value

of 0.23, but researchers over the past three decades have used values ranging from 0.1 to 0.23. There are also refinements of the original Smagorinsky model [26, 27, 28] that do not require the user to prescribe the constants, but rather generate them automatically as part of the numerical scheme.

5.4 Summary

The basis of large eddy simulation is that accuracy increases as the numerical mesh is refined. For fire applications, the grid sensitivity studies have shown that the accuracy of the model is a function of the characteristc fire diameter D^* divided by the grid cell size. It is not enough to describe the resolution of the calculation solely in terms of the grid cell size, but rather the grid cell size relative to the heat release rate. For non-fire applications, there are no simple means to evaluate "good resolution."

As a rule of thumb, in simulations of limited resolution FDS predictions are more reliable in the far-field because the substantial numerical diffusion mimics the unresolved sub-grid scale mixing. This is hard to quantify other than through comparisons with experiment. In some of the sensitivity studies discussed above, the authors conclude that the model works best with a cell size of a given value, and often this cell is not the smallest one tested. In these cases, the authors have found a flow scenario where the unresolved convective mixing is almost exactly offset by numerical diffusion. This is fortuitous, but the conclusion does not necessarily extend to other scenarios. The disadvantage of any turbulence model, large eddy simulation included, is that good results are not guaranteed on grids of limited resolution. The advantage of LES over other turbulence models is that the solution of the actual governing equations, not a temporal or spatial average, is obtained as the mesh is refined.

The same can be said for phenomena closer in to the fire. However, grid resolution is more critical for near-field phenomena because numerical diffusion near the fire on coarse grids does not have the same fortuitous effect as it does on far-field results. In general, coarse resolution will decrease temperatures and velocities by smearing the values over the large grid cells. This can affect the radiative flux, convection to surrounding solids, and ultimately flame spread and fire growth.

Chapter 6

Model Validation

6.1 Introduction

Model validation is a process where an one simulates a controlled experiment and assesses the degree of difference between measured and predicted quantities. The assessment involves the model's input parameters, its mathematical formulation of the physical phenomena, and its interpretation of the measurements. It is often difficult to sort out the major source of error, especially if the experiment is complicated. It is best if the experiment is designed purely to validate a model, in which case one can eliminate error sources by simplifying the geometry and materials. However, most fire experiments are performed for reasons other than simply to validate a model, and they often involve real materials burning in complicated spaces.

In this chapter, a survey of FDS validation work will be presented. Some of the work has been performed at NIST, some by its grantees and some by engineering firms using the model. Because each organization has its own reasons for validating the model, the referenced papers and reports do not follow any particular guidelines. Some of the works only provide a qualitative assessment of the model, concluding that the model agreement with a particular experiment is "good" or "reasonable." Sometimes, the conclusion is that the model works well in certain cases, not as well in others. These studies are included in the survey because the references are useful to other model users who may have a similar application and are interested in even qualitative assessment. It is important to note that some of the papers point out flaws in early releases of FDS that have been corrected or improved in more recent releases. Some of the issues raised, however, are still subjects of active research. The research agenda for FDS is greatly influenced by the feedback provided by users, often through publication of validation efforts.

6.2 Validation Work with Pre-Release Versions of FDS

FDS was officially released in 2000. However, for two decades various CFD codes using the basic FDS hydrodynamic framework were developed at NIST for different applications and for research. In the mid 1990s, many of these different codes were consolidated into what eventually became FDS. Before FDS, the various models were referred to as LES, NIST-LES, LES3D, IFS (Industrial Fire Simulator), and ALOFT (A Large Outdoor Fire Plume Trajectory).

The NIST LES model describes the transport of smoke and hot gases during a fire in an enclosure using the Boussinesq approximation, where it is assumed that the density and temperature variations in the flow are relatively small [9, 69, 71]. Such an approximation can be applied to a fire plume away from the fire itself. Much of the early work with this form of the model was devoted to the formulation of the low Mach number form of the Navier-Stokes equations and the development of the basic numerical algorithm. Early validation efforts compared the model with salt water experiments [59, 58], and fire plumes [88, 89, 90, 29].

Clement validated the hydrodynamic model in FDS by measuring salt water flows using Laser Induced dye Fluorescence (LIF) [91]. An interesting finding of this work was that the transition from a laminar to a turbulent plume is very difficult to predict with any technique other than DNS.

Eventually, the Boussinesq approximation was dropped and simulations began to include more fire-specific phenomena. Simulations of enclosure fires were compared to experiments performed by Steckler [67]. Mell *et al.* [66] studied small helium plumes, with particular attention to the relative roles of baroclinic torque and buoyancy as sources of vorticity. Cleary *et al.* [92] used the LES model to simulate the enviroment seen by multi-sensor fire detectors and performed some simple validation work to check the model before using it. Large fire experiments were performed by NIST at the FRI test facility in Japan, and at US Naval aircraft hangars in Hawaii and Iceland [93]. Room airflow applications were considered by Emmerich and McGrattan [94].

These early validation efforts were encouraging, but still pointed out the need to improve the hydrodynamic model by introducing the Smagorinsky form of large eddy simulation. This addition improved the stability of the model because of the relatively simple relation between the local strain rate and the turbulent viscosity. There is both a physical and numerical benefit to the Smagorinsky model. Physically, the viscous term used in the model has the right functional form to describe sub-grid mixing processes. Numerically, local oscillations in the computed flow quantities are damped if they become large enough to threaten the stability of the entire calculation.

During the 1980s and 1990s, the Building and Fire Research Laboratory at NIST studied the burning of crude oil under the sponsorship of the US Minerals Management Service. The aim of the work was to assess the feasibility of using burning as a means to remove spilled oil from the sea surface. As part of the effort, Rehm and Baum developed a special application of the LES model called ALOFT. The model was a spin-off of the two-dimensional LES enclosure model, in which a three-dimensional steady-state plume was computed as a two-dimensional evolution of the lateral wind field generated by a large fire blown in a steady wind. The ALOFT model is based on large eddy simulation in that it attempts to resolve the relevant scales of a large, bent-over plume. Validation work was performed by simulating the plumes from several large experimental burns of crude oil in which aereal and ground sampling of smoke particulate was performed [95]. Yamada [96] performed a validation of the ALOFT model for 10 m oil tank fire. The results indicate that the prediction of the plume cross section 500 m from the fire agree well with the experimental observations.

6.3 Validation of FDS since 2000

There is an on-going effort at NIST and elsewhere to validate FDS as new capabilities are added. To date, most of the validation work has evaluated the model's ability to predict the transport of heat and exhaust products from a fire through an enclosure. In these studies, the heat release rate is usually prescribed, along with the production rates of various products of combustion. More recently, validation efforts have moved beyond just transport issues to consider fire growth, flame spread, suppression, sprinkler/detector activation, and other fire-specific phenomena.

The validation work discussed below can be organized into several categories: Comparisons with full-scale tests conducted especially for the chosen evaluation, comparisons with previously published full-scale test data, comparisons with standard tests, comparisons with documented fire experience, and comparisons with engineering correlations. There is no single method by which the predictions and measurements are compared. Formal, rigorous validation exercises are time-consuming and expensive. Most validation exercises are done simply to assess if the model can be used for a very specific purpose. While not comprehensive on their own, these studies collectively constitute a valuable assessment of the model.

6.3.1 Comparison with Full-Scale Tests Conducted Specifically for the Chosen Evaluation

As part of the NIST investigation of the World Trade Center fires and collapse, a series of large scale fire experiments were performed specifically to validate FDS [97]. The tests were performed in a rectangular compartment 7.2 m long by 3.6 m wide by 3.8 m tall. The fires were fueled by heptane for some tests and a heptane/toluene mixture for the others. The fuel was sprayed from a nozzle into a steel pan. The compartment was heavily instrumented.

FDS simulations were performed before testing began to guide the design of the compartment and also to provide a baseline set of "blind" predictions[1]. A uniform numerical grid whose cells are 10 cm on a side was chosen based on a grid resolution study. The heat release rate (HRR) of the simulated burner was set to that which was measured in the experiments. No attempt was made to model the spray burner.

To quantify the accuracy of the predictions, the measured and predicted gas temperatures of the upper layer were compared for each test. Because the uncertainty of the measured HRR is often the major source of disagreement between model and experiment, an analysis was performed to assess how sensitive the measured temperatures were to changes in the HRR. According to an empirical correlation by McCaffrey, Quintiere and Harkleroad [98], the rise in the upper layer gas temperature ΔT_g in a compartment is related to the overall HRR by the relation

$$\Delta T_g = 6.85 \left(\frac{\dot{Q}^2}{A_0 \sqrt{H_0} h_k A_T} \right)^{\frac{1}{3}} \tag{6.1}$$

where $\dot{Q}$ is the HRR (kW), A_0 is the area of the opening (m^2), H_0 is the height of the opening (m), h_k is the thermal conductivity of the walls (kW/m/K), and A_T is the total area of the compartment walls (m^2). What is of importance here is the fact that the temperature rise is proportional to the HRR to the 2/3 power. The reported uncertainty in the heat release rate measurement was 5 % (one standard deviation). The 5 % uncertainty in the HRR corresponds to a 2/3 x 5 % = 3.3 % uncertainty in the temperature rise. For upper layer temperatures of approximately 600 °C, this translates to roughly 20 °C. The difference in measured and predicted upper layer temperatures ranged from 5 °C to 20 °C, meaning that the predictions were within the uncertainty range of the HRR. Even though there are uncertainties in the measurement of the temperature itself, the discrepancy between measurement and prediction can be explained solely in terms of the uncertainty in the HRR measurement.

To extend this analysis further, it was observed that the heat flux onto surfaces in the upper layer was very nearly given by σT^4 where $\sigma = 5.67 \times 10^{-11}$ kW/m^2/K^4 and T is the temperature in degrees K. In other words, the emissivity of the upper layer gases is nearly 1, not surprising given the high level of soot. Given the uncertainty in the upper layer temperature rise of 3.3 %, the uncertainty in absolute temperature at 600 °C is 2.3 %, leading to an estimate for the uncertainty in heat flux of 4 $\times$ 2.3 % = 9.2 %. In most instances, the difference between measurement and prediction was within 10 %, confirming that the model is within experimental uncertainty.

In the discussion above, it was shown that the FDS predicted upper layer temperatures and heat fluxes were within the uncertainty range of the experiment. For this exercise it was assumed that the uncertainty in the experiment was based solely on the uncertainty of the heat release rate measurement. Thus, it was shown how sensitive the upper layer temperature and heat flux measurements were to the heat release rate. In the numerical simulations there are dozens of input parameters prescribed by the model user. Often there is no way to assess the sensitivity of these parameters except by numerical experiment; that is, running the model with small changes to the base parameters to see what effect these have on the predictions. To this

[1] A blind prediction simply means that the calculation is performed before the experiment is conducted. At NIST, the results of a blind prediction are given to the engineers conducting the experiment so that they can be compared with the measurements immediately after the experiment is completed. This is an effective test the model, and also a good way to ensure that the measurements make sense.

end, the data set was exploited to assess the sensitivity of FDS to grid cell size, wall thermal properties, fire soot yield, radiation fraction, and various other quantities. Details can be found in Reference [97].

A second set of experiments to validate FDS for use in the World Trade Center investigation is documented in Ref. [99]. The intent of these tests was to evaluate the ability of the model to simulate the growth of a fire burning 3 office workstations within a compartment of dimensions 11 m by 7 m by 4 m, open at one end to mimic the ventilation of 5 windows similar to those in WTC 1 and 2. Six tests were performed with various initial conditions exploring the effect of jet fuel spray and ceiling tiles covering the surface of the desks and carpet. Measurements were made of the heat release rate and compartment gas temperatures at four locations using vertical thermocouple arrays. Six different material samples were tested in the NIST cone calorimeter: desk, chair, paper, computer case, privacy panel, and carpet. Data for the carpet, desk and privacy panel were input directly into FDS, with the other 3 materials lumped together to form an idealized fuel type. Open burns of single workstations were used to calibrate the simplified fuel package. Then FDS was used to make blind predictions of the 3 workstation fires within the compartment. Peak heat release rates and temperatures were predicted to within 20 % for all tests.

6.3.2 Comparison with Engineering Correlations

There are several examples of fire flows that have been extensively studied, so much so that a set of engineering correlations combining the results of many experiments have been developed. These correlations are useful to modelers because of their simplicity. The most studied phenomena include fire plumes, ceiling jets, and flame heights.

Although much of the early validation work before FDS was released involved fire plumes, it remains an active area of interest. One study by Chow and Yin [100] surveys the performance of various models in predicting plume temperatures and entrainment. They compare various correlations, a RANS (Reynolds-Averaged Navier-Stokes) model, and FDS. Simulations were carried out which replicated a 470 kW fire with a diameter of 1 m and an unbounded ceiling. A numerical grid size of 96 by 96 by 96 cells was used in the FDS calculation and provided results that agreed well with those predicted by the RANS model and the various correlations.

Battaglia *et al.* [101] used FDS to simulate fire whirls. First, the model was shown to reproduce the McCaffrey correlation of a fire plume, then it was shown to reproduce qualitatively certain features of fire whirls. At the time, FDS used Lagrangian elements to introduce heat from the fire (no longer used), and this combustion model could not replicate the extreme stretching of the core of the flame zone.

Quintiere and Ma [32, 33, 34] compared predicted flame heights and plume centerline temperatures to empirical correlations. For plume temperature, the Heskestad correlation [35] was chosen. Favorable agreement was found in the plume region, but the results near the flame region were found to be grid-dependent, especially for low Q^* fires. At this same time, researchers at NIST were reaching similar conclusions, and it was noticed by both teams that a critical parameter for the model is $D^*/\delta x$, where D^* is the characteristic fire diameter and δx is the grid cell size. If this parameter is sufficiently large, the fire can be considered well-resolved and agreement with various flame height correlations was found. If the parameter is not large enough, the fire is not well-resolved and adjustments must be made to the combustion routine to account for it. See Section 3.3.2 for more details.

6.3.3 Comparisons with Previously Published Full-Scale Test Data

Experiments conducted solely for model validation are somewhat rare. More common are validation studies that use data from past experiments. This section contains brief descriptions of work published comparing FDS with past experiments or correlations of experimental data.

Pool Fires

Xin [68] used FDS to model a simple 1 m diameter methane pool fire. The computational domain was 2 m by 2 m by 4 m with a uniform grid size of 2.5 cm. The predicted results were compared to experimental data and found to qualitatively and quantitatively reproduce the velocity field.

Hostikka *et al.* [102] modeled small pool fires of methane and methanol to test the FDS radiation solver for low-sooting fires. They conclude that the predicted radiative fluxes for both fuels are higher than measured values, especially at small heat release rates, due to an over-prediction of the gas temperature.

Hietaniemi, Hostikka and Vaari [103] consider heptane pool fires of various diameters. Predictions of the burning rate as a function of diameter follow the trend observed in a number of experimental studies. Their results show an improvement in the model over the earlier work with methanol fires, due to improvements in the radiation routine and the fact that heptane is more sooty than methanol, simplifying the treatment of radiation. The authors point out that reliable predictions of the burning rate of liquid fuels require roughly twice as fine a grid spanning the burner than would be necessary to predict plume velocities and temperatures. The reason for this is the prediction of the heat feedback to the burning surface necessary to *predict* rather than to *prescribe* the burning rate.

Airflows in Non-Fire Compartments

The low Mach number assumption in FDS is appropriate not only to fire, but to most building ventilation scenarios. An example of how the model can be used to assess indoor air quality is presented by Musser *et al.* [85]. The test compartment was a displacement ventilation test room that contained computers, furniture, and lighting fixtures as well as heated rectangular boxes intended to represent occupants. A detailed description of the test configuration is given by Yuan *et al.* [104]. The room is ventilated with cool supply air introduced via a diffuser that is mounted on a side wall near the floor. The air rises as it is warmed by heat sources and exits through a return duct located in the upper portion of the room. The flow pattern is intended to remove contaminants by sweeping them upward at the source and removing them from the room. Sulphur hexafluoride, SF_6, was introduced into the compartment during the experiment as a tracer gas near the breathing zone of the occupants. Temperature, tracer concentration, and velocity were measured during the experiments. For temperature, the two finest grids (50 by 36 by 24 and 64 by 45 by 30) produced results in which the agreement between the measurement and prediction was considered acceptable. The agreement for the tracer concentrations were not as good. It was suggested that the difference could be related to the way the source of the tracer gas was modeled. The comparison of velocity data was deemed reasonable, given the limitations of the velocity probes at low velocities.

Mniszewski [105] used FDS to model the release of flammable gases in simple enclosures and open areas. In this work, the gases were not ignited.

Kerber and Walton provided a comparison between FDS version 1 and experiments on positive pressure ventilation in a full-scale enclosure without a fire. The model predictions of velocity were within 10 % to 20 % of the experimental values [106].

Wind Engineering

Most applications of FDS involve fires within buildings. However, it can be used to model thermal plumes in the open and wind impinging on the exterior of a building. Rehm, McGrattan, Baum and Simiu [107] use the LES solver to estimate surface pressures on simple rectangular blocks in a crosswind, and compare these estimates to experimental measurements. In a subsequent paper [108], they consider the qualitative effects of multiple buildings and trees on a wind field.

A different approach to wind is taken by Wang and Joulain [109]. They consider a small fire in a wind tunnel 0.4 m wide and 0.7 m tall with flow speeds of 0.5 m/s to 2.5 m/s. Much of the comparison

Table 6.1: T51 Test Results [112]

Quantity	Experimental Data	FDS
Upper Temperature °C	730	808
Upper Velocity (m/s)	4.5	2.8
Lower Velocity (m/s)	2.3	1.1
Layer Height (m)	1.0	0.9
O_2 Concentration (%)	11.6	7.6

with experiment is qualitative, including flame shape, lean, length. They also use the model to determine the predominant modes of heat transfer for different operating conditions. To assess the combustion, they implement an "Eddy Break-up" combustion model [110] and compare it to the mixture fraction approach used by FDS. The two models perform better or worse, depending on the operating conditions. Some of the weaknesses of the mixture fraction model as implemented in FDS version 2 are addressed in subsequent versions. The Eddy Break-up approach has not been implemented in the official version of FDS.

Growing Fires

Vettori [111] modeled two different fire growth rates in an obstructed ceiling geometry. The rectangular compartment was 9.2 m by 5.6 m by 2.4 m with a hollow steel door to the outside that remained closed during the tests. An open wooden stairway led to an upper floor with the same dimensions as the fire compartment below. Wooden joists measuring 0.038 m by 0.24 m were spaced at 0.41 m intervals across the ceiling and were supported by a single steel beam that spanned the width of the room. A rectangular methane gas burner measuring 0.7 m by 1.0 m by 0.31 m was placed in the corner of the chamber. Slow and fast burning fires that reached 1055 kW in 600 s and 150 s, respectively, were monitored. Four vertical arrays of Type K thermocouples were used to measure temperatures during the tests. The FDS model used four grid refinements and piecewise linear grid spacing for each fire growth rate (slow and fast). For the fast growing fire, the predicted temperatures were within 20 % of the measured values and within 10 % for the slow growing fire. In general, finer grids produced better agreement.

Floyd [112] validated FDS by comparing the modeling results with measurements from fire tests at the Heiss-Dampf Reaktor (HDR) facility. The structure was originally the containment building for a nuclear power reactor in Germany. The cylindrical structure was 20 m in diameter and 50 m in height topped by a hemispherical dome 10 m in radius. The building was divided into eight levels. The total volume of the building was approximately 11,000 m^3. From 1984 to 1991, four fire test series were performed within the HDR facility. The T51 test series consisted of eleven propane gas tests and three wood crib tests. To avoid permanently damaging the test facility, a special set of test rooms were constructed, consisting of a fire room with a narrow door, a long corridor wrapping around the reactor vessel shield wall, and a curtained area centered beneath a maintenance hatch. The fire room walls were lined with fire brick. The doorway and corridor walls had the same construction as the test chamber. Six gas burners were mounted in the fire room. The fuel source was propane gas mixed with 10 % air fed at a constant rate to one of the six burners. For comparison with the FDS model, only the fire room, hallway and curtained region was input into the model, for a total of 450,000 grid cells. The burners were defined within FDS as separate vents with a constant inlet velocity. Two sets of burners were created, the first set at the physical location of the burners as the source of fuel and second set directly above the first set as a source for ambient air. The data was presented at fifteen minutes into the fire. The results comparing the measured data and the predicted data are presented in Table 6.1. The FDS model predicted the layer height and temperature of the space to within 10 % of the

experimental values [112].

FDS predictions of fire growth and smoke movement in large spaces were presented by Kashef [113]. The experiments were conducted at the National Research Council Canada. The tests were performed in a compartment with dimensions of 9 m by 6 m by 5.5 m with 32 exhaust inlets and a single supply fan. A burner generated fires ranging in size from 15 kW to 1000 kW. FDS produced good predictions of the experimental layer temperatures and interface heights, but there was some disagreement in the shape of the temperature profiles.

Flame Spread

FDS was evaluated to predict the heat transfer to the wall from an adjacent pool fire. The experimental results were based on the work by Beck *et al.* The predicted heat flux was in agreement with the experimental results. The temperatures are within 30 % of the measured values near the base of the wall but decrease more rapidly than the experimental measurements. The difference between the experimental and predicted values can be attributed to the combustion model within FDS.

The flame spread calculations from FDS were compared to the vertical flame spread over a 5 m slab of PMMA performed by Factory Mutual Research Corporation (FMRC). The predicted flame spread rate was within 0.3 m/s for any point in time during the analysis. The comparison at the quasi-steady burning rate once the full slab was burning shows that FDS over-estimated the burning rate [32, 33, 34].

Response of Active and Passive Fire Protection

A significant validation effort for sprinkler activation and suppression was a project entitled the International Fire Sprinkler, Smoke and Heat Vent, Draft Curtain Fire Test Project organized by the National Fire Protection Research Foundation [114]. Thirty-nine large scale fire tests were conducted at Underwriters Laboratories in Northbrook, IL. The tests were aimed at evaluating the performance of various fire protection systems in large buildings with flat ceilings, like warehouses and “big box” retail stores. All the tests were conducted under a 30 m by 30 m adjustable-height platform in a 37 m by 37 m by 15 m high test bay. At the time, FDS had not been publicly released and was referred to as the Industrial Fire Simulator (IFS), but it was essentially the same as FDS version 1.

For model validation of sprinkler activation, the most valuable experiments performed were a series of heptane spray fires. With the spray burner in different locations, with and without draft curtains, with and without vertical vents, the model made predictions of sprinkler activation and upper layer temperatures. For all tests, the first ring of sprinklers surrounding the fire activated within 15 % of the experimental times; within 25 % for the second ring. The gas temperatures near the ceiling were predicted to within about 15 % of the measured values.

Most of the full-scale experiments performed during the project used a heptane spray burner to generate controlled fires of 1 MW to 10 MW. However, 5 experiments were performed with 6 m high racks containing the Factory Mutual Standard Plastic Commodity, or Group A Plastic. To model these fires, bench scale experiments were performed to characterize the burning behavior of the commodity, and larger test fires provided validation data with which to test the model predictions of the burning rate and flame spread behavior [50, 51]. Two to four tier configurations were evaluated. For the period of time prior to application of water, the simulated heat release rate was within 20 % of the experimental heat release rates. It should be noted that the model was very sensitive to the thermal parameters and the numerical grid when used to model the fire growth in the piled commodity tests.

High rack storage fires of pool chemicals were modeled by Olenick *et al.* [115] to determine the validity of sprinkler activation predictions of FDS. The model was compared to full-scale fires conducted in January,

2000 at Southwest Research Institute in San Antonio, Texas. The results indicated that the model accurately predicted sprinkler activation and the over-pressurization of the test compartment.

Airflows in Fire Compartments

Cochard [116] used FDS to study the ventilation within a tunnel. He compared the model results with a full-scale tunnel fire experiment conducted as part of the Massachusetts Highway Department Memorial Tunnel Fire Ventilation Test Program (the test cited is 321A) [117]. The test consisted of a single point supply of fresh air through a 28 m^2 opening in a 135 m tunnel. The ventilation was started 2 min after the ignition of a 40 MW fire. Fifteen temperature measurement trees were placed within the tunnel and replicated within the model. Depending on location, the difference between predicted and measured temperature rise ranged from 10 % to 20 %.

McGrattan and Hamins [118] also applied FDS to simulate two of the Memorial Tunnel Fire Tests as validation for the use of the model in studying an actual fire in the Howard Street Tunnel, Baltimore, Maryland, July 2001. The experiments chosen for the comparison were unventilated. One experiment was a 20 MW fire; the other a 50 MW fire. FDS predictions of peak near-ceiling temperatures were within 50 °C of the measured peak temperatures, which were 600 °C and 800 °C, respectively.

Friday studied the use of FDS in large scale mechanically ventilated spaces. The ventilated enclosure was provided with air injection rates of 1 to 12 air changes per hour and a fire with heat release rates ranging from 0.5 MW to 2 MW. The test measurements and model output were compared to assess the accuracy of FDS [79].

Zhang *et al.* [87] utilized the FDS model to predict turbulence characteristics of the flow and temperature fields due to fire in a compartment. The experimental data was acquired through tests that replicated a half-scale ISO Room Fire Test. Two cases were explored: the heat source in the center of the room and the heat source adjacent to a wall. The heat source was a heating element with an output of 12 kW/m^2 and was assumed stable after 300 s. For the first case, the predicted average velocity and temperature profiles were found to "agree reasonably well." Near the ceiling, the model under-predicted temperature and over-predicted velocity. The predicted intensity of the temperature fluctuation "agree[d] very well" at all points except those directly adjacent to the burner. The turbulent heat flux was found to be larger in the region above the heat source.

The second case also used a burner with a 12 kW/m^2 heat source located at the wall. As with the first case, the predicted mean velocities agree with the experimental results except near the ceiling. The temperatures near the ceiling were found to be over-predicted by FDS. The intensity of the velocity fluctuation was found to "agree well" with the experimental data except near the ceiling. The predicted intensity of the temperature fluctuation agrees "very well" with the experimental data except in the region near the middle of the room. This might be due to the influence of the door sill. Overall, in both cases, the predicted values agreed well with the experimental values in all regions except near the ceiling.

The ability of version 1 of FDS to accurately predict smoke detector activation was studied by D'Souza [119]. The smoke transport model within FDS was tested and compared with UL 217 test data. The second step in this research was to further validate the model with full-scale multi-compartment fire tests. The results indicated that FDS is capable of predicting smoke detector activation when used with smoke detector lag correlations that correct for the time delay associated with smoke having to penetrate the detector housing.

Cleary [120] also provided a comparison between FDS computed gas velocity, temperature and concentrations at various detector locations. The research concluded that multi-room fire simulations with the FDS model can accurately predict the conditions that a sensor might experience during a real fire event. The FDS model was able to predict the smoke and gas concentrations, heat, and flow velocities at various detector locations to within 15 % of measurements.

Piergoirgio *et al.* [121] provided a qualitative analysis of FDS applied to a truck fire within a tunnel.

Table 6.2: Comparison of FDS and measured quantities in a half-scale ISO 9705 compartment [122]

Parameter	VTFRL	FDS
Room TC 1	191 °C	134 °C
Door TC 5	348 °C	365 °C
Room TC 5	585 °C	529 °C
Door TC 8	227 °C	409 °C
Room TC 8	625 °C	559 °C
Door Vel 1	4.4 m/s	3.3 m/s
Door O_2 1	14.6 %	13.9 %
Door Vel 5	-0.54 m/s	-0.75 m/s
Door O_2 5	21.0 %	21.0 %
Room HF1	29 kW/m^2	26 kW/m^2
Door $CO_2$1	3.5 %	3.8 %
Door HF2	3.6 kW/m^2	4.1 kW/m^2
Door $CO_2$4	0.2 %	2.2 %

The goal of their analysis was to describe the spread of the toxic gases within the tunnels, to determine the places not involved in the spreading of combustion products and to quantify the oxygen, carbon monoxide and hydrochloric acid concentrations during the fire.

Combustion Model

Floyd *et al.* [122] compared the radiation model of FDS version 2 with full-scale data from the Virginia Tech Fire Research Laboratory (VTFRL). The test compartment was outfitted with equipment capable of taking temperature, air velocity, gas concentrations, unburned hydrocarbon and heat flux measurements. The test facility consisted of a single compartment which replicated the ISO 9705 standard compartment with dimensions of 1.2 m by 1.8 m by 1.2 m in height. The ceiling and walls were constructed of fiberboard over a steel shell with a floor of concrete. Three baseline experiments were completed with fires ranging in size from 90 kW to 440 kW. A sample of the test results are presented in Table 6.2.

Overall, FDS predicted the temperatures to within 15 % of the measured temperatures. The FDS velocity measurements followed the trend of the test data but did not replicate it. The outgoing velocities were under-predicted by 30 % to 40 % and the incoming velocities were over-predicted by 40 %. FDS predicted the heat flux gauge response to within 10 % of the measured values. The radiation model in FDS predicted the measured fluxes to within 15 %. The radiation to and from the compartment wall was estimated well. The mixture fraction model was also successful. For well ventilated tests, the predictions were excellent. The quality of the FDS prediction decreased with the under-ventilated cases. The main source of error with the model predictions in the under-ventilated cases was the over-prediction of compartment gas temperatures and the size of the upper layer [123].

Xin and Gore [82] provides a comparison between FDS predictions and measurements of the spectral radiation intensities of small fires. The fuel flow rates for methane and ethylene burners were selected so that the Froude numbers matched that of liquid toluene pool fires. The heat release rate was 4.2 kW for the methane flame and 3.4 kW for the ethylene flame. Line of sight spectral radiation intensities were measured at six downstream locations. The spectral radiation intensity calculations were performed by post-processing the transient scalar distributions provided by FDS. The calculated and measured spectral radiation intensities were found to be in “excellent” agreement for the gas radiation bands.

Zhang *et al.* [60] compared the experimental results of a circular methane gas burner to predictions computed by FDS. The compartment was 2.8 m by 2.8 m by 2.2 m high with natural ventilation from a standard door. Good agreement was found for the temperature prediction at the doorway where the radiation model was used. The FDS model predicted the temperatures at the corner of the room better than other models compared by the group. It was found that, overall, FDS predicted temperatures well but the prescribed turbulent Prandtl and Schmidt numbers play an important role in determining the accuracy of the model.

Dillon and Hamins [124] studied the use of FDS in providing data and correlations for fire investigators to support their investigations. A paraffin wax candle was placed within a 0.61 m by 0.61 m by 0.76 m plexi-glass enclosure. The chamber was raised 20 mm off the surface to reveal 44 uniformly spaced 6 mm diameter holes. The holes provided oxygen to the flame without subjecting the flame to a draft. A 150 mm hole was provided at the top of the enclosure to allow for the heat and combustion products to exit the space. The heat flux from the candle flame was modeled with FDS. The model provides a prediction of the heat flux of the candle at a height of 56 mm above the base of the flame with an accuracy of 5 %. The flux is under predicted by 16 % at 76 mm above the base of the flame. The remainder of the predictions show flux measurements were under-predicted by 15 % to 40 % of the measured values.

6.3.4 Comparison with Standard Tests

Standard fire tests are performed at various testing laboratories and universities around the world. While most were not designed as validation tools, they nevertheless can be used as relatively simple, well characterized fire experiments.

An extensive amount of validation work with FDS version 4 has been performed by Hietaniemi, Hostikka, and Vaari at VTT, Finland [103]. The case studies are comprised of fire experiments ranging in scale from the cone calorimeter (ISO 5660-1, 2002) to full-scale fire tests such as the room corner test (ISO 9705, 1993). Comparisons are also made between FDS 4 results and data obtained in the SBI (Single Burning Item) Euroclassification test apparatus (EN 13823, 2002) as well as data obtained in two *ad hoc* experimental configurations: one is similar to the room corner test but has only partial linings and the other is a space to study fires in building cavities. In the study of upholstered furniture, the experimental configurations are the cone and furniture calorimeters, and the ISO room. For liquid pool fires, comparison is made to data obtained by numerous researchers. The burning materials include spruce timber, MDF (Medium Density Fiber) board, PVC wall carpet, upholstered furniture, cables with plastic sheathing, and heptane. The cases studied are summarized in Table 6.3.

The scope of the VTT work is considerable. Assessing the accuracy of the model must be done on a case by case basis. In some cases, predictions of the burning rate of the material were based solely on its fundamental properties, as in the heptane pool fire simulations. In other cases, some properties of the material are unknown, as in the spruce timber simulations. Thus, some of the simulations are true predictions, some are calibrations. The intent of the authors was to provide guidance to engineers using the model as to appropriate grid sizes and material properties. In many cases, the numerical grid was made fairly coarse to account for the fact that in practice, FDS is used to model large spaces of which the fuel may only comprise a small fraction.

6.3.5 Comparison with Documented Fire Experience

Documented fire experience includes known behavior of materials in fires, eyewitness accounts of real fires, observed post fire conditions, and other means. To date, several actual fires have been reconstructed using FDS. One case study performed by NIST is documented in Ref. [125]. Two firefighters were killed and one severely injured in a townhouse fire in Washington, D.C. during the evening of May 30, 1999. Questions arose about the injuries the firefighters had sustained, the lack of thermal damage in the living room where

Table 6.3: Summary of materials and test methods considered in VTT study [103]

Burning material	Experimental Configuration
10 mm thick spruce timber	Cone calorimeter SBI test Room corner test
22 mm thick spruce timber	Modified room corner test 6 m by 1.1 m by 0.5 m cavity
12 mm thick MDF board	Cone calorimeter SBI test Room corner test
PVC wall carpet on gypsum plasterboard	Cone calorimeter SBI test Room corner test
Upholstered furniture: a chair with PU padding and PP fabric	Cone calorimeter Furniture calorimeter ISO room test
Cables with plastic sheathing	6 m by 1.2 m by 0.6 m cavity lined with non-combustible board
Heptane	Pool fires of various sizes

a fallen fire fighter was found and why the firefighters never opened their hose lines to protect themselves or to extinguish the fire.

To answer some of the questions, a rectangular volume of 10 m by 6 m by 5.1 m was divided into 76,500 cells in the FDS model. The FDS results that best replicated the observed fire behavior indicated that the opening of the basement sliding glass door provided oxygen to a pre-heated, under-ventilated fire. Flashover was estimated to occur in less than 60 s following the entry of firefighters into the basement. The resulting fire gases flowed up the basement stairs and moved across the living room ceiling towards the back wall of the townhouse. These hot gases came in direct contact with the firefighters who were killed. The hot gases traversed the townhouse in less than 2 s, giving the firefighters little time to respond. The model showed that the oxygen level was too low to support flaming and, therefore, the firefighters did not have a visual cue of the thermal conditions until it was too late. Results of the FDS study were shared with the D.C. fire department and have been made available via a multi-media CD-ROM to other fire departments across the country.

Another case study performed at NIST involved a fire in a Houston restaurant [126]. On the morning of February 14, 2000, a fire started in the office area of a fast food restaurant. Two firefighters died when the roof collapsed. The FDS model was used to simulate the fire. The fuel was assumed to be the contents of a typical office, and the fire was assumed to have a slowly growing heat release rate peaking at 6 MW. Multiple vents were modeled and the time at which they opened replicated the firefighters' actions after arrival. The model provided a visual representation of the fire during the initial phases until the collapse of the roof.

NIST also performed a case study on a fire that killed three children and three firefighters on the morning of December 22, 1999 [127]. The fire started on top of a stove in a two-story residence. FDS was used to simulate the fire. The fuel packages consisted of several furniture items in the kitchen and living room with heat release rates reaching 5.2 MW. The model results indicated the critical event in the fire was flashover of the kitchen. The fire became a multi-room event after flashover with temperatures increasing to over

600 °C. The hot gases spread quickly from the living room to the stairway on the second floor trapping the firefighters.

Chapter 7

Conclusion

The equations and numerical algorithm described in this document form the core of an evolving fire model. As research into specific fire-related phenomena continues, the relevant parts of the model can be improved. Because the model was originally designed to predict the transport of heat and exhaust products from fires, it can be used reliably when the fire is prescribed and the numerical grid is sufficiently resolved to capture enough of the flow structure for the application at hand. It is the job of the user to determine what level of accuracy is needed. For simulations that simply involve mass and heat transport, the model predicts flow velocities and temperatures to an accuracy of 5 % to 20% compared to experimental measurements, depending on the fidelity of the underlying grid. Current research efforts focus on improving both the gas phase and solid phase descriptions of combustion so that phenomena such as flame spread, fire growth, under-ventilation, and suppression can be handled more reliably.

Any user of the numerical model must be aware of the assumptions and approximations being employed. There are two issues for any potential user to consider before embarking on calculations. First, for both real and simulated fires, the growth of the fire is very sensitive to the thermal properties (conductivity, specific heat, density, burning rate, *etc.*) of the surrounding materials. Second, even if all the material properties are known, the physical phenomena of interest may not be simulated due to limitations in the model algorithms or numerical grid. Except for those few materials that have been studied to date at NIST, the user must supply the thermal properties of the materials, and then validate the performance of the model with experiments to ensure that the model has the necessary physics included. Only then can the model be expected to predict the outcome of fire scenarios that are similar to those that have actually been tested.

Nomenclature

A_s	water droplet surface area
B	pre-exponential factor for Arrhenius reaction
C	Sprinkler C-Factor
C_D	drag coefficient
C_s	Smagorinsky constant (LES)
c_p	constant pressure specific heat
D	diffusion coefficient
D^*	characteristic fire diameter
d_m	median volumetric droplet diameter
E	activation energy
$\mathbf{f}$	external force vector (excluding gravity)
g	acceleration of gravity
$\mathcal{H}$	total pressure divided by the density
h	enthalpy; heat transfer coefficient
h_i	enthalpy of ith species
h_i^0	heat of formation of ith species
I	radiation intensity
I_b	radiation blackbody intensity
k	thermal conductivity; suppression decay factor
M	molecular weight of the gas mixture
M_i	molecular weight of ith gas species
$\dot{m}''_f$	fuel mass flux
$\dot{m}'''_i$	mass production rate of ith species per unit volume
$\dot{m}''_w$	water mass flux
m''_w	water mass per unit area
$\dot{m}''_O$	oxygen consumption rate per unit area
Nu	Nusselt number
Pr	Prandtl number
p	pressure
p_0	background pressure
$\tilde{p}$	pressure perturbation
$\mathbf{q}_r$	radiative heat flux vector
$\dot{q}'''$	heat release rate per unit volume
$\dot{q}''_r$	radiative flux to a solid surface
$\dot{q}''_c$	convective flux to a solid surface
$\dot{Q}$	total heat release rate
Q^*	characteristic fire size
$\mathcal{R}$	universal gas constant

Re	Reynolds number
r_d	water droplet radius
RTI	Response Time Index of sprinkler
$\mathbf{s}$	unit vector in direction of radiation intensity
Sc	Schmidt number
Sh	Sherwood number
T	temperature
t	time
t_b	thermal element burn-out time (LES)
U	integrated radiant intensity
$\mathbf{u} = (u, v, w)$	velocity vector
$\dot{m}_i'''$	production rate of ith species per unit volume
We	Weber number
$\mathbf{x} = (x, y, z)$	position vector
X_i	volume fraction of ith species
Y_i	mass fraction of ith species
Y_O^∞	mass fraction of oxygen in the ambient
Y_F^I	mass fraction of fuel in the fuel stream
y_s	soot yield
Z	mixture fraction
γ	ratio of specific heats; Rosin-Rammler exponent
ΔH	heat of combustion
ΔH_O	energy released per unit mass oxygen consumed
δ	wall thickness
κ	absorption coefficient
μ	dynamic viscosity
ν_i	stoichiometric coefficient, species i
Φ	dissipation function
ρ	density
τ	viscous stress tensor
χ_r	radiative loss fraction
σ	Stefan-Boltzmann constant
σ_d	droplet scattering coefficient
σ_s	scattering coefficient
$\omega = (\omega_x, \omega_y, \omega_z)$	vorticity vector

Bibliography

[1] S. Olenick and D. Carpenter. Updated International Survey of Computer Models for Fire and Smoke. *Fire Protection Engineering*, 13(2):87–110, May 2003.

[2] R. Friedman. Survey of Computer Models for Fire and Smoke. Technical report, Factory Mutual Research Corporation, Norwood, Massachusetts, March 1990.

[3] American Society for Testing and Materials, West Conshohocken, Pennsylvania. *ASTM E 1355-04, Standard Guide for Evaluating the Predictive Capabilities of Deterministic Fire Models*, 2004.

[4] H.C. Hottel. Stimulation of Fire Research in the United States After 1940. *Combustion Science and Technology*, 39:1–10, 1984.

[5] W.W. Jones. A Review of Compartment Fire Models. NBSIR 83-2684, National Bureau of Standards (now NIST), Gaithersburg, Maryland, 1983.

[6] J. Quintiere. A Perspective on Compartment Fire Growth. *Combustion Science and Technology*, 39:11–54, 1984.

[7] G.P. Forney and W.F. Moss. Analyzing and Exploiting Numerical Characteristics of Zone Fire Models. *Fire Science and Technology*, 14:49–60, 1994.

[8] S.V. Patankar. *Numerical Heat Transfer and Fluid Flow*. Hemisphere Publishing, New York, 1980.

[9] R.G. Rehm and H.R. Baum. The Equations of Motion for Thermally Driven, Buoyant Flows. *Journal of Research of the NBS*, 83:297–308, 1978.

[10] E.S. Oran and J.P. Boris. *Numerical Simulation of Reactive Flow*. Elsevier Science Publishing Co., Inc., New York, 1987.

[11] K.B. McGrattan and G.P. Forney. Fire Dynamics Simulator (Version 4), User's Guide. NIST Special Publication 1019, National Institute of Standards and Technology, Gaithersburg, Maryland, July 2004.

[12] G.P. Forney and K.B. McGrattan. User's Guide for Smokeview Version 4. NIST Special Publication 1017, National Institute of Standards and Technology, Gaithersburg, Maryland, July 2004.

[13] D.A. Anderson, J.C. Tannehill, and R.H. Pletcher. *Computational Fluid Mechanics and Heat Transfer*. Hemisphere Publishing Corp., Philadelphia, Pennsylvania, 1984.

[14] R. Peyret and T.D. Taylor. *Computational Methods for Fluid Flow*. Springer-Verlag, New York, 1983.

[15] J.H. Ferziger and M. Perić. *Computational Methods for Fluid Dynamics*. Springer-Verlag, New York, 1997.

[16] R.W. Bilger. *Turbulent Reacting Flows*, chapter 4. Turbulent Flows with Nonpremixed Reactants. Springer-Verlag, 1980.

[17] J.P. Holman. *Heat Transfer*. McGraw-Hill, New York, 5th edition, 1989.

[18] F.P. Incropera and D.P. De Witt. *Fundamentals of Heat and Mass Transfer*. John Wiley and Sons, New York, 3rd edition, 1990.

[19] R. Siegel and J. R. Howell. *Thermal Radiation Heat Transfer*. Hemisphere Publishing Corp., Philadelphia, Pennsylvania, 3rd edition, 1992.

[20] *SFPE Handbook of Fire Protection Engineering*. National Fire Protection Association, Quincy, Massachusetts, 3rd edition, 2002.

[21] D. Drysdale. *An Introduction to Fire Dynamics*. John Wiley and Sons, New York, 2nd edition, 2002.

[22] J.G. Quintiere. *Principles of Fire Behavior*. Delmar Publishers, Albany, New York, 1998.

[23] V. Babrauskas. *Ignition Handbook*. Fire Science Publishers, Issaquah, Washington USA, 1st edition, 2003. Co-published by the Society of Fire Protection Engineers.

[24] H.R. Baum and K.B. McGrattan. Simulation of Large Industrial Outdoor Fires. In *Fire Safety Science – Proceedings of the Sixth International Symposium*. International Association for Fire Safety Science, 1999.

[25] J. Smagorinsky. General Circulation Experiments with the Primitive Equations. I. The Basic Experiment. *Monthly Weather Review*, 91(3):99–164, March 1963.

[26] J.W. Deardorff. Numerical Investigation of Neutral and Unstable Planetary Boundary Layers. *Journal of Atmospheric Sciences*, 29:91–115, 1972.

[27] M. Germano, U. Piomelli, P. Moin, and W.H. Cabot. A Dynamic Subgrid-Scale Eddy Viscosity Model. *Physics of Fluids A*, 3:1760–1765, 1991.

[28] D.K. Lilly. A Proposed Modification of the Germano Subgrid-Scale Closure Method. *Physics of Fluids A*, 4:633–635, 1992.

[29] H.R. Baum, K.B. McGrattan, and R.G. Rehm. Three Dimensional Simulations of Fire Plume Dynamics. *Journal of the Heat Transfer Society of Japan*, 35:45–52, 1997.

[30] R.C. Reid, J.M. Prausnitz, and B.E. Poling. *Properties of Gases and Liquids*. McGraw-Hill, Inc., New York, 4th edition, 1987.

[31] C. Huggett. Estimation of the Rate of Heat Release by Means of Oxygen Consumption Measurements. *Fire and Materials*, 4(2):61–65, June 1980.

[32] T. Ma. Numerical Simulation of an Axi-symmetric Fire Plume: Accuracy and Limitations. Master's thesis, University of Maryland, 2001.

[33] T. Ma and J. Quintiere. Application of CFD Modeling to Room Fire Growth on Walls. NIST GCR 03-849, National Institute of Standards and Technology, Gaithersburg, Maryland, April 2003.

[34] T. Ma and J. Quintiere. Numerical Simulation of Axi-Symmetric Fire Plumes: Accuracy and Limitations. *Fire Safety Journal*, 38:467–492, 2003.

[35] G. Heskestad. *SFPE Handbook of Fire Protection Engineering*, chapter Fire Plumes, Flame Height and Air Entrainment. National Fire Protection Association, Quincy, Massachusetts, 3rd edition, 2002.

[36] C. Beyler. *SFPE Handbook of Fire Protection Engineering*, chapter Flammability Limits of Premixed and Diffusion Flames. National Fire Protection Association, Quincy, Massachusetts, 3rd edition, 2002.

[37] I.K. Puri and K. Seshadri. Extinction of Diffusion Flames Burning Diluted Methane and Diluted Propane in Diluted Air. *Combustion and Flame*, 65:137–150, 1986.

[38] C.K. Westbrook and F.L. Dryer. Simplified Reaction Mechanisms for the Oxidation of Hydrocarbon Fuels in Flames. *Combustion Science and Technology*, 27:31–43, 1981.

[39] W. Grosshandler. RadCal: A Narrow Band Model for Radiation Calculations in a Combustion Environment. NIST Technical Note TN 1402, National Institute of Standards and Technology, Gaithersburg, Maryland, 1993.

[40] G.D. Raithby and E.H. Chui. A Finite-Volume Method for Predicting Radiant Heat Transfer in Enclosures with Participating Media. *Journal of Heat Transfer*, 112(2):415–423, 1990.

[41] K. Prasad, C. Li, K. Kailasanath, C. Ndubizu, R. Ananth, and P.A. Tatem. Numerical modelling of methanol liquid pool fires. *Combustion Theory and Modelling*, 3:743–768, 1999.

[42] A. Atreya. Pyrolysis, Ignition and Fire Spread on Horizontal Surfaces of Wood. NBS GCR 83-449, National Bureau of Standards (now NIST), Gaithersburg, Maryland, 1983.

[43] S.J. Ritchie, K.D. Steckler, A. Hamins, T.G. Cleary, J.C. Yang, and T. Kashiwagi. The Effect of Sample Size on the Heat Release Rate of Charring Materials. In *Proceedings of the 5th International Symposium on Fire Safety Science*, pages 177–188. International Association For Fire Safety Science, 1997.

[44] G. Heskestad and R.G. Bill. Quantification of Thermal Responsiveness of Automatic Sprinklers Including Conduction Effects. *Fire Safety Journal*, 14:113–125, 1988.

[45] P. Ruffino and M. di Marzo. Temperature and Volumetric Fraction Measurements in a Hot Gas Laden with Water Droplets. *Journal of Heat Transfer*, 125(2), April 2003.

[46] P. Ruffino and M. di Marzo. The Effect of Evaporative Cooling on the Activation Time of Fire Sprinklers. In *Fire Safety Science – Proceedings of the Seventh International Symposium*. International Association for Fire Safety Science, 2002.

[47] F. Gavelli, P. Ruffino, G. Anderson, and M. di Marzo. Effect of Minute Water Droplets on a Simulated Sprinkler Link Thermal Response. NIST GCR 99-776, National Institute of Standards and Technology, Gaithersburg, Maryland, July 1999.

[48] T.S. Chan. Measurements of Water Density and Droplet Size Distributions of Selected ESFR Sprinklers. *Journal of Fire Protection Engineering*, 6(2):79–97, 1994.

[49] H.Z. Yu. Investigation of Spray Patterns of Selected Sprinklers with the FMRC Drop Size Measuring System. In *Fire Safety Science – Proceedings of the First International Symposium*, pages 1165–1176. International Association For Fire Safety Science, 1986.

[50] A. Hamins and K.B. McGrattan. Reduced-Scale Experiments to Characterize the Suppression of Rack Storage Commodity Fires. NISTIR 6439, National Institute of Standards and Technology, Gaithersburg, Maryland, 1999.

[51] A. Hamins and K.B. McGrattan. Reduced-Scale Experiments on the Water Suppression of a Rack-Storage Commodity Fire for Calibration of a CFD Fire Model. In *Fire Safety Science – Proceedings of the Seventh International Symposium*, pages 457–468. International Association for Fire Safety Science, 2002.

[52] N. Cheremisinoff. *Encyclopedia of Fluid Mechanics, Volume 3: Gas-Liquid Flows*. Gulf Publishing Co., Houston, Texas, 1986.

[53] T. Ravigururajan and M. Beltran. A Model for Attenuation of Fire Radiation Through Water Droplets. *Fire Safety Journal*, 15:171–181, 1989.

[54] A. Tuntomo, C. Tien, and S. Park. Optical Constants of Liquid Hydrocarbon Fuels. *Combustion Science and Technology*, 84:133–140, 1992.

[55] W.J. Wiscombe. Improved Mie Scattering Algorithms. *Applied Optics*, 19(9):1505–1509, 1980.

[56] G.M. Hale and M.R. Quarry. Optical constants of water in the 200 nm to 200 mm wavelength region. *Applied Optics*, 12(3):555–563, 1973.

[57] H.Z. Yu, J.L. Lee, and H.C. Kung. Suppression of Rack-Storage Fires by Water. In *Fire Safety Science – Proceedings of the Fourth International Symposium*, pages 901–912. International Association For Fire Safety Science, 1994.

[58] K.B. McGrattan, R.G. Rehm, and H.R. Baum. Fire-Driven Flows in Enclosures. *Journal of Computational Physics*, 110(2):285–292, 1994.

[59] H.R. Baum, O.A. Ezekoye, K.B. McGrattan, and R.G. Rehm. Mathematical Modeling and Computer Simulation of Fire Phenomenon. *Theoretical and Computational Fluid Dynamics*, 6:125–139, 1994.

[60] W. Zhang, N. Ryder, R.J. Roby, and D. Carpenter. Modeling of the Combustion in Compartment Fires Using Large Eddy Simulation Approach. In *Proceedings of the 2001 Fall Technical Meeting, Eastern States Section*. Combustion Institute, Pittsburgh, Pennsylvania, December 2001.

[61] G. Continillo, F.M Denaro, and F.S. Marra. Accuracy and Stability Analysis of Time-Integrated Schemes for Advection-Diffusion-Reaction Equations. In *Seventh International Conference on Numerical Combustion*, page 99, 1998.

[62] J.Y. Murthy and S.R. Mathur. Radiative Heat Transfer in Axisymmetric Geometries Using an Unstructured Finite-Volume Method. *Numerical Heat Transfer, Part B*, 33:397–416, 1998.

[63] S.H. Kim and K.Y. Huh. Assessment of The Finite-Volume Method and The Discrete Ordinate Method for Radiative Heat Transfer In a Three-Dimensional Rectangular Enclosure. *Numerical Heat Transfer, Part B*, 35:85–112, 1999.

[64] W. Yang, T. Parker, H.D. Ladouceur, and R.J. Kee. The Interaction of Thermal Radiation and Water Mists in Fire Suppression. In *Proceedings of the Second NRIFD Symposium*. National Research Institute of Fire and Disaster (Japan), 2002.

[65] Green Mountain Software, Boulder, Colorado. *CRAYFISHPAK User's Guide, Cray Version 1.1*, 1990.

[66] W. Mell, K.B. McGrattan, and H. Baum. Numerical Simulation of Combustion in Fire Plumes. In *Twenty-Sixth Symposium (International) on Combustion*. Combustion Institute, Pittsburgh, Pennsylvania, 1996.

[67] K.B. McGrattan, H.R. Baum, and R.G. Rehm. Large Eddy Simulations of Smoke Movement. *Fire Safety Journal*, 30:161–178, 1998.

[68] Y. Xin, J.P. Gore, K.B. McGrattan, R.G. Rehm, and H.R. Baum. Large Eddy Simulation of Buoyant Turbulent Pool Fires. In *Proceedings of the 2002 Spring Technical Meeting, Central States Section*. Combustion Institute, Pittsburgh, Pennsylvania, April 2002.

[69] H.R. Baum, R.G. Rehm, P.D. Barnett, and D.M. Corley. Finite Difference Calculations of Buoyant Convection in an Enclosure, Part I: The Basic Algorithm. *SIAM Journal of Scientific and Statistical Computing*, 4(1):117–135, 1983.

[70] H.R. Baum and R.G. Rehm. Finite Difference Solutions for Internal Waves in Enclosures. *SIAM Journal of Scientific and Statistical Computing*, 5(4):958–977, 1984.

[71] R.G. Rehm, H.R. Baum, P.D. Barnett, and D.M. Corley. Finite Difference Calculations of Buoyant Convection in an Enclosure, Part II: Verification of the Nonlinear Algorithm. *Applied Numerical Mathematics*, 1:515–529, 1985.

[72] J.C. Adams, W.S. Brainerd, J.T. Martin, B.T. Smith, and J.L. Wagener. *Fortran 95 Handbook: Complete ISO/ANSI Reference*. MIT Press, Cambridge, Massachusetts, 1997.

[73] W. Mell and T. Kashiwagi. Dimensional Effects on Microgravity Flame Transition. In *Twenty-Seventh Symposium (International) on Combustion*. Combustion Institute, Pittsburgh, Pennsylvania, 1998.

[74] W. Mell, S.L. Olson, and T. Kashiwagi. Flame Spread Along Free Edges of Thermally-Thin Samples in Microgravity. In *Twenty-Eighth Symposium (International) on Combustion*. Combustion Institute, Pittsburgh, Pennsylvania, 2000.

[75] T. Kashiwagi, W. Mell, K. McGrattan, H. Baum, S. Olson, O. Fujita, M. Kikuchi, and K. Ito. Ignition, Transition, Flame Spread in Multidimensional Configurations in Microgravity. In *Proceedings of the 4th International Microgravity Combustion Workshop*. National Aeronautics and Space Administration, Lewis Research Center, Cleveland, Ohio, May 1997.

[76] A. Jhalani. A Numerical Study of Stretch in Partially Premixed Flames. Master's thesis, University of Illinois at Chicago, 2001.

[77] A. Mukhopadhyay and I. Puri. An Assessment of Stretch Effects on Flame Tip Using the Thin Flame and Thick Formulations. *Combustion and Flame*, 133:499–502, 2003.

[78] A. Hamins, M. Bundy, I. Puri, K.B. McGrattan, and W.C. Park. Suppression of Low Strain Rate Non-Premixed Flames by an Agent. In *Proceedings of the 6th International Microgravity Combustion Workshop, NASA/CP-2001-210826*, pages 101–104. National Aeronautics and Space Administration, Lewis Research Center, Cleveland, Ohio, May 2001.

[79] P. Friday and F. W. Mowrer. Comparison of FDS Model Predictions with FM/SNL Fire Test Data. NIST GCR 01-810, National Institute of Standards and Technology, Gaithersburg, Maryland, April 2001.

[80] A. Bounagui, N. Benichou, C. McCartney, and A. Kashef. Optimizing the Grid Size Used in CFD Simulations to Evaluate Fire Safety in Houses. In *3rd NRC Symposium on Computational Fluid Dynamics, High Performance Computing and Virtual Reality*, Ottawa, Ontario, Canada, December 2003. National Research Council, Canada.

[81] R.L. Alpert. *SFPE Handbook of Fire Protection Engineering*, chapter Ceiling Jet Flows. National Fire Protection Association, Quincy, Massachusetts, 3rd edition, 2003.

[82] Y. Xin, J.P. Gore, K.B. McGrattan, R.G. Rehm, and H.R. Baum. Large Eddy Simulation of Buoyant Turbulent Pool Fires. In *Twenty-Ninth Symposium (International) on Combustion*. Combustion Institute, Pittsburgh, Pennsylvania, 2002.

[83] J.A. Ierardi and J.R. Barnett. A Quantititive Method for Calibrating CFD Model Calculations. In *Proceedings of the CIB-CTBUH International Conference on Tall Buildings*. International Council for Research and Innovation in Building and Construction (CIB), 2003.

[84] N. Petterson. Assessing the feasibility of reducing the grid resolution in fds field modeling. Technical report, University of Canterbury, Christchurch, New Zealand, February 2002.

[85] A. Musser, K. B. McGrattan, and J. Palmer. Evaluation of a Fast, Simplified Computational Fluid Dynamics Model for Solving Room Airflow Problems. NISTIR 6760, National Institute of Standards and Technology, Gaithersburg, Maryland, June 2001.

[86] K.B. McGrattan, J.E. Floyd, G.P. Forney, H.R. Baum, and S. Hostikka. Improved Radiation and Combustion Routines for a Large Eddy Simulation Fire Model. In *Fire Safety Science – Proceedings of the Seventh International Symposium*. International Association for Fire Safety Science, 2002.

[87] W. Zhang, A. Hamer, M. Klassen, D. Carpenter, and R. Roby. Turbulence Statistics in a Fire Room Model by Large Eddy Simulation. *Fire Safety Journal*, 2002.

[88] H. Baum, K. McGrattan, and R. Rehm. Large Eddy Simulation of Smoke Movement in Three Dimensions. In *Proceedings of the Ninth International Interflam Conference*. Interscience Communications, London, March 1996.

[89] H.R. Baum, K.B. McGrattan, and R.G. Rehm. Large Eddy Simulations of Smoke Movement in Three Dimensions. In *Proceedings of the Seventh International Interflam Conference*, pages 189–198. Interscience Communications, London, 1996.

[90] H.R. Baum and B.J. McCaffrey. Fire Induced Flow Field – Theory and Experiment. In *Fire Safety Science – Proceedings of the Second International Symposium*, pages 129–148. International Association for Fire Safety Science, 1989.

[91] J.M. Clement and C.M. Fleischmann. Experimental Verification of the Fire Dynamics Simulator Hydrodynamic Model. In *Fire Safety Science – Proceedings of the Seventh International Symposium*, pages 839–862. International Association for Fire Safety Science, 2002.

[92] T. Cleary, M. Anderson, J. Averill, and W. Grosshandler. Evaluating Multi-Sensor Fire Detectors in the Fire Emulator/Detector Evaluator. In *Proceedings of the Eighth International Interflam Conference*, pages 453–464. Interscience Communications Ltd., June 1999.

[93] W. Davis, K Notarianni, and K. McGrattan. Comparison of Fire Model Predictions with Experiments Conducted in a Hangar with a 15 Meter Ceiling. NISTIR 5927, National Institute of Standards and Technology, Gaithersburg, Maryland, December 1996.

[94] S.J. Emmerich and K.B. McGrattan. Application of a Large Eddy Simulation Model to Study Room Airflow. *ASHRAE Transactions*, 104(1):1–9, 1998.

[95] K.B. McGrattan, H.R. Baum, and R.G. Rehm. Numerical Simulation of Smoke Plumes from Large Oil Fires. *Atmospheric Environment*, 30(24):4125–4136, 1996.

[96] T. Yamada. Smoke Plume Trajectory from In-Situ Burning of Crude Oil in Tomakomai. Technical report, National Research Institute of Fire and Disaster, Japan, November 1998.

[97] A. Hamins, A. Maranghides, K.B. McGrattan, E. Johnsson, T.J. Ohlemiller, M. Donnelly, J. Yang, G. Mulholland, K. Prasad, S. Kukuck, R. Anleitner, and T. McAllister. Report on Experiments to Validate Fire Dynamic and Thermal-Structural Models for Use in the World Trade Center Investigation. NIST Special Publication in preparation, National Institute of Standards and Technology, Gaithersburg, Maryland, 2004.

[98] W.D. Walton and P.H. Thomas. *SFPE Handbook of Fire Protection Engineering*, chapter Estimating Temperatures in Compartment Fires. National Fire Protection Association, Quincy, Massachusetts, 3rd edition, 2002.

[99] A. Hamins, A. Maranghides, K.B. McGrattan, Ohlemiller, and R. Anletiner. Experiments to Validate Models of Fire Growth and Spread for use in the World Trade Center Investigation. NIST Special Publication in preparation, National Institute of Standards and Technology, Gaithersburg, Maryland, 2004.

[100] W.K. Chow and R. Yin. Discussion on Two Plume Formulae with Computational Fluid Dynamics. *Journal of Fire Sciences*, 20(3), May 2002.

[101] F. Battaglia, K. McGrattan, R. Rehm, and H. Baum. Simulating Fire Whirls. *Combustion Theory and Modeling*, 4, 2000.

[102] S. Hostikka, K.B. McGrattan, and A. Hamins. Numerical Modeling of Pool Fires using Large Eddy Simulation and Finite Volume Method for Radiation. In *Fire Safety Science – Proceedings of the Seventh International Symposium*. International Association for Fire Safety Science, 2002.

[103] J. Hietaniemi, S. Hostikka, and J. Vaari. FDS Simulation of Fire Spread – Comparison of Model Results with Experimental Data. Technical Report VTT Working Paper 4, VTT Building and Transport, Espoo, Finland, 2004.

[104] X. Yuan. Measurement and Computation of Room Airflow with Ventilation. Technical Report RP949, American Society of Heating, Refrigerating, Air-Conditioning Engineers, 1999.

[105] K. Mniszewski. The Use of FDS for Estimation of Flammable Gas/Vapor Concentrations. In *Proceedings of the 3rd Technical Symposium on Computer Applications in Fire Protection Engineering*. Society for Fire Protection Engineers, Bethesda, Maryland, November 2001.

[106] S. Kerber and W. Walton. Characterizing Positive Pressure Ventilation using Computational Fluid Dynamics. NISTIR 7065, National Institute of Standards and Technology, Gaithersburg, Maryland, February 2003.

[107] R. Rehm, K. McGrattan, H. Baum, and E. Simiu. An Efficient Large Eddy Simulation Algorithm for Computational Wind Engineering: Application to Surface Pressure Computations on a Single Building. NISTIR 6371, National Institute of Standards and Technology, August 1999.

[108] R.G. Rehm, K.B. McGrattan, and H.R. Baum. Large Eddy Simulation of Flow over a Wooded Building Complex. *Wind & Structures*, 5(2), 2002.

[109] H.Y. Wang and P. Joulain. Numerical Simulation of Wind-Aided Turbulent Fires in a Ventilated Model Tunnel. In *Fire Safety Science – Proceedings of the Seventh International Symposium*. International Association for Fire Safety Science, 2002.

[110] F. Magnussen and B.H. Hjertager. On Mathematical Modeling of Turbulent Combustion with Special Emphasis on Soot Formation and Combustion. In *Proceedings of the Sixteenth Symposium (International) on Combustion*, pages 719–731. Combustion Institute, Pittsburgh, Pennsylvania, 1977.

[111] R. Vettori. Effect of an Obstructed Ceiling on the Activation Time of a Residential Sprinkler. NISTIR 6253, National Institute of Standards and Technology, Gaithersburg, Maryland, November 1998.

[112] J. Floyd. Comparison of CFAST and FDS for Fire Simulation with the HDR T51 and T52 Tests. NIST GCR 01-810, National Institute of Standards and Technology, Gaithersburg, Maryland, March 2002.

[113] A. Kashef, N. Benichou, G.D. Lougheed, and C. McCartney. A Computational and Experimental Study of Fire Growth and Smoke Movement in Large Spaces. Technical Report NRCC-45201, National Research Council Canada, 2002.

[114] K.B. McGrattan, A. Hamins, and D. Stroup. Sprinkler, Smoke & Heat Vent, Draft Curtain Interaction — Large Scale Experiments and Model Development. NISTIR 6196-1, National Institute of Standards and Technology, Gaithersburg, Maryland, September 1998.

[115] S. Olenick, M. Klassen, and R.J. Roby. Validation Study for FDS for a High Rack Storage Fire Involving Pool Chemicals. In *Proceedings of the 3rd Technical Symposium on Computer Applications in Fire Protection Engineering*. Society of Fire Protection Engineers, Bethesda, Maryland, September 2001.

[116] S. Cochard. Validation of Fire Dynamics Simulator (Version 2.0) Freeware. *Tunnel Management International Journal*, 6(4), December 2003.

[117] Memorial Tunnel Fire Ventilation Test Program. Interactive CD-ROM and Comprehensive Test Report, Massachusetts Highway Department, 1996.

[118] K. B. McGrattan and A. Hamins. Numerical Simulation of the Howard Street Tunnel Fire, Baltimore, Maryland, July 2001. NISTIR 6902, National Institute of Standards and Technology, Gaithersburg, Maryland, January 2003. Joint Publication of NIST and the US Nuclear Regulatory Commission (NUREG/CR-6793).

[119] V. D'Souza, J.A. Sutula, S.M. Olenick, W. Zhang, and R.J. Roby. Use of Fire Dynamics Simulator to Predict Smoke Detector Activation. In *Proceedings of the 2001 Fall Technical Meeting, Eastern States Section*. Combustion Institute, Pittsburgh, Pennsylvania, December 2001.

[120] T. Cleary, M. Donnelly, G. Mulholland, and B. Farouk. Fire Detector Performance Predictions in a Simulated Multi-Room Configuration. In *Proceedings of the 12th International Conference on Automatic Fire Detection (AUBE '01)*. National Institute of Standards and Technology, Gaithersburg, Maryland, March 2001. NIST SP 965.

[121] A. Piergiorgio, D. Giuseppe, F. Dino, G. Zappellini, and A. Ferrari. CFD Simulations of a Truck Fire in the Underground Gran Sasso National Laboratory. In *Proceedings of the 5th Italian Conference on Chemical and Process Engineering*. Associazione Italiana Di Ingegneria Chimica (AIDIC), May 2001.

[122] J.E. Floyd, C. Wieczorek, and U. Vandsburger. Simulations of the Virginia Tech Fire Research Laboratory Using Large Eddy Simulation with Mixture Fraction Chemistry and Finite Volume Radiative Heat Transfer. In *Proceedings of the Ninth International Interflam Conference*. Interscience Communications, London, 2001.

[123] J.E. Floyd, C. Wieczorek, and U. Vandsburger. Post-Test Computations of the Virginia Tech Propane Fire Compartment Study Using FDS v2. In *Fire Safety Science – Proceedings of the Seventh International Symposium*. International Association for Fire Safety Science, 2002.

[124] S. Dillon and A. Hamins. Ignition Propensity and Heat Flux Profiles of Candle Flames for Fire Investigation. In Vytenis Babrauskas, editor, *Fire Science Applications to Fire Investigations*. Interscience Communications Ltd., London, 2003.

[125] D. Madrzykowski and R.L. Vettori. Simulation of the Dynamics of the Fire at 3146 Cherry Road NE Washington D.C., May 30, 1999. NISTIR 6510, National Institute of Standards and Technology, Gaithersburg, Maryland, April 2000.

[126] R.L. Vettori, D. Madrzykowski, and W.D. Walton. Simulation of the Dynamics of a Fire in a One-Story Restaurant – Texas, February 14, 2000. NISTIR 6923, National Institute of Standards and Technology, Gaithersburg, Maryland, October 2002.

[127] D. Madrzykowski, G.P. Forney, and W.D. Walton. Simulation of the Dynamics of a Fire in a Two-Story Duplex – Iowa, December 22, 1999. NISTIR 6854, National Institute of Standards and Technology, Gaithersburg, Maryland, January 2002.